

## Durham E-Theses

---

### *Simulating the 21-cm signal from the Epoch of Reionization*

Tam, Wong Kenneth

#### How to cite:

---

Tam, Wong Kenneth (2009) *Simulating the 21-cm signal from the Epoch of Reionization*, Durham theses, Durham University. Available at Durham E-Theses Online: <http://etheses.dur.ac.uk/2033/>

#### Use policy

---

The full-text may be used and/or reproduced, and given to third parties in any format or medium, without prior permission or charge, for personal research or study, educational, or not-for-profit purposes provided that:

- a full bibliographic reference is made to the original source
- a [link](#) is made to the metadata record in Durham E-Theses
- the full-text is not changed in any way

The full-text must not be sold in any format or medium without the formal permission of the copyright holders.

Please consult the [full Durham E-Theses policy](#) for further details.

# Simulating the 21-cm Signal from the Epoch of Reionization

by Wong Kenneth Tam

A thesis submitted to the University of Durham  
in accordance with the regulations for  
admittance to the Degree of Master of Science.

Department of Physics

University of Durham

March 2009

The copyright of this thesis rests with the author or the university to which it was submitted. No quotation from it, or information derived from it may be published without the prior written consent of the author or university, and any information derived from it should be acknowledged.



- 1 MAY 2009

# Simulating the 21-cm Signal from the Epoch of Reionization

by Wong Kenneth Tam

M.Sc. Thesis, March 2009

## Abstract

In this thesis, the 21-cm signal from the epoch of reionization is simulated using a combination of N-Body techniques and semi-analytical models. Images, line-of-sight spectra and power spectra of the simulated 21-cm signal are presented.

The N-Body code, GADGET-2, is used to obtain the distribution of dark matter and a friends-of-friends algorithm is used to identify dark matter halos to construct halo merger trees. We ran seven simulations with periodic boxes of volumes ranging from  $(10h^{-1}\text{Mpc})^3$  to  $(140h^{-1}\text{Mpc})^3$ , and particle masses ranging from  $6.46 \times 10^4 h^{-1}M_{\odot}$  to  $1.42 \times 10^9 h^{-1}M_{\odot}$ . These merger trees are used with the GALFORM semi-analytical model of galaxy formation to predict the locations of galaxies and their ionizing luminosities within the halos. We find that halos in a broad range of masses contribute significantly to the total ionizing emissivity of each simulation. The effect of suppressing gas cooling due to reionization in low mass halos in GALFORM was also investigated. For a redshift of reionization,  $z_{\text{reion}} = 15$ , this significantly reduces the number of ionizing photons produced at  $z < 15$ . This results in a prolonged period of reionization as the Universe makes the transition from neutral to fully ionized.

Next, the 21-cm signal and ionization state of the hydrogen is calculated for the simulation box with a volume of  $(20h^{-1}\text{Mpc})^3$  and a particle mass of  $5.17 \times 10^5 h^{-1}M_{\odot}$ . The hydrogen is assumed to follow the dark matter, and the 21-cm differential brightness temperature is calculated from the distribution of neutral hydrogen. High resolution images and spectra of the 21-cm signal are generated from these neutral hydrogen density fields. A toy model is first investigated, randomly distributed ionized spheres of constant radii are generated to investigate the effect ionized regions have on the 21-cm power spectra. We find that this increases power on the scales of the size of the ionized spheres, but decreases power on small scales. The amount of change in power is sensitive to the overall ionized fraction of the simulation box, increasing the ionized

---

fraction increases the power on the scales of the spheres while decreases the power on small scales. Next, the GALFORM model is investigated. The ionizing luminosities of GALFORM galaxies are used to calculate cosmological Strömgren spheres representing ionized regions. These spheres are “painted” around the location of the galaxies on the density field. We find that the power spectra lack any obvious features due to the range of sizes of the GALFORM ionized regions. However, the power spectra is sensitive to the ionized fraction of the simulation box. The slope of the power spectra decreases as ionized fraction increases.

Finally, the temperature field is smoothed over a bandwidth of 200kHz and a 2-D Gaussian beam with a FWHM of 3 arcmin to emulate the LOFAR telescope beam response. We find that only the largest features, such as large ionized regions, are still identifiable after smoothing. LOFAR should be able to detect the early stages of reionization, but may have difficulties during later stages when much of the brightest 21-cm signal is removed by reionization.

# Contents

<b>1</b>	<b>Introduction</b>	<b>1</b>
1.1	Background . . . . .	1
1.1.1	The Big Bang and the Expanding Universe . . . . .	2
1.1.2	The Cosmic Microwave Background . . . . .	2
1.1.3	Big Bang Nucleosynthesis . . . . .	4
1.1.4	Cosmic Inflation . . . . .	5
1.1.5	The Dark Ages . . . . .	6
1.1.6	Dark Matter . . . . .	7
1.1.7	Galaxy Formation . . . . .	11
1.2	Reionization . . . . .	15
1.2.1	Observational Constraints . . . . .	16
1.2.2	Theoretical Models of Reionization . . . . .	18
1.3	21-cm Signal . . . . .	20
1.3.1	Fundamental Physics of the 21-cm Line . . . . .	20
1.3.2	Spin Temperature . . . . .	21
1.3.3	The Wouthuysen-Field Effect . . . . .	23
1.4	Motivation for this work . . . . .	25
<b>2</b>	<b>Tools for simulating the Evolution of the Universe</b>	<b>29</b>
2.1	Introduction . . . . .	29
2.2	N-Body Simulations . . . . .	30
2.2.1	GADGET-2 . . . . .	30
2.3	GALFORM: A semi-analytical model . . . . .	35
2.3.1	Dark Matter Halo Merger Trees . . . . .	40

2.4	Running the simulations . . . . .	43
<b>3</b>	<b>Simulating the Epoch of Reionization</b>	<b>47</b>
3.1	Introduction . . . . .	47
3.2	Ionizing Emissivities as a Function of Halo Mass . . . . .	47
<b>4</b>	<b>Simulating the 21-cm Signal</b>	<b>59</b>
4.1	Introduction . . . . .	59
4.2	Current status of 21-cm Signal simulations . . . . .	59
4.3	Generating 21-cm Maps and Power Spectra . . . . .	61
4.3.1	Calculating the 21-cm Brightness Temperature . . . . .	61
4.3.2	Cosmological HII Regions . . . . .	64
4.4	21-cm Line of Sight Spectra . . . . .	71
4.5	21-cm Power Spectra . . . . .	74
4.6	Smoothing the Signal . . . . .	80
<b>5</b>	<b>Summary and Conclusions</b>	<b>87</b>
5.1	Ionizing luminosities from the GALFORM model . . . . .	87
5.2	The 21-cm Signal . . . . .	88
5.3	Directions for Future Work . . . . .	90

# List of Figures

1.1	WMAP 5-year temperature power spectrum . . . . .	3
1.2	Rotation Curve of galaxy NGC 2198 . . . . .	8
1.3	Comparison of different analytical halo mass functions . . . . .	10
1.4	Luminosity function of galaxies . . . . .	14
1.5	Quasar spectra with Gunn-Peterson Trough . . . . .	17
1.6	De-excitation rate coefficients for H-H and e-H collisions . . . . .	23
1.7	Level diagram illustrating the Wouthuysen-Field effect . . . . .	24
2.1	2D slice of density field from a L-GADGET2 simulation . . . . .	34
2.2	GALFORM Schematic Diagram . . . . .	36
2.3	Halo mass function of FOF halos from L-GADGET-2 simulation . . . . .	42
3.1	Total ionizing emissivity in logarithmic mass bins demonstrating effect of mass resolution . . . . .	48
3.2	Total ionizing emissivity in logarithmic mass bins demonstrating effect of simulation box size . . . . .	49
3.3	Evolution of the total ionizing emissivity in logarithmic mass bins in redshift	50
3.4	Fraction of ionizing emissivity produced in halos below a given mass . . .	51
3.5	Effect of Adjusting zcut parameter in GALFORM at z=14.64 . . . . .	53
3.6	Effect of adjusting zcut parameter in GALFORM at z=9.80 on the ionizing emissivity . . . . .	54
3.7	Effect of adjusting zcut parameter in GALFORM at z=7.97 on the ionizing emissivity . . . . .	55
3.8	Number of ionizing photons per neutral hydrogen atom as a function of redshift . . . . .	56

3.9	Number of ionizing photons per hydrogen atom as a function of redshift with modified $z_{\text{cut}}$ . . . . .	57
4.1	Over-density of a 2D slice at redshift of 14.64 . . . . .	67
4.2	Differential brightness temperature of a 2D slice at redshift of 14.64 . . . . .	68
4.3	Differential brightness temperature of a 2D slice at redshift of 14.64 with ionized regions . . . . .	69
4.4	Differential brightness temperature of 2D slices at various redshifts, overlaid with ionized regions . . . . .	70
4.5	Example LOS spectra . . . . .	73
4.6	Power spectra of the hydrogen over-density and differential brightness temperature fields of the L20_N1024 simulation at redshift of 14.64 . . . . .	75
4.7	2D slices and 3D Power spectra of the 21-cm brightness temperature field with randomly distributed ionized regions, varying the number of bubbles. . . . .	76
4.8	2D slices and 3D Power spectra of the 21-cm brightness temperature field with randomly distributed ionized regions, varying the size of the bubbles while keeping the ionized fraction approximately constant. . . . .	78
4.9	3D power spectra of the 21-cm brightness temperature field with ionized regions generated from GALFORM sources at various redshifts . . . . .	79
4.10	Differential brightness temperature of a bandwidth-smoothed 2D slice at redshift of 14.64 . . . . .	81
4.11	Differential brightness temperature of a bandwidth and beam-smoothed 2D slice at redshift of 14.64 . . . . .	82
4.12	Example of smoothed LOS spectrum overplotted on the original spectrum . . . . .	83
4.13	Example of smoothed LOS spectrum . . . . .	84
4.14	Power spectra of the bandwidth and beam smoothed differential brightness temperature field . . . . .	85

# List of Tables

2.1	List of simulations . . . . .	43
2.2	Cosmological parameters . . . . .	44
2.3	GALFORM parameters used . . . . .	45
2.4	GALFORM parameters used for Monte-Carlo merger trees . . . . .	45
3.1	Redshifts at which one ionizing photon is produced for every neutral hydrogen atom in simulations . . . . .	58
4.1	The ionized fraction of the L20_N1024 box at various redshift and the fraction of ionized volume that is overlapping . . . . .	71

## Declaration

The work described in this thesis was undertaken between 2007 and 2009 while the author was a research student under the supervision of Dr. Tom Theuns and Dr. Cedric Lacey in the Department of Physics at the University of Durham. This work has not been submitted for any other degree at the University of Durham or any other University.

The description of the GADGET-2 code found in section 2.2.1 is based on the description which appears in the following paper:

- Springel, V., 2005, MNRAS, 364, 1105

The description of the GALFORM semi-analytical model found in section 2.3 is based on the description which appears in the following papers:

- Cole, S.; Lacey, C.G.; Baugh, C.M.; Frenk, C.S., 2000, MNRAS, 319, 168
- Baugh, C.M.; Lacey, C.G.; Frenk, C.S.; Granato, G.L.; Silva, L.; Bressan, A.; Benson, A.J.; Cole, S., 2005, MNRAS, 356, 1191

The copyright of this thesis rests with the author. This copy has been supplied for the purpose of research or private study on the understanding that it is copyright material and that no quotation from the thesis may be published without proper acknowledgement.

## Acknowledgements

The work carried out in this thesis would not have been possible without the guidance and support of my supervisors, Dr. Tom Theuns and Dr. Cedric Lacey.

I would like to thank John Helly for his help with running the N-Body simulations used in this thesis, and Milan Raicevic for his input during the numerous discussions we had between Dr. Theuns, Dr. Lacey, Mr. Raicevic and myself.

I also thank Volker Springel for providing a copy of the N-GENiC code, used to generate the initial conditions for the N-Body simulation code, GADGET-2, as well as providing the friends-of-friends algorithms used to locate dark matter halos within the N-Body simulations.



# Chapter 1

## *Introduction*

### 1.1 Background

The Universe as we observe it today is filled with complex objects, these objects have fascinated humans for thousands of years, provoking the questions of where and how these objects came into existence. Based on current theories of cosmology, the very early Universe emerging out of the Big Bang was extremely hot and dense, and almost entirely homogeneous. Small density fluctuations in this initial state grew through gravitational instabilities as the Universe expanded, eventually cooling to form the stars and galaxies we observe today. This is known as the Hot Big Bang model.

Our understanding in Cosmology lies mainly in two periods, the very early Universe right after the Big Bang, and also the local Universe as we observe it. Study in elementary particle physics has helped us understand the very early Universe, while observations have given us a wealth of information on the current state of the Universe. However, little is known about the gap of time in between, as luminous objects had yet to form, the Universe was composed of mainly neutral hydrogen and little could be observed.

The transition from a mostly neutral Universe to the highly ionized Universe we observe now is known as the Epoch of Reionization. To observe this Epoch, large arrays of radio telescopes are being built to attempt to observe the 21-cm signal, caused by emission due to a highly forbidden electron spin state transition in neutral hydrogen atoms.

In this introductory chapter, I present an overview of the Hot Big Bang model in modern cosmology and the observational evidence supporting it. I also present the evidence for reionization and the theory for 21-cm emission.



### 1.1.1 The Big Bang and the Expanding Universe

In the standard model of modern cosmology, the Universe expanded from an extremely hot and dense initial state, shortly after the Big Bang, the Universe went through a stage of rapid, exponential expansion known as inflation (see section 1.1.4). The Universe continued to expand and cool after inflation, forming the matter and structure we see today.

The first evidence for an expanding Universe came when Edwin Hubble announced his discovery of a linear relationship between the distances to galaxies and their recessional velocities, measured from their redshifts, in 1929. This relationship was exactly what one would expect to observe in a Universe that was expanding uniformly. Together with Milton Humason, Hubble formulated what is now known as Hubble's Law:

$$v = H_0 d, \quad (1.1)$$

where  $d$  is the distance to the observed galaxy and the constant of proportionality,  $H_0$ , is known as Hubble's constant. Hubble's constant indicates the rate at which the Universe is expanding, and at that time, Hubble estimated this constant to be around  $500 \text{kms}^{-1} \text{Mpc}^{-1}$  (Hubble, 1929). It was later realised that the expansion rate of the Universe varied with cosmic time and  $H_0$  in eq. (1.1) is in fact a parameter dependent on time.  $H_0$  now refers to Hubble's parameter at present time. More recent measurements, for example, from the HST key project (Freedman et al., 2001), gives  $H_0 = 72 \pm 0.08 \text{kms}^{-1} \text{Mpc}^{-1}$ . The expansion of the Universe suggests that at one point in the past, the Universe was infinitesimally small in volume. This is strong evidence for the Big Bang Theory.

### 1.1.2 The Cosmic Microwave Background

The Cosmic Microwave Background Radiation (CMB) was discovered in 1965 by Penzias and Wilson, for which they won the Nobel Prize in 1978. The CMB has a thermal blackbody spectrum that peaks in the microwave range frequency of 160.2GHz and is almost entirely isotropic.

The CMB is believed to be a relic of the Big Bang. During the first few days of the Universe, the Universe was extremely hot, and the photons and baryons formed a plasma. This plasma was kept in thermal equilibrium since the ionized matter was coupled to the radiation through the constant scattering of photons off ions and electrons. As the

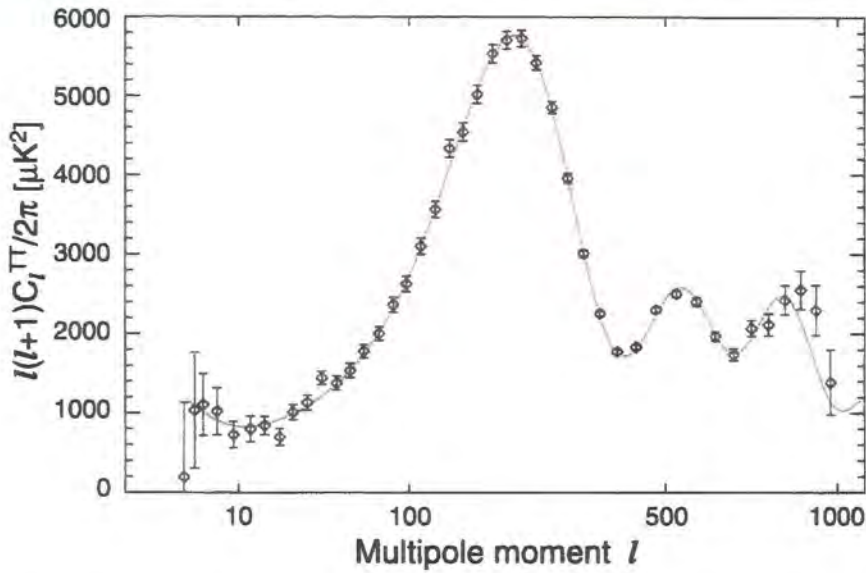


Figure 1.1: The WMAP 5-year temperature power spectrum. The red curve is the best fit Lambda-CDM Model to the WMAP data (Nolta et al., 2008).

Universe expanded and the temperature dropped, protons and electrons combined to form hydrogen in a process known as recombination. The removal of free electrons in the Universe meant photons were no longer scattered via Thomson scattering, and were able to propagate freely through space. Since the photons were in thermal equilibrium prior to recombination, the spectrum of this radiation carries the shape of a blackbody spectrum. As the Universe continued to expand, these photons were redshifted and the temperature fell, however, the shape of the blackbody spectrum was preserved. Observations made by the Cosmic Microwave Background Explorer (COBE) have determined the temperature of the CMB spectrum to be 2.73 K (Mather et al., 1994). The Wilkinson Microwave Anisotropy Probe (WMAP) succeeded the COBE mission to measure the small temperature differences in the CMB in different directions on the sky. WMAP measured the power spectrum of the CMB and this is shown in Fig. 1.1. The various peaks and troughs of the power spectrum contain a wealth of information about the origin of the Universe. Varying different cosmological parameters changes the spectrum in different ways and cosmologists have been able to constrain key parameters using the observed spectrum. The observation of the CMB is regarded as strong evidence that the Universe was at one time much hotter and denser than the present, thus supporting the

Big Bang Theory.

### 1.1.3 Big Bang Nucleosynthesis

Big bang nucleosynthesis describes the production of elements heavier than hydrogen, explaining the abundance of “light elements” (deuterium, helium and lithium and beryllium) that is observed today. Big bang nucleosynthesis begins shortly after the big bang, when the Universe has cooled sufficiently for stable protons and neutrons to form. The ratio of neutrons to protons is kept in thermal equilibrium via weak interactions:



where  $e^-$  and  $e^+$  are the electron and positron,  $\nu$  and  $\bar{\nu}$  are the electron neutrino and anti-neutrino. Initially, the thermal energy is sufficient to support the reactions in both directions. However, the mass difference between a proton and neutron means that as the Universe expands and the temperature falls further, the reaction converting neutrons to protons becomes more energetically favourable. There are now more protons than neutrons as weak reactions maintain the ratio at the equilibrium point, this continues until the temperature falls further and neutrinos decouple. The neutron abundance falls as neutrons decay. However, most of the neutrons bind with protons to form deuterium before decaying. The high photon density and low binding energy of deuterium means heavier nuclei form only when the temperature falls further, at which heavier elements, mostly helium, are created. Eventually the temperature falls to a point where the coulomb repulsion prevents further nuclear reactions. The limited time between which deuterium begins to form and the coulomb force becomes significant means that only lighter elements are created. The absence of stable nuclei with atomic masses of five and eight also means nucleosynthesis via  $\text{He} + p$  and  $\text{He} + \text{He}$  is not possible, causing nearly all of the neutrons to form into stable helium nuclei. Trace amounts of lithium and beryllium are also created via rare reactions. Heavier elements are produced later, within stars and supernovae explosions. The theory of big bang nucleosynthesis predicts the abundances given the baryonic density of the Universe. Observational constraints on abundances of light elements can therefore be used to constrain the baryon density parameter within a narrow range. CMB observations with the WMAP have provided an

independent value for this parameter and have found the predictions of big bang nucleosynthesis to be in agreement with observations.

### 1.1.4 Cosmic Inflation

Inflation is considered a key component of standard hot big bang cosmology, it describes a period of rapid, exponential expansion during the very early Universe, the Universe expanded by a factor of  $10^{40}$  to  $10^{100}$ . During inflation, primordial perturbations that were initially quantum fluctuations, were inflated to macroscopic scales. Gravity then acted on these small perturbations to create the structures we see today by making the denser regions more dense, and under-dense regions less dense. Although the detailed particle physics mechanism that drove inflation is not known, it is considered in the standard cosmological model as it is able to resolve several problems that, without inflation, would be inferred from the observed Universe today.

#### Key problems of the Big Bang Model

1. **The horizon problem:** Why is it that the Universe we observe appears to be homogeneous and isotropic? The observed CMB temperature is nearly isotropic, it has nearly the same temperatures in all directions we look. This would not be a problem if the different regions of the sky were able to interact and achieve thermal equilibrium. However, the expansion of the Universe is faster than the speed of light, the radiation that we observe from one side of the Universe has only just reached us so it is impossible that it has also reached the opposite side of the sky.
2. **The flatness problem:** Current observations set the current density of the Universe very close to the critical density (A flat Universe, hence the name of the problem). However, this arrangement is unstable, the density diverges from the critical value rapidly over cosmic time. The Universe must have had a density value even closer to the critical value in the early Universe, and cosmologists question how the initial density could be set to such a specific value.
3. **Magnetic monopole problem:** Magnetic monopoles and other exotic particles such as gravitinos, are predicted by Grand Unified Theories to have been produced with a high abundance in the hot, dense environment of the very early Universe. These

particles are predicted to be very massive, and therefore non-relativistic for most of the history of the Universe. This means these particles are diluted more slowly than radiation as the Universe expands (since mass density goes as  $a^{-3}$  while radiation density goes as  $a^{-4}$ ), and become dominant particles in the present Universe. However, the contrary is true, none of these exotic particles are observed today.

### Cosmic Inflation as the Solution

1. **The horizon problem:** Inflation solves this problem by increasing the size of a region of the Universe greatly. A small enough patch of the Universe can achieve thermal equilibrium before inflation, after which the patch expands to a much larger region. The opposite sides of the sky that are observed today to have the same temperature, were in fact in causal contact prior to inflation.
2. **The flatness problem:** Inflation's rapid expansion would expand away any large scale curvature of the Universe we can detect. This is analogous to blowing up a balloon. Before the balloon is blown up, a small patch would appear curved, but once the balloon blows up rapidly, the same patch will appear flat.
3. **Magnet monopole problem:** The rapid expansion of the Universe during inflation dilutes the density of these exotic particles. However, the temperature of the Universe at the end of the inflationary period must not be too high that these particles are regenerated.

Inflation provides a very convenient solution to some glaring problems of the Big Bang model and explains how structure formation was able to begin from initial quantum fluctuations. However, the origins of inflation are unknown and a lot of research is done in this area at the moment.

#### 1.1.5 The Dark Ages

The period directly following the recombination and the decoupling of CMB photons is known as the dark ages. This lasts until the formation of the first luminous objects, triggering reionization of the Universe (more of which in section 1.2). No direct observations have been made of this era because of the lack of luminous objects. The physics

content of the dark ages should be relatively simple compared to all the complex objects observed today, only a few basic processes would contribute to the evolution of the Universe. For this reason, observation of the dark ages could be very insightful in directly constraining various key parameters of a cosmological model, such as the baryon and matter density.

### 1.1.6 Dark Matter

Dark matter is an important ingredient of the Big Bang Model. It is called dark matter because it has never been observed directly. It is thought to be primarily non-baryonic and does not interact with light. The existence of dark matter was first inferred by Fritz Zwicky in 1933 when he applied the virial theorem to the Coma Cluster. He estimated the total mass of the cluster based on the motions of galaxies near the edge of the cluster. He then also estimated the mass using the cluster's brightness and the number of galaxies. When he compared the two, he discovered that the first estimation was approximately 400 times larger than the second. This implied that the visible mass would not be sufficient to maintain the high speed orbits of the galaxies near the edge of the cluster, inferring the existence of some non-visible form of matter we now know as dark matter. Further evidence comes from measuring rotation curves of galaxies, a plot of the orbital velocities of gas versus its radial distance from the centre of the host galaxy. Rotation curves of edge on spiral galaxies can be measured using spectroscopy. The 21-cm line is used to measure the velocities of the rotating gas. An example of a rotation curve from van Albada et al. (1985) is shown in Fig. 1.2. As can be seen in Fig. 1.2, the rotation curve is flat, this means most gas in spiral galaxies orbits roughly at the same speed regardless of the distance from the centre. This is surprising because most of the stars and observable mass reside in the galactic bulge and disk. Equating the centripetal force of a star to the gravitational force it feels yields

$$\frac{mv^2}{r} = \frac{GMm}{r^2}, \quad (1.4)$$

where  $m$  is the mass of the star,  $M$  is the mass of the host galaxy,  $v$  is the orbital velocity,  $r$  is radial distance from the galactic centre and  $G$  is the universal gravitational constant. If we assume most of the mass is at the centre (for the milky way, the galactic centre has

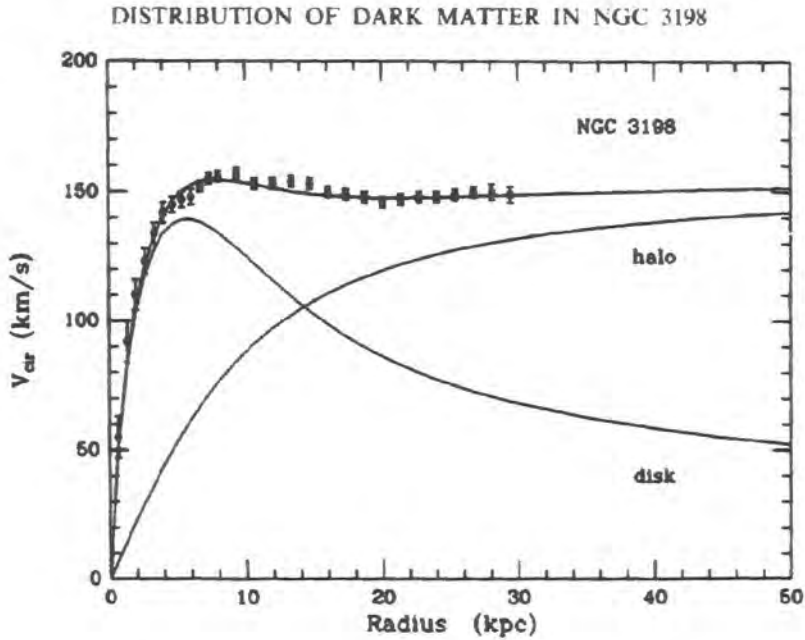


Figure 1.2: The points with error bars show the observed rotation curve of spiral galaxy NGC 3198. The solid lines show the fit to the data by van Albada et al. (1985), also shown are the separate contributions from the galactic disc and galactic halo according to parameters in their fit.

a diameter of  $\sim 20 - 30$  kpc) and does not depend on radius, this simplifies to:

$$v = \sqrt{\frac{GM}{r}}. \quad (1.5)$$

From eq. (1.5) we can see that as we move away from the galactic centre and  $r$  increases, the orbital velocity,  $v$  should decrease, resulting in the curve showing only the disc contribution to the rotation curve in Fig. 1.2. The flat curve suggests that the mass is not concentrated in the centre where most of the light is, and that large amounts of the mass that cannot be observed reside in the galactic halo.

In the Big Bang Model, after recombination, primordial matter began to clump together due to gravitational instabilities, since most of the matter is in dark matter, hydrogen and helium gas would follow the dark matter distribution as the dark matter clumped to form halos. These halos continue to grow through accretion and mergers, resulting in the large scale structures we observe today. This is known as hierarchical

structure formation, as structure is formed from bottom up, large structures are the result of clumping and merging of smaller structures.

### Halo Mass Function

One way of representing the distribution of dark matter is using the halo mass function, which gives the number of halos per unit volume as a function of the halo mass. The first attempt to theoretically calculate the mass function was made by Press and Schechter (1974), who provided an analytical formalism for structure formation in the non-linear regime. In the Press-Schechter theory, the primordial density perturbations are considered to be Gaussian fluctuations. This Gaussian density field is then smoothed on different mass scales using a spherical top-hat window with radius  $R$ , where  $R$  is related to the mass  $M$  by

$$M = \frac{4}{3}\pi\rho R^3, \quad (1.6)$$

where  $\rho$  is the density. The abundance of halos above a given mass depends on the fraction of space in this smoothed field that exceeds some critical value,  $\delta_c$ . Using this method, approximately half the volume of the Universe in the linear regime will be under dense and never exceed the critical value, since a Gaussian field is used. To fix this, Press and Schechter simply multiplied their expression for the halo mass function by two, which is not very convincing on physical grounds. The extended Press-Schechter Theory was developed to put forward more plausible arguments for the missing factor (Bond et al., 1991).

The halo mass function predicted by the Press-Schechter Theory agrees reasonably well with results obtained from N-body simulations, despite the simple calculations used. The assumptions used in the Press-Schechter formalism have been refined by others to produce better fits to N-body simulations. In Sheth et al. (2001), an ellipsoidal collapse is used instead of the original spherical collapse in Press and Schechter (1974). Jenkins et al. (2001) proposed a fitting formula of the halo mass function for numerical results obtained from a range of N-body simulations. Fig. 1.3 shows a comparison of the various analytical halo mass functions.

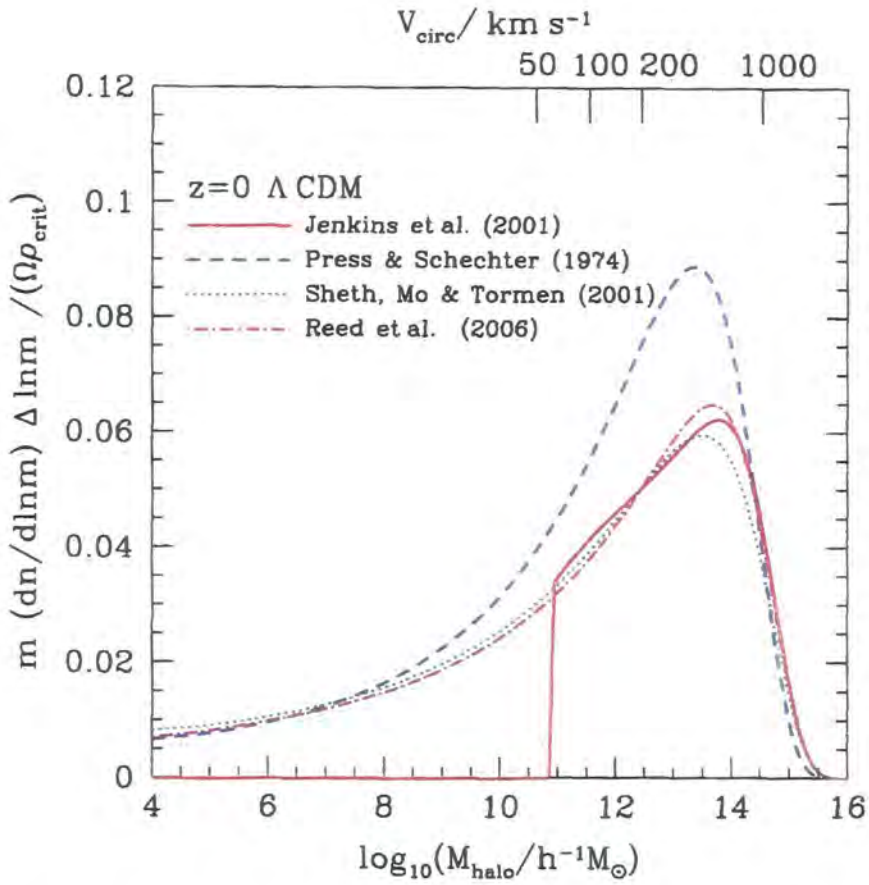


Figure 1.3: The fraction of mass contained in halos of different masses at  $z = 0$ . The Jenkins et al. (2001) curve has a sharp drop-off at  $10^{11} h^{-1} M_{\odot}$  because the fit was obtained using a limited range of masses in a collection of N-Body simulations. This figure is from Baugh (2006).

### 1.1.7 Galaxy Formation

The next step in the evolution of the Universe is to convert the mass into objects, such as stars, that are observed today. Most of the stars are grouped in galaxies, thus we require a theory of galaxy formation to explain the observable universe. In White and Rees (1978), a two-stage model of galaxy formation was first proposed. In this model, dark matter halos are assumed to grow through mergers and accretion, at each stage of the merging hierarchy, dynamical relaxation effects erase any trace of progenitor halos. The luminous contents of galaxies result from the cooling and fragmentation of gas within these dark matter potential wells. In this picture of galaxy formation, structures form mostly hierarchically due to gravitational clustering, this is because most of the matter in the Universe is composed of dark matter and as described in section 1.1.6, interacts with gravitational forces but not electromagnetic forces. The processes involved in galaxy formation are complex and not all are well understood. Below, I will briefly describe some of the more important aspects required in a theory of galaxy formation

#### Gas Cooling

The cooling of gas is central to galaxy formation, as it determines the rate at which material becomes available for star formation. Initially, the gas roughly follows the distribution of the dark matter in halos, as fluctuations in the dark matter separate from the Hubble flow and start to collapse into halos. The gas follows and falls into these dark matter halo potential wells. The gas is heated by shocks as it falls into the dark matter halos. This heating of the gas prevents further collapse as the outward pressure of the gas supports it against the inwards gravitational forces. The gas can now cool via a number of different processes in the hot halo. The two primary mechanisms relevant to galaxy formation are:

1. Emission of photons from transitions between energy levels in atoms. Collision between electrons and atoms excite the atom to higher energy levels, when the excited levels decay, photons are emitted, removing energy and cooling the gas.
2. Bremsstrahlung radiation as electrons accelerate past ions in an ionized plasma.

As the gas cools, the outward pressure decreases and the gas can sink into the centre of the halo as the ingredient for galaxy formation. The gas cooling rate can be affected

by external factors, changing the rate at which galaxy formation proceeds, this will be discussed later in this section.

### Star Formation

Most of what we can observe of galaxies is due to stars, so star formation is an important aspect of galaxy formation. The physics of star formation is very complex and not completely understood, and a wide range of theories for star formation exists. In the context of modelling galaxy formation, a simple estimate is usually made for the global rate of star formation within a galaxy, where the star formation rate,  $\dot{M}_*$ , is calculated using a simple relation such as

$$\dot{M}_* \propto \frac{M_{\text{cold}}}{\tau}. \quad (1.7)$$

where  $M_{\text{cold}}$  is the amount of cold gas available and  $\tau$  is some characteristic timescale.

### Galaxy Mergers

Galaxies are assumed to grow from accretion and mergers following the merging of their parent dark matter halos, as proposed by White and Rees (1978). In this picture, as dark matter halos merge, the former, central galaxies of the smaller halos now become satellite galaxies orbiting a central massive galaxy of the resulting halo. Initially, the satellite galaxies remain separate to the central galaxy. However, as they orbit around the central galaxy in the same dark matter halo, energy is lost through dynamical friction and the satellite galaxies begin to spiral inwards in their orbit.

Galaxy mergers are believed to trigger other important events as well as providing a mechanism for growing galaxies. In violent mergers, where the mass of the satellite is significant, the discs of central spiral galaxies are destroyed, leaving a spheroidal remnant containing all the stars involved. In some other major mergers, the event can trigger a burst of star formation in the galaxy.

### Galaxy Luminosity Function

A successful model of galaxy formation must be able to reproduce the observed galaxy luminosity function. This is the distribution of galaxies within a fixed volume in terms of their luminosity. A galaxy formation model needs to explain the difference between the

halo mass function and the galaxy luminosity function to connect the theory of hierarchical structure formation with the observed Universe. The halo mass function represents the distribution of matter as a result of hierarchical growth, while the luminosity function represents the distribution of galaxies at different luminosities. Naively, one might expect the two to be similar as the amount of mass dictates the formation rate of stars and galaxies. However, the picture of galaxy formation is far more complex, and models of galaxy formation try to explain how different processes connect the halo mass function to the luminosity function. This is illustrated in Fig. 1.4 (Benson et al., 2003), the dashed line is simply the halo mass function converted into a galaxy luminosity function using a constant mass-to-light ratio. It is apparent that this does not agree well with the observed data, this suggests that more complex processes are involved and is one of the motivations for studying the physics of galaxy formation. A commonly used analytical parameterisation of the luminosity function is the Schechter Luminosity Function (Schechter, 1976), and is given by:

$$\phi(L)dL = \phi_* \left( \frac{L}{L_*} \right)^\alpha e^{-L/L_*} \frac{dL}{L_*} \quad (1.8)$$

$\phi(L)dL$  is the number of galaxies per unit volume in a luminosity interval  $L$  to  $L + dL$ .  $\phi(L)_*$  is a normalisation constant for the number of galaxies per unit volume,  $L_*$  is the “characteristic luminosity”, above which the number density of galaxies decreases rapidly, and  $\alpha$  is a dimensionless constant that determines the slope of the luminosity function fainter than  $L_*$ . At  $L < L_*$  the power law term dominates and so the luminosity function depends largely on  $\alpha$ , while for  $L > L_*$  the exponential term dominates and there is a rapid drop in the luminosity function. This is a feature in galaxy luminosity functions believed to be at least in part the result of long cooling time for gas in high-mass halos (White and Rees, 1978), and is known as the “knee” of the luminosity function. We again refer to Fig. 1.4, the dotted line represents a model where only the effects of gas cooling time is considered. This indeed does reproduce the rapid drop in the luminosity function as predicted, but at the expense of creating many more low mass galaxies than observed.

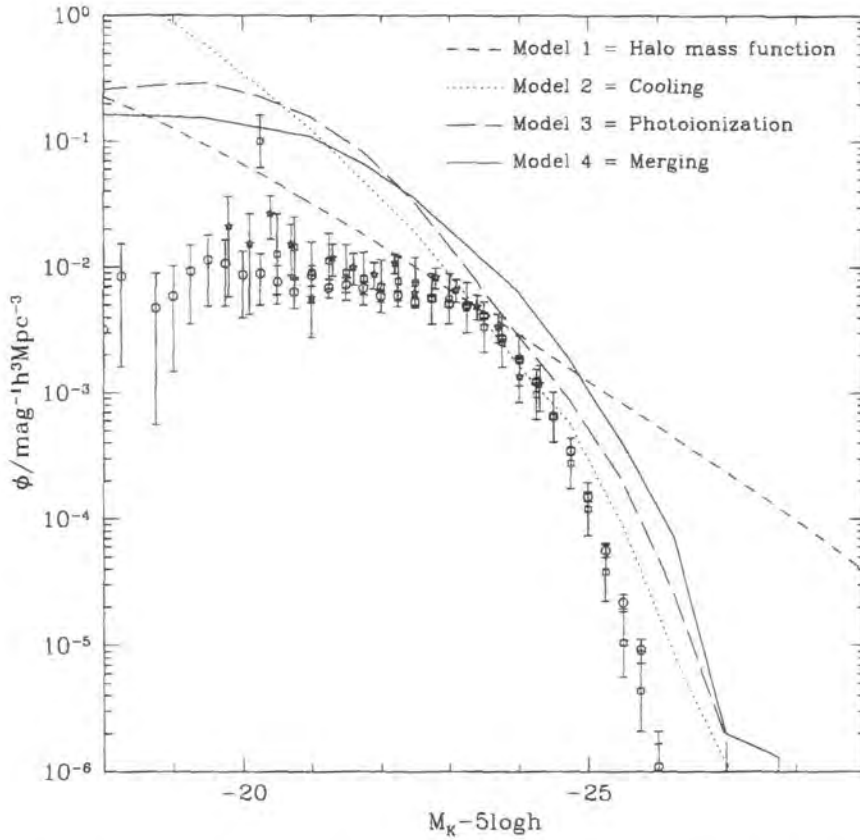


Figure 1.4: K-Band Luminosity function of galaxies from Benson et al. (2003). The points show the observational data while the lines show results from various models. The dashed line shows the result of converting the halo mass function to a luminosity function using a fixed mass-to-light ratio chosen to match the knee of the luminosity function, the dotted line shows a model where only gas cooling is considered. The long-dashed and solid lines show the effect of including photoionization and galaxy merging into the models respectively.

## Feedback processes

The theoretically predicted luminosity function has discrepancies with the observational estimates and is the motivation for including feedback processes in models of galaxy formation. The first discrepancies are in the faint end of the luminosity function, where more low mass galaxies are predicted than observed. To reconcile these differences, the feedback mechanisms considered usually aim to regulate the formation of low mass dwarf galaxies by either suppressing the rate at which the gas cools, or simply removing the cold gas from the galactic disc. A common form of feedback used is modelling supernova driven winds to eject cold gas from the galactic disc. There is observational evidence that supernova driven winds exist in dwarf galaxies (Ott et al., 2005). The gas can be retained in the hot gas halo to be available for “re-cooling” or it can be ejected completely from the halo into the intergalactic medium, leaving it unable to cool to collapse and form stars in galaxies. Some of these mechanisms which delay gas cooling result in the gas cooling at later stages in large dark matter halos. This introduces new problems in the bright end of the luminosity function. The extra material available in large halos creates excess bright galaxies in simulations, and the break around  $L_*$  is not reproduced.

Another form of feedback investigated in galaxy formation models is feedback due to active galactic nuclei (AGN). The large amounts of energy released from an accreting black hole would be significant in suppressing gas cooling in halos. AGN feedback is implemented in galaxy formation models such as those in Croton et al. (2006) and Bower et al. (2006), these models were able to reproduce the observed break in the present day luminosity function.

## 1.2 Reionization

After recombination, the Universe was composed mostly of neutral hydrogen atoms, this contrasts greatly from what we observe today, a highly ionized Universe filled with many complex objects. The epoch of reionization marks the change when a mostly neutral Universe transitions into an ionized Universe. This epoch is of interest because it will allow better understanding of some of the first objects to form. These first objects are believed to have driven reionization as they emitted ionizing radiation to ionize the

intergalactic medium (IGM) around them. The rate at which neutral hydrogen is ionized must exceed the rate at which hydrogen is recombining for a region to reionize. These ionized regions around sources will initially be small, but as more stars are formed and the ionizing luminosity increases, these regions will grow. By studying this era, it will position us better to answer many crucial questions. How were the first stars formed? How massive were these stars? When did the first heavy elements form?

In this section, I will first discuss the current observational constraints, then, some of the current theoretical models will be described. Finally, the 21-cm line signal and its relevance to reionization will be discussed.

### 1.2.1 Observational Constraints

#### Gunn-Peterson Trough

The Gunn-Peterson Trough is a feature observed in spectra of high redshift quasars. Photons with energies near the Lyman alpha wavelength are scattered by hydrogen atoms. The cross-section for this scattering is very high. As photons from distant quasars travel through the IGM, they may pass through regions of neutral hydrogen which scatters photons that have been redshifted into the frequency corresponding to the Lyman Alpha transition. As a result, there would be an absorption feature bluewards of the Lyman alpha line in quasar spectra. The absorption feature becomes stronger as one observes quasars at higher and higher redshifts. This is because the gas in the intergalactic medium is denser at higher redshifts. Eventually, one would expect to observe a trough in the spectrum as the absorption is so strong. This was first observed at a redshift of 6.28 (Becker et al., 2001). Fig. 1.5 shows the spectra of this quasar and also a quasar at lower redshift. This however, is not conclusive evidence that reionization occurred at a  $z \sim 6$ . The scattering cross-section of the  $\text{Ly}\alpha$  transition is very high. This means only a small amount of neutral hydrogen is needed to achieve high levels of absorption. Nevertheless, this sets a lower limit as we know the Universe has become mostly ionized at this time.

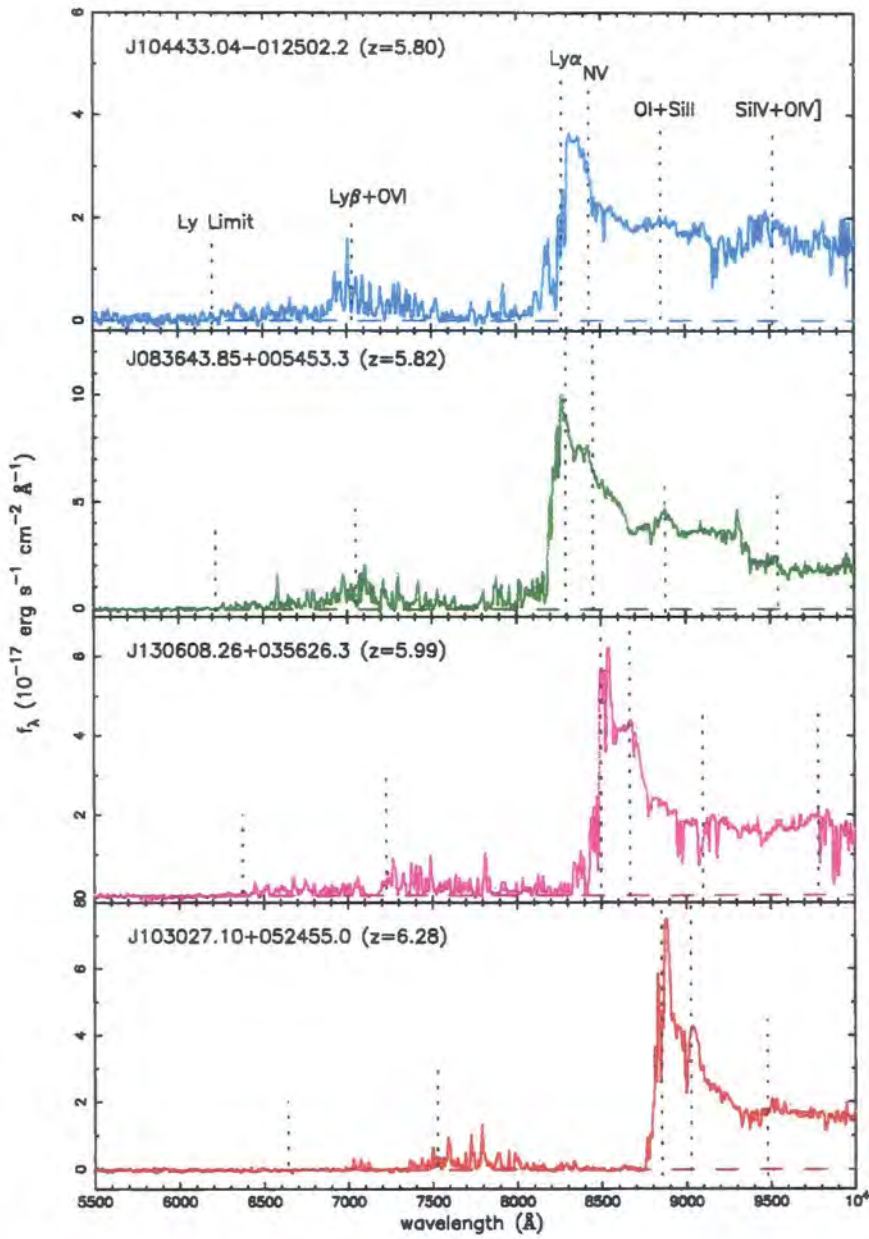


Figure 1.5: Optical spectra of  $z > 5.8$  quasars observed with Keck/ESI, in the observed frame from Becker et al. (2001), the top spectrum of SDSS1044-0125 has been taken from Fan et al. (2000). The Gunn-Peterson trough can be seen to appear bluewards of the Lyman alpha line as redshift increases.

## Effects of Reionization on the Cosmic Microwave Background

The CMB can be analysed to obtain a lot of information on the initial content and also cosmological parameters of the Universe. Reionization can alter the anisotropy spectrum of the CMB, revealing some of the physics during this epoch. As reionization progresses, neutral hydrogen is ionized and free electrons are released into the IGM. The presence of these free electrons causes Thomson scattering of CMB photons. This affects CMB anisotropies in two different ways, it damps the primary temperature anisotropies and also generates secondary large scale polarization anisotropies. The primary anisotropies are damped because the Thomson scattering of CMB photons blends photons from different lines of sight. This effect is characterised by the optical depth parameter,  $\tau$ .

### 1.2.2 Theoretical Models of Reionization

The process of hydrogen reionization can be broadly separated into three stages (Barkana and Loeb, 2001, section 6.3). The initial stage is the “pre-overlap” stage, this is when the ionizing sources are formed and begin to emit ionizing radiation. Typically, the first galaxies would form in the most massive halos that are located in the high density regions. Any ionizing photons that escape the galaxy must first ionize the surrounding high density regions, where the recombination rate of hydrogen is high. Once the ionizing photons get past the high density regions, they propagate much more easily into low density areas. The high recombination rate of the high density regions means that there may be small neutral regions within the larger ionized volume. During this stage of the reionization process, individual highly ionized bubbles surround the first sources, while the rest of the IGM remains neutral.

The middle stage is the “overlap” stage, in this phase, the separate ionized regions grow and neighboring ionized bubbles begin to overlap. This means each point within the connected regions is now exposed to more than one source of ionizing radiation. This increase in ionizing intensity causes high density regions of neutral gas inside the ionized bubble to become ionized as the ionization rate exceeds the recombination rate in these regions. As the ionized regions overlap, it becomes much easier for ionizing photons to travel further, more and more new galaxies that can provide ionizing photons are also being formed, so this stage of reionization is believed to occur rapidly.

The final stage is the “post-overlap” stage, the remaining high density regions that were neutral in the previous stages are gradually ionized. The ionizing intensity continues to grow as galaxy formation proceeds, it also becomes more uniform as the sources are able to reach out to more and more regions of the IGM. Although some neutral gas still remains in collapsed objects, most of the Universe is now ionized and signals the end of the epoch of reionization.

The first sources of light are a big part of theoretical models as reionization is driven by ionizing photons. Only a small amount of gas needs to be converted to luminous objects to have a large effect on reionization, nuclear fusion in stars releases  $7 \times 10^6 \text{eV}$  per hydrogen atom, however, only 13.6eV is required to ionize hydrogen atom. If one considers the possibility of early black holes then reionization can proceed even quicker, thin disc accretion onto a schwarzschild black hole releases ten times more energy than nuclear fusion in stars.

### Population III Stars

Population III stars are metal-free stars and their evolution differs from Population I and II stars that are readily observed. The first stars are believed to be Population III stars because they form from cooling of gas clouds that have not been metal-enriched by supernovae explosions. Although Population III stars have not been observed, it is believed that they exist as the only known mechanism for producing metals is within stars, Hence the first stars to form would be metal-free. The lack of metals means that the CNO cycle cannot occur in these stars, and nuclear fusion can only proceed via the proton-proton chain reaction, which is very inefficient compared to the CNO cycle. Stellar structure and atmosphere models from Tumlinson and Shull (2000) show that the effective temperature of Population III stars is much higher than those of Population I stars, and thus they have a larger effect in ionizing their surroundings.

### Black Holes and Quasars

Formation of black holes and quasars during the epoch of reionization would have a large effect on the reionization history of the Universe. Quasars are more effective at ionizing intergalactic hydrogen than stars because they are brighter and the escape fraction of their ionizing photons is also likely to be higher (Barkana and Loeb, 2001, section

4.2). Given that most galaxies are believed to be hosts of massive black holes, the existence of active black holes during the epoch of reionization would play a large part in reionizing neutral hydrogen. The models in Haiman and Loeb (1999) predict that black holes are expected to exist prior to reionization and their contribution to the ionizing background would be comparable to stars.

### Feedback from Reionization

Towards the end of the “overlap” stage, the ionizing background increases rapidly, ionizing radiation heats the intergalactic medium to temperatures above  $10^4\text{K}$ . The Jeans mass, which is the critical mass at which the inwards gravitational forces of a gas cloud balances the outwards gaseous pressure, increases drastically due to the high temperatures. As a result, the minimum mass required for gas to collapse and form galaxies also increases. Before reionization, the intergalactic medium is cold and the Jeans mass is less of a factor in limiting galaxy formation. After reionization, the heating of the intergalactic medium raises the Jean mass by several orders of magnitude and the Jeans mass becomes a major factor in limiting the formation of stars and galaxies. Numerical simulations such as Thoul and Weinberg (1996) show that for small halos, there is complete suppression of gas infall. The long-dashed line in Fig. 1.4 shows the effect of adding photoionization suppression to a gas cooling only model (dotted line). The luminosity function is flattened in the faint end as formation of low mass galaxies is suppressed. However, this also produces more bright galaxies as more of the gas is now available for galaxy formation in the larger dark matter halos.

## 1.3 21-cm Signal

### 1.3.1 Fundamental Physics of the 21-cm Line

The intergalactic medium of the dark ages consists of mostly neutral hydrogen. The neutral hydrogen is generally in the electron ground state and as a result, unable to produce emission lines by transition of electrons between different orbits. However, it is still possible to detect neutral hydrogen using the 21-cm line. 21-cm radiation is due to a transition between the two hyperfine states in the hydrogen ground state (see the Furlanetto et al. (2006) review for an in depth discussion of the 21-cm line in the high-redshift

Universe). Hyperfine splitting is caused by the weak magnetic interaction between the electrons and nuclei. In the hydrogen atom, there are two possible states, since both the electron and proton have a spin of  $\frac{1}{2}$ , corresponding to two allowed values of the spin quantum number,  $\pm\frac{1}{2}$ , the spins of the electron and the proton can either be aligned in the same direction (in parallel), or opposite directions (antiparallel). The state where the spins are parallel is at a slightly higher energy level than the state where the spins are in anti parallel, the energy difference between the levels is  $5.9 \times 10^{-6}\text{eV}$ , corresponding to a wavelength of approximately 21-cm. This transition of the hyperfine spin states occurs with an extremely small probability of  $2.9 \times 10^{-15}\text{s}^{-1}$  and so the emission of a 21-cm photon from a single neutral hydrogen is extremely rare. This transition is not observed in laboratories on Earth, due to collisional de-excitation. However, in the intergalactic medium, the large number of hydrogen atoms present and the low density means it is possible to observe the 21-cm emission line with radio telescopes.

The emission or absorption of 21-cm photons from neutral hydrogen gas is governed by the spin temperature,  $T_S$ , defined via:

$$\frac{n_1}{n_0} = \frac{g_1}{g_0} e^{-E_{10}/k_B T_S} = 3e^{-T_*/T_S} \quad (1.9)$$

where  $n_1$  and  $n_0$  are the relative number densities of atoms in the two hyperfine levels,  $g_0$  and  $g_1$  are the statistical weights,  $E_{10}$  is the energy splitting of the two levels,  $k_B$  is the Boltzmann constant and  $T_* = E_{10}/k_B$ . Here,  $g_0 = 1$  and  $g_1 = 3$ . From eq. (1.9) we can see that the relative number densities depend only on  $T_S$ . However, during reionization,  $T_S \gg T_*$ , and so we can expect three out of four neutral hydrogen atoms to be in the excited state if no other external effects are considered.

This spin flip transition in neutral hydrogen quickly enters equilibrium with background CMB photons, coupling  $T_S$  to the CMB temperature,  $T_{\text{CMB}}$ . As an observer, this would mean 21-cm photons would not be visible against the CMB background.  $T_S$  needs to be decoupled from  $T_{\text{CMB}}$  via some mechanism for 21-cm photons to be observable.

### 1.3.2 Spin Temperature

Observationally, the 21-cm signal is seen against the CMB background. The quantity one measures is the differential brightness temperature,  $\delta T_b$  (see section 4.3.1).  $\delta T_b$  is given

by (e.g. Mellema et al. (2006, eq. 1))

$$\delta T_b = \frac{T_S - T_{\text{CMB}}}{1+z} (1 - e^{-\tau}), \quad (1.10)$$

where  $\tau$  is the optical depth of a cloud of hydrogen. Therefore, the variation of  $T_S$  from  $T_{\text{CMB}}$  will determine whether the 21-cm signal will be observable, and if so, whether it will appear in emission or absorption. There are three processes that determine  $T_S$ :

1. Absorption of CMB photons,
2. Collisions with other hydrogen atoms, free electrons and other particles, and
3. "Ly $\alpha$  pumping" via the Wouthuysen-Field Effect.

The absorption of CMB photons will drive  $T_S$  towards  $T_{\text{CMB}}$  causing the 21-cm signal to become unobservable. The relation between  $T_S$ ,  $T_{\text{CMB}}$  and the gas kinetic temperature,  $T_K$  can be written as (Furlanetto et al., 2006, eq. 23)

$$1 - \frac{T_{\text{CMB}}}{T_S} = \frac{y_\alpha + y_c}{1 + y_\alpha + y_c} \left( 1 - \frac{T_{\text{CMB}}}{T_K} \right), \quad (1.11)$$

where  $y_\alpha$  and  $y_c$  are the coefficients for radiative and collisional coupling respectively.

For collisional coupling,  $y_c$  for species  $i$  is (Furlanetto et al., 2006, eq. 24)

$$y_c^i = \frac{n_i \kappa_{10}^i T_\star}{A_{21} T_{\text{CMB}}}, \quad (1.12)$$

where  $n_i$  is the number density of the species,  $\kappa_{10}^i$  is the rate coefficient for spin de-excitation in collisions with that species and  $A_{21}$  is the Einstein coefficient for spontaneous emission for the 21-cm line. The values of  $\kappa_{10}^i$  are tabulated in Zygelman (2005) for hydrogen-hydrogen collisions and Furlanetto and Furlanetto (2007) for electron-hydrogen collisions. This is summarised in Fig. 1.6. As is seen in Fig. 1.6,  $\kappa_{10}^{eH} \gg \kappa_{10}^{HH}$ . However, the net rates are proportional to densities so H-H collisions dominate in the early Universe when the ionized fraction is very small. Neutral helium contains a full outer shell of electrons in the ground state. The Pauli exclusion principle prevents any spin change via electron exchange unless the helium atom is excited to the triplet state. This requires much more energy than the cold neutral intergalactic medium can provide at early times. Other species are generally unimportant due to their rarity. The H-H collisional coupling is considered important at high redshifts (Nusser, 2005) and in dense regions (Ciardi and Madau, 2003). However, the effect of Ly $\alpha$  photon pumping is the most dominant effect and is described in the next section.

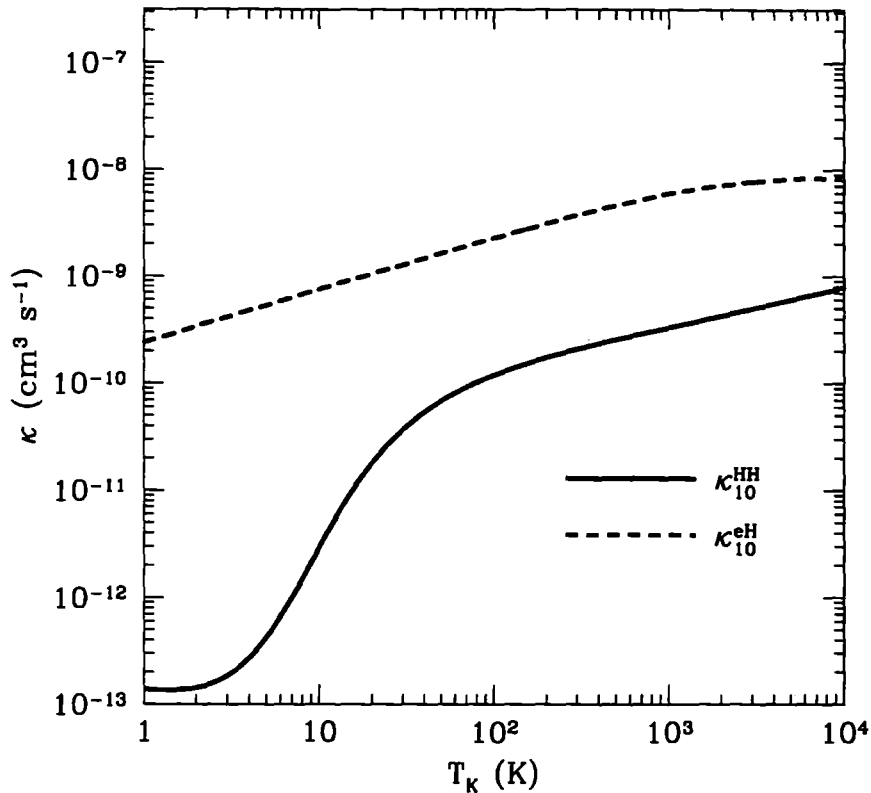


Figure 1.6: De-excitation rate coefficient for hydrogen-hydrogen and electron-hydrogen collisions. Note that net rates are proportional to densities, so H-H collisions still dominate in a weakly-ionized medium. Figure from Furlanetto et al. (2006)

### 1.3.3 The Wouthuysen-Field Effect

The Wouthuysen-Field effect (Wouthuysen, 1952; Field, 1959) allows the hydrogen atom to switch to the higher energy spin state via absorption and spontaneous re-emission of Ly $\alpha$  photons. This is illustrated in Fig. 1.7. For a hydrogen atom in the hyperfine singlet state ( $1_0S_{1/2}$ , using the notation  $n_F L_J$ , where  $n$  is the energy level,  $F$  is the total angular momentum,  $L$  and  $J$  are the orbital and total angular momentum of the electron respectively), on absorption of a Ly $\alpha$  photon, the electric dipole selection rules allow  $\Delta F = 0, 1$ , except  $F = 0 \rightarrow 0$  is prohibited. The atom will therefore jump to either the  $2_1P_{1/2}$  or  $2_1P_{3/2}$  state as indicated by the solid lines in Fig. 1.7. Using the same rules, the atom can now decay to either of the  $1S$  states, again indicated by the solid lines. Thus, through the absorption and spontaneous re-emission of Ly $\alpha$  photons, some of the neutral hydrogen atoms change hyperfine states, increasing the number of atoms capable of 21-

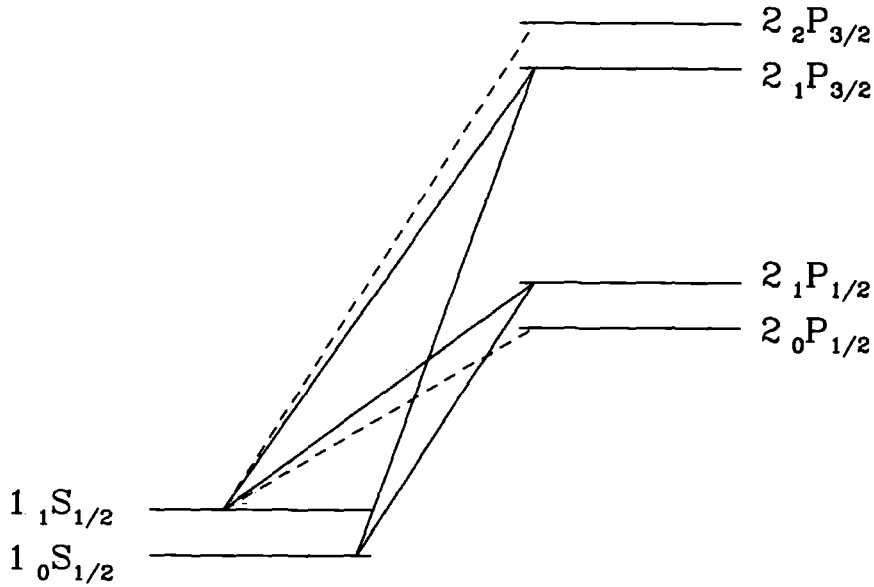


Figure 1.7: Level diagram illustrating the Wouthuysen-Field effect, The hyperfine splittings of the 1S and 2P levels are shown. The solid lines label transitions that mix the ground state hyperfine levels, while the dashed lines label complementary transitions that do not participate in mixing. From Pritchard and Furlanetto (2006).

cm emission.

$\text{Ly}\alpha$  pumping is very efficient at bringing  $T_S$  towards  $T_K$  for the following reasons. Firstly, the  $\text{Ly}\alpha$  scattering cross section is very high, a  $\text{Ly}\alpha$  photon will scatter many times before redshifting out of resonance. Secondly,  $\text{Ly}\alpha$  photons emitted from stellar sources can reach far beyond surrounding ionized regions. During the early stages of reionization, UV photons emitted from stellar sources with sufficient energies ( $h\nu > 13.6\text{eV}$ ) are likely to be used in ionizing the surrounding neutral hydrogen gas.  $\text{Ly}\alpha$  continuum photons with  $10.2\text{eV} < h\nu < 13.6\text{eV}$  will travel unimpeded until they are redshifted to  $h\nu \approx 10.2\text{eV}$ , where they can be captured by neutral hydrogen atom in the  $\text{Ly}\alpha$  line. Under these circumstances, the photon can travel about  $350h^{-1}\text{Mpc}$  at  $z \approx 20$  (Nusser, 2005), and since stars emit at least 4 times as many  $\text{Ly}\alpha$  continuum photons than UV photons (e.g. Ciardi and Madau (2003)), one would expect  $\text{Ly}\alpha$  photons to travel much further than the surrounding ionized regions, contributing to the Wouthuysen-Field effect.

## 1.4 Motivation for this work

As described in section 1.1, very little is known about the Universe during the epoch of reionization. A better understanding of this period will help to connect what we already know about the very early Universe (from particle physics) to what we observe today. Detecting the 21-cm signal is one of the most direct methods of probing this epoch. It contains information about the neutral content of the Universe that we have limited knowledge about. One of the motivations to simulate 21-cm signal now is that large radio observatories are being built, with one of the goals being to observe these signals directly. With mock images and spectra from simulations, these can be compared with observations, testing current theories of reionization. The planned projects that have goals of observing the 21-cm signal are:

- **LOFAR**<sup>1</sup>: The Low Frequency Array for Radio Astronomy is an array of radio telescopes currently under construction in Europe, with the core located in Netherlands and various stations spread across other different countries. LOFAR will perform sky surveys over a frequency range of approximate 40 – 240MHz. It is expected to finish construction in 2009.
- **PaST/21CMA**<sup>2</sup>: The Primeval Structure Telescope also known as the 21 centimetre Array, is located in a remote location in north western China. The array has an angular resolution of 4 armin and will be able to capture radio images of the sky in the frequency range of 50 – 200MHz. A quarter of the array has already been built and has begun to collect 21-cm signal.
- **MWA**<sup>3</sup>: The Muchison Widefield Array is located in western australia. The MWA will be able to survey the sky for 21-cm signal in the range of 80 – 300MHz. It will not have enough sensitivity to image individual features in the 21-cm signal, but it has a large effective field of view and statistical quantities can be measured as well as detecting large ionized “bubbles”.
- **SKA**<sup>4</sup>: The Square Kilometre Array is a large ambitious project in development that

---

<sup>1</sup><http://www.lofar.org/>

<sup>2</sup><http://web.phys.cmu.edu/past/>

<sup>3</sup><http://www.haystack.mit.edu/ast/arrays/mwa/>

<sup>4</sup><http://www.skatelescope.org/>

will have a total collecting area of approximately one square kilometre. The SKA is planned to have a very large field of view, with a goal of 200 square degrees at frequencies below 1GHz and more than 1 square degree at higher frequencies. The SKA will have a compact core containing half its collecting area within a diameter of 5km, with a surrounding spiral network of stations covering a continent.

Of these projects, the SKA is the largest and will have the best sensitivity. However, due to the size of the project, initial observations are scheduled for 2016 and SKA will not be fully functional until 2020. LOFAR provides an intermediate stepping stone to SKA, also, the involvement of the UK scientific community in the LOFAR project makes it a suitable choice to focus our efforts on.

The LOFAR project has a number of science goals. The one that interests us is studying the Epoch of Reionization using the redshifted 21-cm line. For this purpose, LOFAR will have a frequency range of 115Mhz to 180Mhz, corresponding to  $z = 11.4$  to  $z = 6$  for redshifted 21-cm photons, and a field of view of 5 degrees. LOFAR will attempt to answer the following questions about the Epoch of Reionization:

- At what redshift does the bulk of neutral hydrogen become ionized? Does this process happen rapidly such that a clear “Redshift of Reionization” be identified, or is reionization an extended process that happens in multiple stages?
- What are the characteristics of the spatial distribution of the neutral and ionized material during this epoch and how do these evolve?
- What are the main objects that drive reionization?

This work aims to be complementary to the LOFAR project. By simulating the 21-cm signal, mock images and spectra can be made, features in these images and spectra can be associated with the physical processes in the underlying model. This will be useful when studying the real, observed data that may have features similar to those of the mock images.

The layout of this thesis is as follows. In chapter 2, the GAGDET-2 N-body simulation code and the GALFORM semi-analytical model of galaxy formation used to simulate the Universe are described. The N-body simulations ran for the purpose of this thesis are presented.

In chapter 3, the ionizing emissivities as a function of halo mass for a range of simulations are investigated. The implications of these results for the mass resolution and simulation volume required in simulations are discussed. The effect of varying a GALFORM parameter controlling the suppressing of gas cooling in low mass halos is also investigated.

A brief review of the current status of 21-cm signal simulations is first given in chapter 4. We then develop a method to calculate the 21-cm signal and identify ionized regions to generate 21-cm signal maps. Images, line-of-sight spectra and power spectra calculated from these 21-cm maps are discussed.

Finally, in chapter 5, a summary of the main conclusions of this thesis is presented. Possible areas for future research are also identified in this chapter.



# Chapter 2

## *Tools for simulating the Evolution of the Universe*

### 2.1 Introduction

The emergence of modern computers and their increasing computational power plays a large role in modern cosmology. Unlike many other branches of physics where experiments can often be carried out to investigate natural phenomena, in cosmology, it is impossible, for example, to build a galaxy in a laboratory and test how it reacts by changing the conditions surrounding it. Traditionally, astronomical observations were the only source of information about the Universe. However, due to the large timescales over which structures form, it is impossible during one lifetime to observe the evolution of a single galaxy from its birth to death. Nowadays, computational simulations are very important in building theoretical models to help understand the evolution of the Universe. These simulations are a cosmologist's sandbox, allowing us to modify parameters and observing the outcome, very much like a classical experimentalist would do.

To simulate 21-cm emission, one first needs information on the neutral hydrogen from which the radiation is emitted. How is the hydrogen distributed? What is the ionization state of the hydrogen atoms?

In this chapter, I describe the computational tools used in this thesis to simulate the evolution of the distribution of matter, and also to predict where the galaxies, sources of ionizing radiation, are formed. Both of which provide essential information used to simulate the 21-cm signal. At the end of the chapter, I will describe my own application

of these tools.

## 2.2 N-Body Simulations

N-Body simulations simulate the movement of multiple particles according to the gravitational force that acts on them. These are a great tool in cosmology for simulating the non-linear growth of structure in the universe, providing a link between initial conditions of the dark matter to the structures observed today. Cosmological N-body problems in essence are very simple in that only one force, gravity, is considered between the particles. In practice, however, the calculations quickly become very complex as the number of particles used becomes large, to achieve a desirable mass resolution. These simulations are therefore very computationally intensive and have only been possible due to the advances in computational power. A recent large N-Body simulation is the Millennium Simulation. This is a dark matter only simulation with  $2160^3$  particles in a comoving box of volume  $500h^{-1}\text{Mpc}^3$  (Springel et al., 2005). Simulations like the Millennium help us to understand the formation of large scale structures. They also provide valuable information on the distribution of matter that are useful in studying objects at smaller scales, such as galaxies.

There are many different codes using a range of algorithms to run N-Body simulations. The GADGET-2 code (Springel, 2005), utilising a combination of a tree and a particle-mesh algorithm, was used in this study. In this section, the GADGET-2 code and the algorithms used to simulate the gravitational forces will be described.

### 2.2.1 GADGET-2

The GADGET-2 code (Springel, 2005) is a cosmological N-Body simulation code. It is an improved version of the GADGET code (Springel et al., 2001) used in the Millennium simulation. GADGET-2 is capable of both dark matter and smoothed particle hydrodynamics (SPH) simulations. Lean-GADGET-2 (L-GADGET2) is a specialised version of the GADGET-2 code intended for large, dark matter only simulations, and is the version used in this thesis. Any mention of GADGET-2 in the remainder of this thesis refers to L-GADGET2.

### Initial Conditions

To start a N-Body simulations, we need to specify the initial positions and velocities of the particles. These initial conditions should follow from the predictions of linear perturbation theory, which can be specified by the linear power spectrum. The method used to create these initial conditions is to perturb a uniform particle distribution using the Zel'dovich approximation (Zel'Dovich, 1970). In the simulations presented in this study, a Gaussian random field is generated by perturbing a homogeneous, "glass" particle distribution and assigning to them velocities according to the solutions of linear theory. Each mode is assigned a random phase and the power for each mode is selected at random from an exponential distribution with the mean power corresponding to the linear power spectrum. This power spectrum used was calculated numerically for specified cosmological constants using the code CMBFAST (Seljak and Zaldarriaga (1996), details of setting up initial conditions relevant to this study will be provided in section 2.4). The process of generating the initial conditions was done by the program, N-GENiC. This was provided generously by Volker Springel, the author of GADGET-2.

### Gravitational Calculations

L-GADGET2 uses a TreePM algorithm to compute the gravitational forces in the N-Body system. This is a combination of using a tree algorithm to calculate short range gravitational forces while using a particle-mesh (PM) method to calculate the long range forces. The basic equations solved in GADGET, as presented in Springel (2005), are summarized here. The dynamics of particles in the simulation can be described by the Hamiltonian in comoving coordinates,

$$H = \sum_i \frac{\mathbf{p}_i^2}{2m_i a(t)^2} + \frac{1}{2} \sum_{ij} \frac{m_i m_j \varphi(\mathbf{x}_i - \mathbf{x}_j)}{a(t)}, \quad (2.1)$$

where  $H = H(\mathbf{p}_1, \dots, \mathbf{p}_N, \mathbf{x}_1, \dots, \mathbf{x}_N, t)$ .  $\mathbf{x}_i$  are comoving vectors and  $\mathbf{p}_i = a^2 m_i \dot{\mathbf{x}}_i$  are the corresponding canonical momenta. Assuming periodic boundary conditions for a cube of size  $L^3$ , the interaction potential  $\varphi(x)$  is the solution of

$$\nabla^2 \varphi(x) = 4\pi G \left[ -\frac{1}{L^3} + \sum_n \delta(\mathbf{x} - \mathbf{n}L) \right], \quad (2.2)$$

where the sum over  $\mathbf{n} = (n_1, n_2, n_3)$  extends over all integer triplets. For this discretized particle system, the peculiar potential,  $\phi(\mathbf{x})$ , is defined as

$$\phi(\mathbf{x}) = \sum_i m_i \varphi(\mathbf{x} - \mathbf{x}_i). \quad (2.3)$$

A softening factor is required so that particles act as spheres rather than point objects. In GADGET-2, a spline kernel is used for this purpose, and  $\tilde{\delta}(x) = W(|x|, 2.8\epsilon)$ , where  $W$  is given by

$$W(r, h) = \frac{8}{\pi h^3} \begin{cases} 1 - 6 \left(\frac{r}{h}\right)^2 + 6 \left(\frac{r}{h}\right)^3, & 0 \leq \frac{r}{h} \leq \frac{1}{2}, \\ 2 \left(1 - \frac{r}{h}\right)^3, & \frac{1}{2} < \frac{r}{h} \leq 1, \\ 0, & \frac{r}{h} > 1 \end{cases} \quad (2.4)$$

The values chosen for  $r$  and  $h$  here give the Newtonian potential of a point mass at zero lag in non-periodic space as  $-\frac{Gm}{\epsilon}$ , the same as for a Plummer sphere of size  $\epsilon$ . For particle separations larger than  $2.8\epsilon$ , the forces are fully Newtonian. The softening factor prevents the formation of hard binaries and allows for integration of close particle encounters with low-order integrators.

In Fourier space, the potential of eq. (2.3) can be split explicitly into a long-range and short range part according to  $\phi_k = \phi_k^{\text{long}} + \phi_k^{\text{short}}$ , where

$$\phi_k^{\text{long}} = \phi_k \exp(-\mathbf{k}^2 r_s^2), \quad (2.5)$$

with  $r_s$  describing the spatial scale of the force split. The short-range part of the potential can be solved in real space for  $r_s \ll L$ , and the short-range potential is given by

$$\phi^{\text{short}}(\mathbf{x}) = -G \sum_i \frac{m_i}{r_i} \operatorname{erfc}\left(\frac{r_i}{2r_s}\right). \quad (2.6)$$

Here,  $r_i = \min(|\mathbf{x} - \mathbf{r}_i - \mathbf{n}L|)$  is defined as the smallest distance of any of the images of particle  $i$  to the point  $\mathbf{x}$ .

The tree part of the algorithm employs a Barnes and Hut tree construction scheme (Barnes and Hut, 1986) to calculate the potential in eq. (2.6). The simulation volume is divided into eight equal, smaller cubic cells, and each of these cells are further divided into another eight cells and so on until there is only one particle residing in a cell, any empty cells can be discarded. This forms an oct-tree structure where the cubes containing exactly one particle are the nodes of the tree. Therefore, each node in the oct-tree either contains exactly one particle, or is a progenitor to further nodes and carries the monopole

and quadrupole of all particles lying within the cell. The objective of building an oct-tree is so that while forces of nearby particles can be computed directly, particles in distant cells can be treated as just a single large particle, with all the mass in the cell placed at the centre of mass of that cell. The accuracy of the tree algorithm is adjusted with a relative cell opening criterion in GADGET-2:

$$\frac{GM}{r^2} \left(\frac{l}{r}\right)^2 \leq \alpha|\mathbf{a}|, \quad (2.7)$$

where  $G$  is the gravitational constant,  $M$  is the mass of the node,  $r$  is the distance to extension  $l$ ,  $|\mathbf{a}|$  is the size of the total acceleration obtained in the previous time-step, and  $\alpha$  is a tolerance parameter. Springel (2005) notes that large errors are possible in tree codes using standard opening criteria, as first pointed out in Salmon and Warren (1994). These errors occur when the distance to the nearest particle in a node becomes very small. An additional opening criterion is imposed in GADGET-2 to avoid this situation:

$$|r_k - c_k| \leq 0.6l, \quad (2.8)$$

where  $r$  is the particle coordinate and  $c$  is the geometric centre of the node. This criterion is applied separately for each coordinate axis,  $k$ . As the force computation walks through the tree, it checks each node with the above criteria (equations (2.7) and (2.8)). If the criterion is fulfilled (i.e. the cell in question is distant enough) then the walk along this branch can be terminated at this node, otherwise, the cell is opened and the walk continues with the newly opened nodes.

To compute the PM part of the force, given by eq. (2.5), GADGET-2 first uses a cloud-in-cells assignment to construct a mass density field - mass of each particle is distributed to the nearest eight grid points, weighted depending on the distance from each grid point. The gravity potential at each grid point can then be determined using Fourier transform techniques, and the forces on the mesh are approximated by finite differencing the potential. Finally, the forces are interpolated to the position of the particles, again using a cloud-in-cell assignment. For details of the TreePM algorithm, please refer to the original GADGET-2 paper (Springel, 2005).

The combination of these two methods of computing the force is very powerful. The two methods complement one another. On one hand, the tree calculates short range forces accurately but only approximates long range force, on the other hand, the PM is

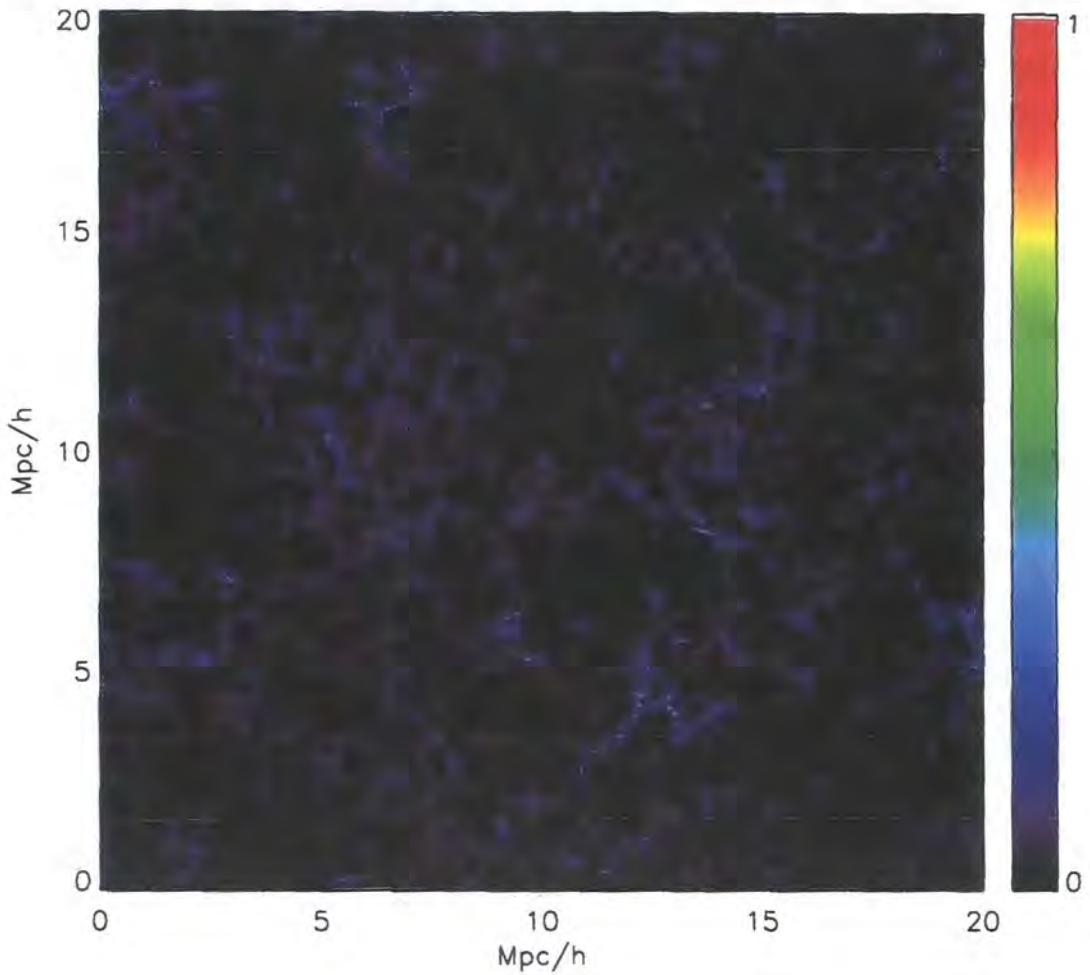


Figure 2.1: A 2D slice from a  $512^3$  grid from a L-GADGET2 simulation box showing the distribution of dark matter at  $z \sim 14$ . The colour scale is normalised to the pixel with the highest density. Note the filamentary structure resulting from hierarchical structure growth.

accurate in long range forces but does not model close interactions between particles well. When compared to a pure tree method, the performance of the code is improved. Since long range forces are computed using a PM, only a small part of the tree corresponding to the region around each particle needs to be considered for the short range forces. The output of a GADGET-2 snapshot lists the positions of the simulation particles. The particle positions can be interpolated on to a regular grid to construct a density grid, an example is shown in Fig. 2.1. A clouds-in-cells assignment was used to interpolate onto a  $512^3$  grid in this case.

### 2.3 GALFORM: A semi-analytical model

The next step after running a dark matter only N-Body simulation is to locate the ionizing sources and determining their luminosities, a range of different techniques can be applied for this purpose. The most straightforward approach is to simply to assign a mass to light ratio to haloes identified in the N-Body simulation, as in done in some simulations (e.g. Iliev et al. (2006); Zahn et al. (2007)). This would be easy to calculate but would not be a great representation of the physical universe. At the other end of the scale, a direct numerical simulation of the gas dynamics can be carried out. This would give a much more accurate picture, but would require a lot of computing power at high resolutions. A technique that has become popular in recent years is to use semi-analytical modelling. In this approach, the baryonic component of galaxy formation is calculated using analytical models, while the evolution of dark matter is calculated using either N-Body methods or Monte-Carlo techniques. In this thesis, GALFORM was used for the semi-analytical modelling. The GALFORM galaxy formation model is a combination of many different techniques to treat different aspects in the complex process of galaxy formation. The full range of properties and processes modelled within GALFORM as presented in Cole et al. (2000) are:

1. the gravitationally driven formation and merging of dark matter haloes;
2. the density and angular momentum profiles of dark matter and shock-heated gas within dense non-linear haloes;
3. the radiative cooling of gas and its collapse to form centrifugally supported discs;
4. the scalelengths of discs based on angular momentum conservation and including the effect of the adiabatic contraction of the surrounding halo during the formation of the disc;
5. star formation in discs;
6. feedback, i.e. the regulation of the star formation rate resulting from injection of supernova energy into the interstellar medium;
7. chemical enrichment of the interstellar medium and hot halo gas, and its influence on both the gas cooling rates and the properties of the stellar populations that are

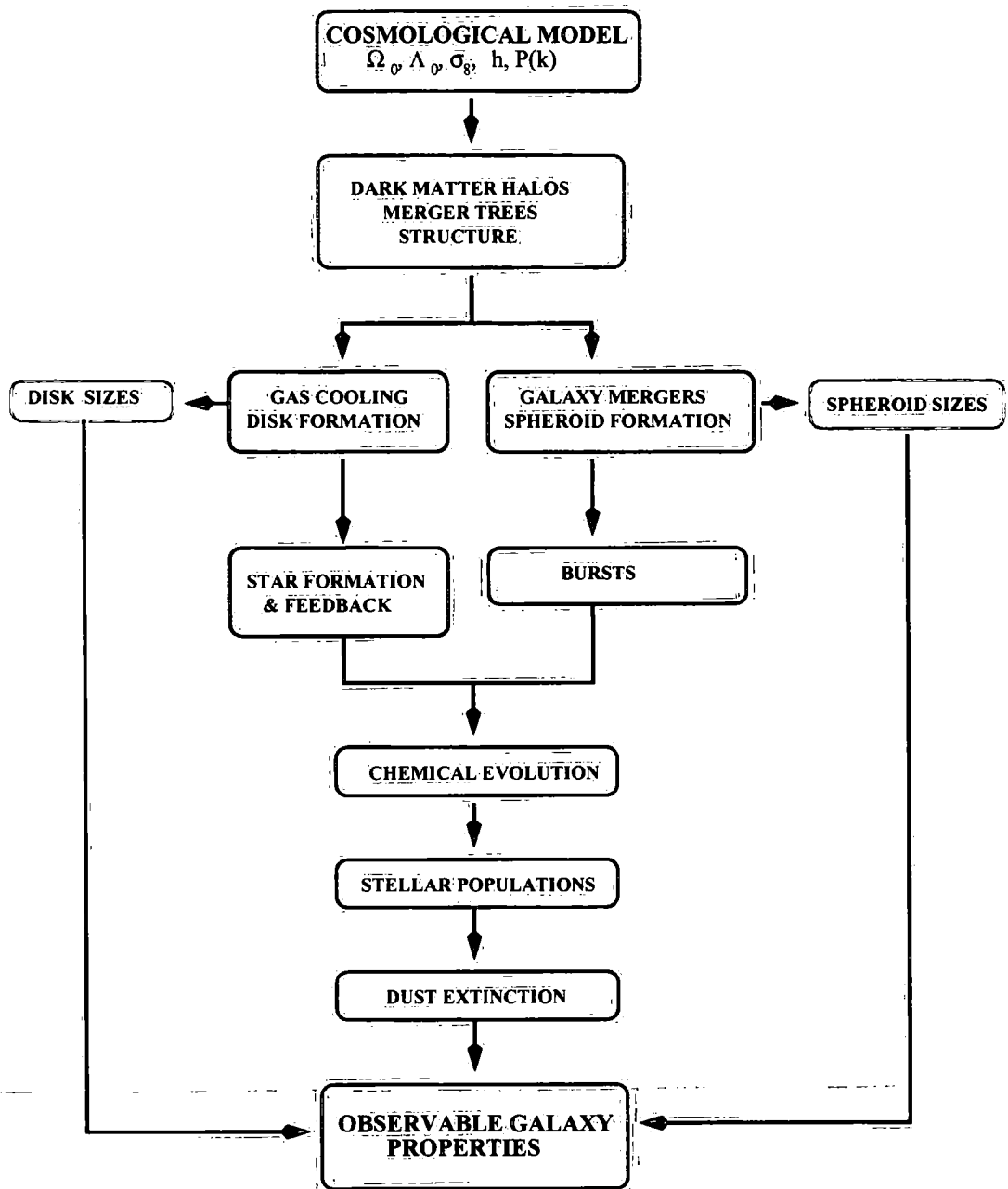


Figure 2.2: A schematic diagram show how the different physical processes are combined in GALFORM to make predictions for observable properties. Figure is an adapted version of the original version in Cole et al. (2000), from Baugh (2006).

- formed;
8. Galaxy mergers resulting from dynamical friction operating on galaxies as they orbit within common dark matter haloes;
  9. the formation of galactic spheroids, accompanied by bursts of star formation, during violent galaxy-galaxy mergers, and estimates of their effective radii;
  10. spectrophotometric evolution of the stellar populations;
  11. the effect of dust extinction on galaxy luminosities and colours, and its dependence on galaxy inclination, and
  12. the generation of emission lines from interstellar gas ionized by young stars.

Fig. 2.2 shows a schematic diagram summarizing the above list. The full details of the GALFORM models can be found in the related papers (e.g. Cole et al. (2000); Benson et al. (2003); Baugh et al. (2005)). Here, I will summarise briefly the treatment of gas cooling, star formation and feedback, as these can strongly affect the epoch of reionization and so are of special interest to us. The specific GALFORM model used in this study is the model presented in Baugh et al. (2005). This model has the goal of improving predictions for galaxy populations at high redshifts, making it an appropriate choice for studying the epoch of reionization.

### Gas Cooling

In GALFORM, the gas in a halo is assumed to have a spherical distribution with the density profile,

$$\rho_{\text{gas}}(r) \propto \frac{1}{r^2 + r_{\text{core}}^2}. \quad (2.9)$$

The hot, shock-heated halo gas is assumed to be in collisional ionization equilibrium. The cooling time,  $\tau_{\text{cool}}$  is given by

$$\tau_{\text{cool}}(r) = \frac{3\mu m_{\text{H}}}{2} \frac{kT_{\text{gas}}}{\rho_{\text{gas}} \Lambda(T_{\text{gas}}, Z_{\text{gas}})}, \quad (2.10)$$

where  $\rho_{\text{gas}}$  is the density of the gas at radius  $r$ ,  $T_{\text{gas}}$  is the temperature and  $Z_{\text{gas}}$  is the metallicity. The tabulated cooling function,  $\Lambda(T_{\text{gas}}, Z_{\text{gas}})$ , of Sutherland and Dopita (1993) is used. The amount of gas that has cooled is estimated by calculating the cooling

radius  $r_{\text{cool}}$ . This is the radius at which the cooling time of the gas is equal to the age of the halo. For the gas to be accreted onto the central disk, it must also have sufficient time to fall to the centre of the halo, giving a free-fall radius,  $r_{\text{ff}}$ . At the beginning and end of one time-step,  $r_{\text{min}}(t)$  is determined by the smaller value of  $r_{\text{cool}}$  and  $r_{\text{ff}}$ . The mass that is added to the disk in a time-step is then the mass of hot gas in a spherical shell, defined by  $r_{\text{min}}$  at the beginning and end of that time-step.

### Star Formation and Supernova Feedback

GALFORM models star formation by considering three simultaneous processes,

1. Gas cooling from the hot halo gas and accreting on to the galactic disk,
2. the star formation from the resulting cold gas and
3. the reheating and ejection of gas.

The first process, cooling, has been described above. The second process, star formation, takes place in galactic disks at a rate  $\psi$ , given by

$$\psi = \frac{M_{\text{cold}}}{\tau_{\star}}, \quad (2.11)$$

where  $M_{\text{cold}}$  is the mass of the cold gas and  $\tau_{\star}$  is the star formation timescale. Stellar feedback is modelled by assuming that cold gas in the disk is reheated by energy from stars and supernovae, and ejected from the disk. The rate of this is given by  $\dot{M}_{\text{eject}}$ , as a function of  $\psi$  and the feedback efficiency,  $\beta$ ,

$$\dot{M}_{\text{eject}} = \beta\psi. \quad (2.12)$$

$\tau_{\star}$  and  $\beta$  depend on the properties of the galactic disk and are defined as below:

$$\tau_{\star} = \tau_{\star 0} \left( \frac{V_{\text{disk}}}{200 \text{ km s}^{-1}} \right)^{\alpha_{\star}} \quad (2.13)$$

$$\beta = \left( \frac{V_{\text{disk}}}{V_{\text{hot}}} \right)^{-\alpha_{\text{hot}}}, \quad (2.14)$$

where  $V_{\text{disk}}$  is the circular velocity of the galactic disk and  $V_{\text{hot}}$  is a parameter.  $\tau_{\star 0}$  is a constant and  $\alpha_{\star}$  and  $\alpha_{\text{hot}}$  are dimensionless parameters. Two additional parameters, the yield,  $p$ , and the recycled fraction,  $R$ , that are related to the IMF are also needed.  $p$  determines the fraction of mass converted into stars and returned to the interstellar

medium as metals, and  $R$  is the mass recycled by stars via winds and supernovae. A set of coupled, differential equations are formulated by considering the rate of transfer of matter between cold gas, hot gas and stars. Solving these equations at each time step gives the change in mass and metal content in the gas and stars. The details of these equations and how to solve them are given in section 4.2 and Appendix B of Cole et al. (2000).

### Photoionization Feedback

A simple approach is taken to model the feedback from photoionization of the intergalactic medium. As described in section 1.2.2, ionization of the intergalactic medium limits the gas infall rate, especially for low mass halos. In the GALFORM model, this is modelled by assuming at redshifts of  $z_{\text{cut}} < 6$ , no gas cools in halos with circular velocities  $V_{\text{cut}} < 60\text{kms}^{-1}$ .  $z_{\text{cut}}$  and  $V_{\text{cut}}$  are adjustable parameters in the model.  $z_{\text{cut}}$  corresponds to the redshift when the abundance of ionizing photons in the intergalactic medium is sufficient to suppress low mass halos through photoionization feedback. This would occur during reionization so  $z_{\text{cut}}$  should be set similar to the redshift of reionization,  $z_{\text{reion}}$ . This prescription suppresses star formation in these low mass halos.

### Constraints on parameters

Although the GALFORM model used has the aim of improving predictions at high redshifts, it follows the philosophy that the model should first be able to reproduce basic properties of local galaxy populations. As such, many of the parameters are constrained by observational data. The constraints used to fix the main parameters introduced in this section are as follows:

1.  $\tau_*$  and  $\alpha_*$ : Observed gas fraction - luminosity relation at  $z = 0$ ;
2.  $V_{\text{hot}}$ : faint end of luminosity function and sizes of low-luminosity spirals;
3.  $\alpha_{\text{hot}}$ : faint end of luminosity function and Tully-Fisher relation, and
4. IMF: observations of solar neighbourhood suggests using a Kennicutt IMF, this is used for stars formed quiescently in discs. For star formation in bursts a top-heavy IMF is used, this is explained in section 2.4.

The parameter values for the model are listed in table 2.3 in section 2.4

The description of the GALFORM model so far allows us to follow the different processes occurring in halos to form stars in galaxies. GALFORM models the spectrophotometric properties of these stars to convert the information into observable properties, such as the ionizing luminosity of galaxies that we require. The effects of dust and ionized gas are also treated by the model. Stellar population models of Bruzual A. and Charlot (1993) are used to assign luminosities to galaxies. The spectral energy distribution provided by the model is given as a function of three variables, the time elapsed since the stars were formed, the metallicity of the stars and the distribution of the stellar masses (set by the stellar initial mass function). The ionizing luminosity is given by the luminosity of Lyman continuum photons.

### 2.3.1 Dark Matter Halo Merger Trees

The dark matter halo merger tree describes the evolution of halos as they merge and grow hierarchically, and is important for GALFORM as galaxies are assumed to form inside dark matter halos. There are two ways of generating these merger trees, the first method is to use the Monte-Carlo algorithm implemented in GALFORM, and the second is to extract the merger trees from N-Body simulation.

#### Using Monte-Carlo Merger Trees

GALFORM uses a Monte-Carlo algorithm to generate merger trees describing the formation paths of randomly selected dark matter halos. A binary merger tree for dark matter halos is created by splitting a halo into two progenitors at each branch in the tree, where the mass ratio of the two progenitors can take any value. The algorithm for generating the merger trees is based on the following equation from Lacey and Cole (1993) that gives the fraction of mass,  $f_{12}(M_1, M_2)dM_1$ , in halos of mass  $M_2$ , at time  $t_2$ , which at an earlier time,  $t_1$ , was in haloes of mass in the range  $M_1$  to  $M_1 + dM_1$ :

$$f_{12}(M_1, M_2)dM_1 = \frac{1}{\sqrt{2\pi}} \frac{(\delta_{c1} - \delta_{c2})}{(\sigma_1^2 - \sigma_2^2)^{3/2}} \times \exp \left[ -\frac{(\delta_{c1} - \delta_{c2})^2}{2(\sigma_1^2 - \sigma_2^2)} \right] \frac{d\sigma_1^2}{dM_1} dM_1. \quad (2.15)$$

$\delta_{c1}$  and  $\delta_{c2}$  are the critical thresholds on the linear overdensity for collapse at  $t_1$  and  $t_2$  respectively. Starting from the final halo in the merger tree and working back in time,

eq.(2.15) is used to build the halo merger tree by calculating the average number of progenitors,  $\frac{dN}{dM_1}$  as a function of  $M_1$ , the details of which are given in section 3.1 of Cole et al. (2000). The procedure generates a binary merger tree with very high time resolution, the binary merger tree is used to generate an equivalent merger tree at lower temporal resolution on a grid of time steps. The new merger tree is no longer binary, as more than one merger may exist at each time step.

### Using N-Body Merger Trees

From N-body simulations, the distribution of dark matter in the simulation box at various snapshot output times is known, but to create merger trees that can be utilized by GALFORM, the dark matter halos need to be identified in the simulation. The method used is a friends-of-friends (FOF) percolation algorithm. In this method, two particles within a given distance of one another, parametrized by the linking length,  $b$ , are linked together, these particles are considered "friends". If one of these particles links with a third particle, then all three particles are put into the same group as it is a "friend of a friend" to the original particle. Using this algorithm, particles that are close together are grouped as FOF halos, so massive halos will form in high density regions as one might expect. After the FOF halos are identified in one snapshot, the same particles are identified in preceding snapshots to find the progenitors of the halos in order to build a merger trees. Fig 2.3 shows the halo mass function of FOF halos at two different redshifts, from L-GADGET2 simulations that I ran (see section 2.4). The halo mass function of halos generated using the Monte-Carlo method (black lines) is also plotted for comparison.

Both methods described have their advantages and disadvantages, Monte-Carlo merger trees have a very high time resolution, but do not provide any spatial information about the halos. Merger trees extracted from N-Body merger trees do provide the spatial information, but the mass resolution is typically much lower because N-Body simulations are computationally expensive. For predicting global properties, Monte-Carlo merger trees are useful, however, for the purpose of this study, the positions of ionizing sources is important in understanding how reionization proceeds.

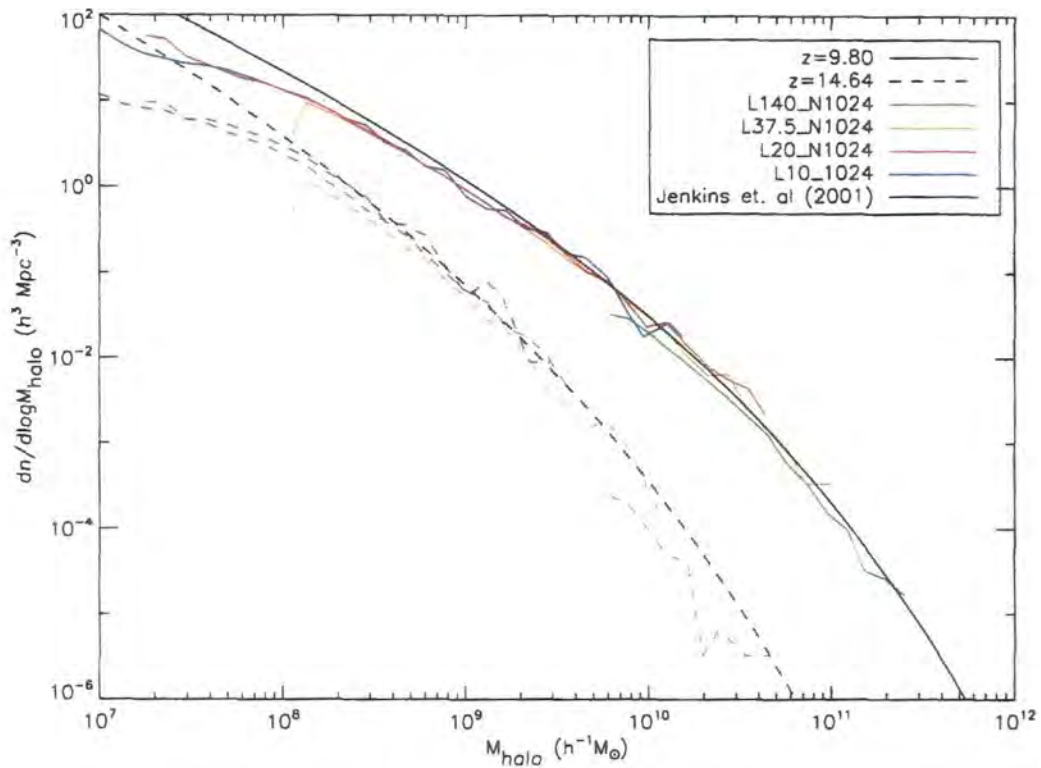


Figure 2.3: Halo mass function of FOF halos from a range of simulations (see section 2.4 for details). The black lines are the Jenkins et al. (2001) mass functions. The different colours represent different simulations as indicated by the legend. The solid lines and the dashed lines are the mass functions at  $z = 9.80$  and  $z = 14.64$ , respectively.

Name	Volume ( $(h^{-1}\text{Mpc})^3$ )	No. of Particles	Particle Mass ( $h^{-1}M_{\odot}$ )
L140_N1024	140	$1024^3$	$1.77 \times 10^8$
L140_N512	140	$512^3$	$1.42 \times 10^9$
L37.5_N1024	37.5	$1024^3$	$3.41 \times 10^6$
L37.5_N512	37.5	$512^3$	$2.73 \times 10^7$
L20_N1024	20	$1024^3$	$5.17 \times 10^5$
L10_N1024	10	$1024^3$	$6.46 \times 10^4$
L10_N512	10	$512^3$	$5.17 \times 10^5$

Table 2.1: List of simulations, all simulations listed are dark matter only, ran using the GADGET-2 code.

## 2.4 Running the simulations

One of the difficulties in simulating the 21-cm signal at high redshifts is that a large dynamic range needs to be considered. According to the paradigm of hierarchical structure formation, one would expect the early universe to be dominated by small, dwarf-size galaxies. However, strong clustering of sources at high redshifts would mean these small ionized regions overlap quickly and would form large ionized regions containing multiple sources, with sizes on the scale of tens of Mpc. Cosmological simulations need to be large enough to contain these regions while maintaining enough resolution to resolve the small sources from which the ionizing radiation originates. For this reason, a range of simulations with different volumes and particle masses were run to cover a large range of masses. Here, I summarise the details of simulations I generated using the tools described in this chapter, for the purpose of this study. The list of simulations is given in table 2.1, all the simulations listed are dark matter only. For setting up the initial conditions using N-GENiC, the box size, standard cosmological parameters, starting redshift, and power spectrum must be specified. For each simulation, the corresponding box size was used (see table 2.1). The cosmological parameters listed in table 2.2, a starting redshift of 127 and the power spectrum used to generate initial conditions for the Millennium simulation were used to generate the initial conditions. The starting redshift was chosen to match the starting redshift of the GADGET-2 simulations. The seven dark matter only N-Body simulations listed in table 2.1 were run using these initial con-

Parameter	Value
$\Omega_M$	0.25
$\Omega_\Lambda$	0.75
$\Omega_B$	0.045
$h$	0.73
$\sigma_8$	0.9

Table 2.2: Cosmological parameters used, these match the cosmological parameters used in the Millennium simulation.

ditions, as well as further parameters specific to GADGET-2. The same cosmological parameters listed in table 2.2 were used again, with the exception that  $\Omega_B$  was set to zero, this is because the simulations are dark matter only, there are no baryons during the run even though the transfer function does contain baryons. The simulations were run from  $z = 127$  to  $z = 5$ . A high starting redshift was chosen to ensure the simulations began while still in the linear regime. Since the interest of this study is the epoch of reionization, there is no benefit in running the simulations to  $z = 0$ , especially since the simulations run much slower at low redshifts. The full particle data was stored at one hundred output times. The output times were chosen to be linear in the logarithm of the expansion factor between  $z = 127$  to  $z = 5$ . The softening factor of one-twentieth of the mean particle separation was used. For the simulations containing  $512^3$  particles, the simulations were run on sixteen 2.2GHz cores. The simulations took between approximately thirteen (L140\_N512) to twenty seven (L10\_N512) hours to complete, depending on the mass resolution. For the simulations containing  $1024^3$  particles, one hundred and twenty eight 2.2GHz cores were used. These simulations took between approximately seventy five (L140\_N1024) to ninety four (L10\_N1024) hours to run to completion.

The GALFORM model used is based on the Baugh et al. (2005) model, with the cosmological parameters of table 2.2. Some of the major parameters were described in section 2.3, the values of which are given in table 2.3. Note that these are the “default” reference values,  $z_{\text{cut}}$  was modified in selected GALFORM runs to investigate its effect. For the GALFORM runs using Monte-Carlo merger trees, some additional parameters must also be specified. These are given in table 2.4.

Parameter	Value
Disc IMF	Kennicutt
Burst IMF	Top-heavy
$V_{\text{hot}}$	$300\text{kms}^{-1}$
$\alpha_{\text{hot}}$	2
$z_{\text{cut}}$	6
$V_{\text{cut}}$	$60\text{kms}^{-1}$

Table 2.3: GALFORM reference parameters used, GALFORM was also run with a modified value of  $z_{\text{cut}}$ .

Parameter	Value
$M_{\text{low}}$	$10^7 h^{-1} M_{\odot}$
$M_{\text{res}}$	$10^7 h^{-1} M_{\odot}$
$M_{\text{fac}}$	$\sqrt{2}$
$n_{\text{bin}}$	35
$n_{\text{halo,min}}$	25
$n_{\text{halo,max}}$	500

Table 2.4: GALFORM parameters used for Monte-Carlo merger tree specific runs.

$M_{\text{low}}$  is the mass of the smallest halo mass bin, while the mass resolution,  $M_{\text{res}}$ , is the minimum halo mass in merger trees. The values for these parameters were chosen to roughly match the mass resolution of the L20\_N1024 simulation. The halo mass bins are spaced geometrically with the factor  $M_{\text{fac}}$ . That is to say, the position of the  $n^{\text{th}}$  bin is at  $M_{\text{low}} \times (M_{\text{fac}})^n$ .  $n_{\text{bin}}$  is the total number of halo mass bins used. For the values of  $M_{\text{low}}$  and  $M_{\text{fac}}$  chosen, 35 halo mass bins were used to cover the range of  $10^7 h^{-1} M_{\odot}$  to  $\sim 10^{12} h^{-1} M_{\odot}$  in halo mass. This range was chosen so comparisons could be made between the Monte-Carlo merger trees and N-body merger trees.  $n_{\text{halo,min}}$  and  $n_{\text{halo,max}}$  are two parameters controlling the minimum and maximum number of realisations used in each bin. The values for these two parameters were chosen after trial and error at multiple redshifts to find the maximum number of realisations that may be used, while keeping the calculations sufficiently well converged.

The top-heavy IMF used for stars formed in bursts was introduced to the GALFORM model in Baugh et al. (2005). Previously, the Kennicutt IMF was used for both stars formed quiescently in discs and in starbursts, based on observations of the solar neighbourhood. The adoption of a top-heavy IMF in starbursts is motivated for two reasons. Firstly, a larger fraction of high mass stars in a top-heavy IMF increases the total energy radiated in the UV per unit mass of stars formed. This increase means there is more energy available to heat the dust. Secondly, more metals are formed from Type II supernovae, leading to more dust to absorb the extra UV radiation. These two factors relating to dust help boost the luminosity of high redshift galaxies in the sub-millimetre wavelength range, one of the observations Baugh et al. (2005) tried to model and explain.

# Chapter 3

## *Simulating the Epoch of Reionization*

### 3.1 Introduction

In the previous chapter (chapter 2), the various tools and methods used to simulate the universe were described. Before moving on to simulating the 21-cm signal, it will be useful to first examine these simulations.

### 3.2 Ionizing Emissivities as a Function of Halo Mass

An interesting thing to look at is where the ionizing photons are produced. One can expect a massive halo to produce many ionizing photons, and a low mass halo to produce much less. However, since the halo mass function shows that low mass halos are much more abundant than massive ones, it is not immediately obvious where the bulk of the ionizing photons originate from. This information is important when using N-Body simulations. Since the simulations are limited by resolution and box size, it is difficult to cover the full dynamic range in halo mass to capture all the ionizing photons. Having this information allows us to choose a box size that covers a range where most of the ionizing photons are produced. Fig 3.1 shows the ionizing emissivity in logarithmic mass bins for all the N-Body simulations using  $1024^3$  particles. Since the same number of particles are used, the larger volumes will have lower mass resolutions. The simulations agree reasonably well where they overlap. The Monte-Carlo merger trees (in black) show that ionizing photons are produced from a range of halo masses from  $\sim 5 \times 10^7 h^{-1} M_{\odot}$  to upwards of  $10^{12} h^{-1} M_{\odot}$  at  $z = 9.80$ . However, with the largest simulation, L140\_N1024, no ionizing photons are produced in halos of mass below  $\sim 3 \times 10^9 h^{-1} M_{\odot}$ . The L20\_N1024 and L10\_N1024 simulations both resolve the smallest halos producing ionizing photons

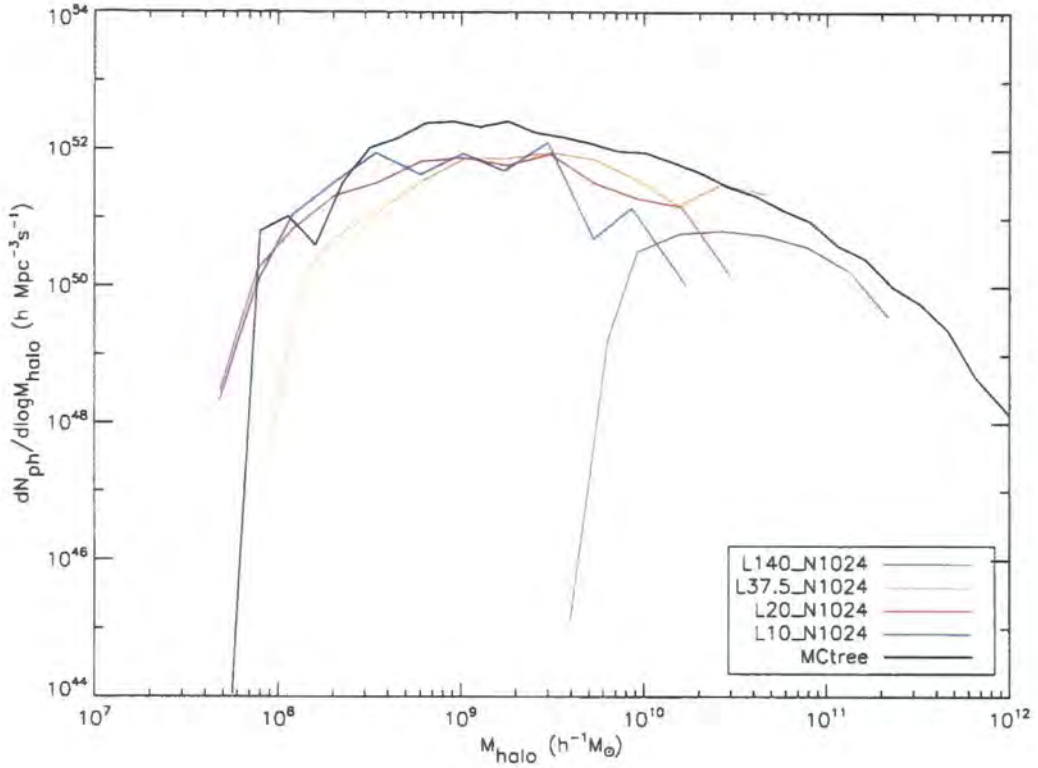


Figure 3.1: Total ionizing emissivity as a function of logarithmic mass bins at  $z = 9.80$ . The black line is from using Monte-Carlo merger trees for comparison. The other different colour lines represent different N-Body simulations: L140\_N1024, L37.5\_N1024, L20\_N1024 and L10\_N1024 are represented by green, orange, red and blue lines respectively. The larger volumes have a high particle mass and do not resolve the low mass halos.

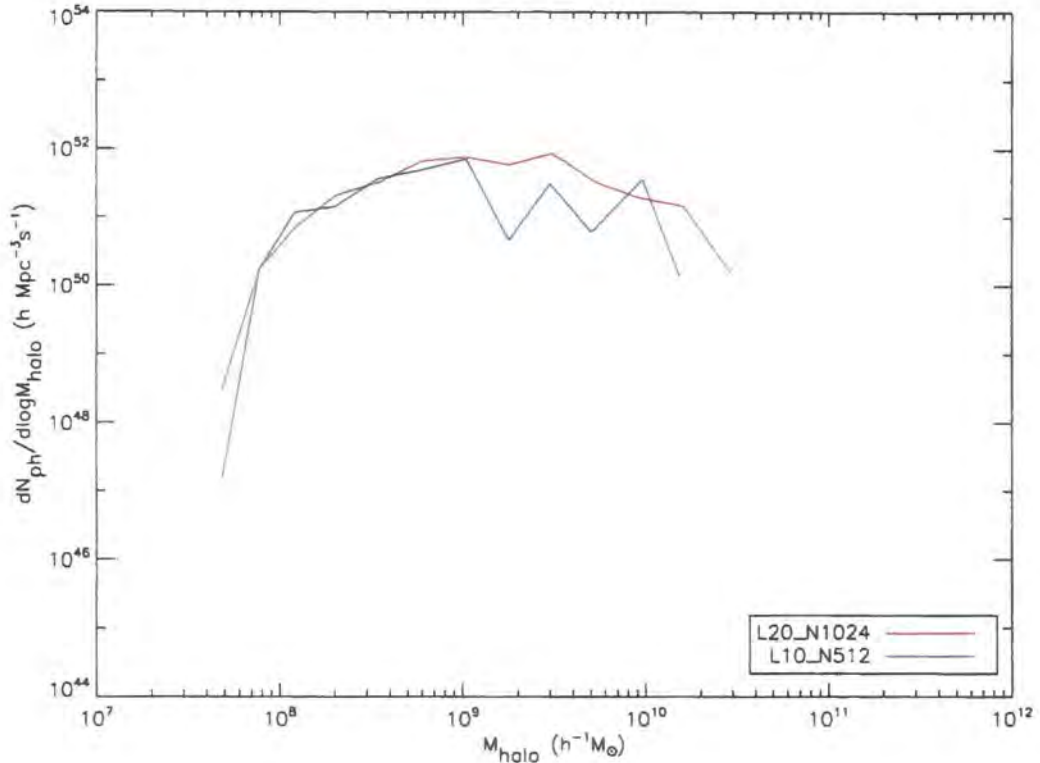


Figure 3.2: Total ionizing emissivity as a function of logarithmic mass bins at  $z = 9.80$ . The red and blue lines represent the L20.1024 and the L10.N512 simulations respectively. Both simulations have the same particle mass, at the same mass resolution the larger simulation volume covers a broader dynamic range in mass.

as indicated by the Monte-Carlo merger trees. In fact, we can be confident that the drop off in ionizing photon production is physical and not due to numerical effects, since increasing the mass resolution by eight times from L20.N1024 to L10.N1024 does not yield any more photons from halos below  $\sim 5 \times 10^7 h^{-1} M_{\odot}$ . As discussed, a larger simulation volume allows halos of higher masses to form. To demonstrate this, Fig. 3.2 shows two simulations with identical particle masses but different box sizes. Since both simulations have identical particle masses, both resolve the same low mass halos, the difference is at the high mass end. At  $z = 9.80$ , the L20.N1024 simulation (red solid line) extends approximately to  $3 \times 10^{10} h^{-1} M_{\odot}$  while the L10.N1024 simulation (blue solid line) reaches approximately  $1.5 \times 10^{10} h^{-1} M_{\odot}$ . Although this seems like a small mass range, the ionizing emissivity of L10.N1024 actually begins to drop much more rapidly at  $\sim 10^9 h^{-1} M_{\odot}$ ,

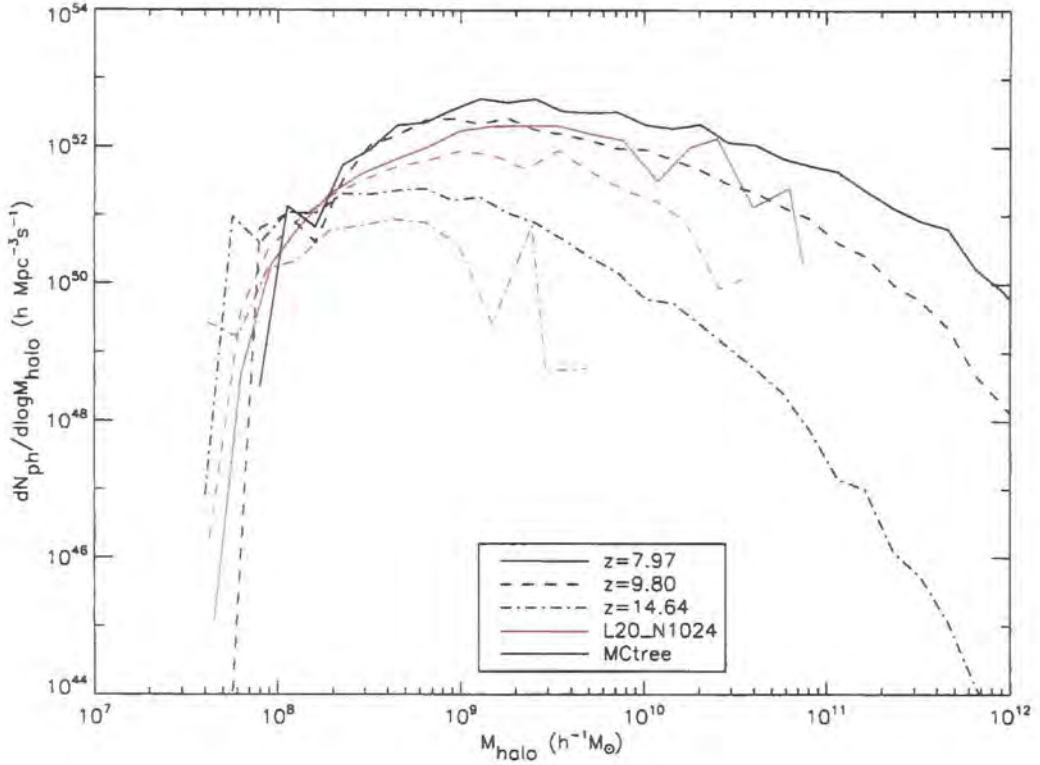


Figure 3.3: Evolution of the total ionizing emissivity in logarithmic mass bins in redshift. The red line is from the L20\_N1024 simulation while the black line is using Monte-Carlo merger trees. The solid, dashed, and dot-dashed lines represent redshifts of 7.97, 9.80 and 14.64 respectively. The total ionizing emissivity increases as redshift decreases since an increasing number of galaxies are formed.

suggesting that above  $10^9 h^{-1} M_{\odot}$ , the L10\_N1024 simulation is insufficient and a larger volume is required. In figure 3.3, the ionizing emissivity as a function of halo mass is shown for the L20\_N1024 simulation and Monte-Carlo merger trees at various redshifts. The total emissivity (the area under the curves) increases with decreasing redshift as galaxies form. The contribution from high mass halos also increases as redshift decreases since an increasing number of large galaxies are formed in these halos. The large difference between N-Body simulations and Monte-Carlo merger trees at high masses is due to the limits of simulation volumes.

One of the aims of looking at this data is to determine the dynamic range in masses required in simulations to capture the bulk of the ionizing photons generated. Looking

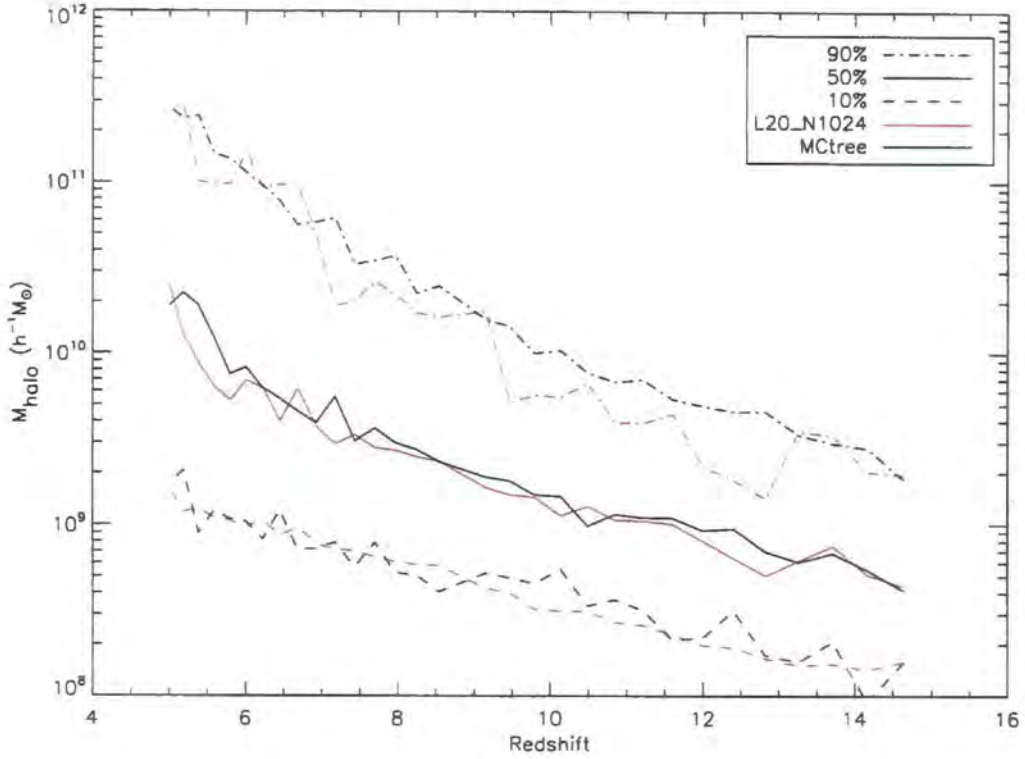


Figure 3.4: Fraction of ionizing emissivity produced in halos below a given mass between  $z = 5$  to  $z = 15$ . The solid lines indicate the halo mass at which 50% of the total ionizing emissivity in a given simulation is generated in halos at that mass or below, at a given redshift. The dashed lines and the dot-dashed lines represent the same quantity but at 10% and 90% respectively. The red lines are from the L20\_N1024 simulation while the black lines are from using Monte-Carlo merger trees. To be able to capture the bulk of the ionizing photons, one should aim to resolve at least the mass range between the 10% line and the 90% line. Note that this plot shows the fraction of the total ionizing emissivity in each simulation, so for example, the actual number of ionizing photons produced at 50% will vary between simulations, as shown in Fig. 3.1.

at Fig. 3.1, The curves appear to be quite flat at around  $10^9 h^{-1} M_{\odot}$ . This shows that a broad range of masses contribute significantly to the total ionizing emissivity. Note that even though the curves are flat around the peak, the figures have a logarithmic scale, and the ionizing emissivity does fall off at high masses. There is about 2 orders of magnitude difference between the ionizing emissivity at  $10^9 h^{-1} M_{\odot}$  and at  $10^{11} h^{-1} M_{\odot}$ . Instead of trying to identify the peak of the curve, we locate the halo mass bin at which fifty percent of the ionizing emissivity is contained below that mass for a range of redshifts, this is shown in Fig. 3.4. The halo mass for ten percent and ninety percent of the ionizing emissivity is also indicated on the figure. To be able to capture the bulk of the ionizing emissivity, one should aim to resolve at least the mass range indicated between the ten percent and ninety percent lines. At low redshifts, the ninety percent line increases rapidly (note the logarithmic scale), the fifty percent line also increases but less rapidly, while the ten percent line remains relatively flat. This shows that at low redshifts, a larger fraction of ionizing photons are generated in massive halos.

To investigate one of the feedback mechanisms in GALFORM, the  $z_{\text{cut}}$  parameter was modified. This changes the redshift at which gas cooling in low mass halos is suppressed due to reionization. Fig. 3.5 to Fig. 3.7 illustrate the effect of setting  $z_{\text{cut}} = 15$  compared with the default  $z_{\text{cut}} = 6$  at various redshifts.  $z_{\text{cut}} = 6$  corresponds to no suppression at the redshifts investigated. In Fig. 3.5, there is virtually no difference between the  $z_{\text{cut}} = 15$  and the  $z_{\text{cut}} = 6$  model. This is expected because suppression in the  $z_{\text{cut}} = 15$  has only just begun. As we move to lower redshifts (Fig. 3.6 and Fig. 3.7), the effect of the suppression can be clearly seen. Below masses corresponding to  $V_{\text{cut}}$  (indicated by the vertical dashed line), the ionizing emissivity of galaxies in the  $z_{\text{cut}} = 15$  model is many orders of magnitude below those in the default  $z_{\text{cut}} = 6$  model. The suppression is seen to have an effect on halos more massive than the mass corresponding to  $V_{\text{cut}}$ . This may be due to low mass halos that were suppressed at earlier redshifts, but have since merged into more massive halos.

One way to estimate the ionized fraction of the simulation is to consider the number of ionizing photons emitted per hydrogen atom. This is shown in Fig. 3.8. The simulations with low mass resolutions do not resolve low mass halos and it is clearly shown here that this is a significant effect at low redshifts. All the simulations begin to converge at low redshifts except for the L140.N512 simulation (dashed green). This

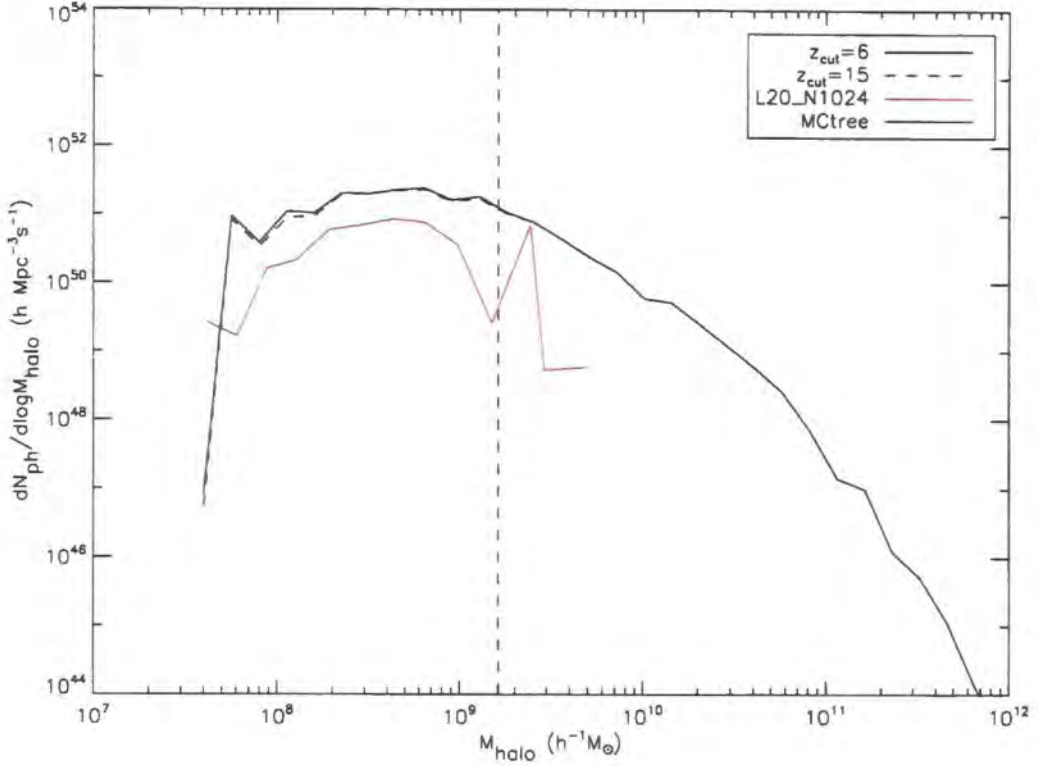


Figure 3.5: Effect of setting  $z_{\text{cut}} = 15$  in the GALFORM model on the ionizing emissivity at  $z = 14.64$ . The red line is from the L20\_N1024 simulation while the black line is using Monte-Carlo merger trees. The solid line represents the model with  $z_{\text{cut}} = 6$  while the dashed lines represents the model with  $z_{\text{cut}} = 15$ . The vertical dashed line indicates the halo mass corresponding to  $V_{\text{cut}} = 60\text{kms}^{-1}$ , galaxy formation below this mass is suppressed.

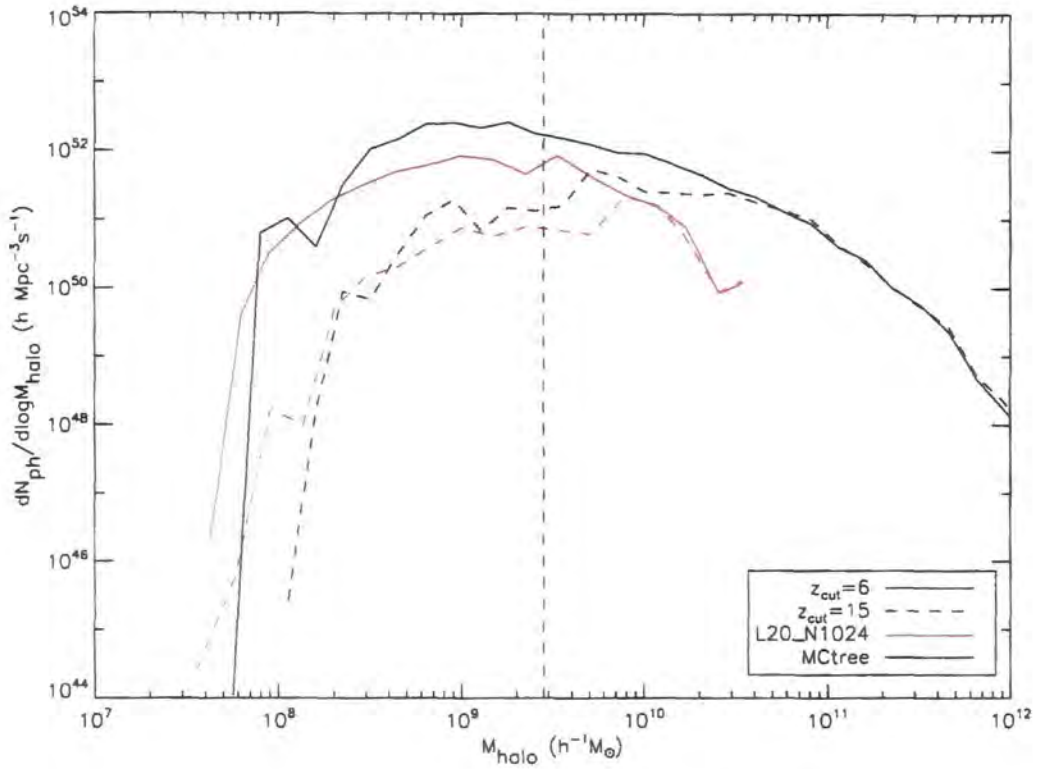


Figure 3.6: Effect of setting  $z_{\text{cut}} = 15$  in the GALFORM model on the ionizing emissivity at  $z = 9.80$ . The red line is from the L20\_N1024 simulation while the black line is using Monte-Carlo merger trees. The solid line represents the model with  $z_{\text{cut}} = 6$  while the dashed lines represents the model with  $z_{\text{cut}} = 15$ . The vertical dashed line indicates the halo mass corresponding to  $V_{\text{cut}} = 60 \text{ km s}^{-1}$ , galaxy formation below this mass is suppressed.

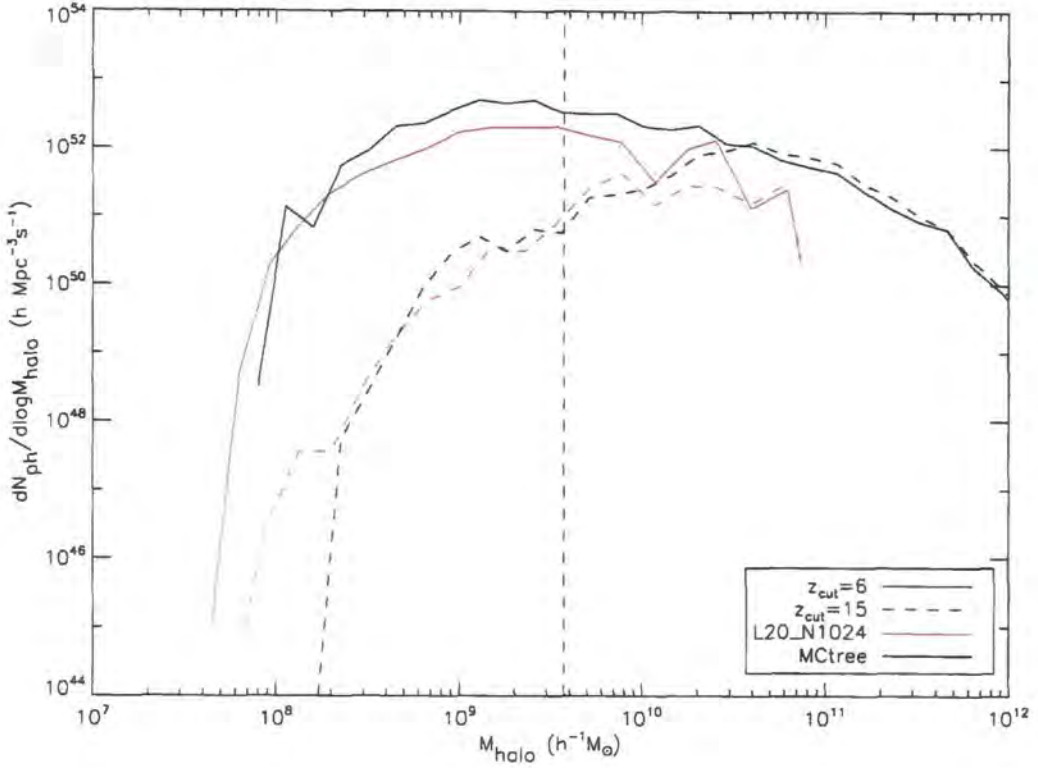


Figure 3.7: Effect of setting  $z_{\text{cut}} = 15$  in the GALFORM model on the ionizing emissivity at  $z = 7.97$ . The red line is from the L20\_N1024 simulation while the black line is using Monte-Carlo merger trees. The solid line represents the model with  $z_{\text{cut}} = 6$  while the dashed lines represents the model with  $z_{\text{cut}} = 15$ . The vertical dashed line indicates the halo mass corresponding to  $V_{\text{cut}} = 60\text{kms}^{-1}$ , galaxy formation below this mass is suppressed.

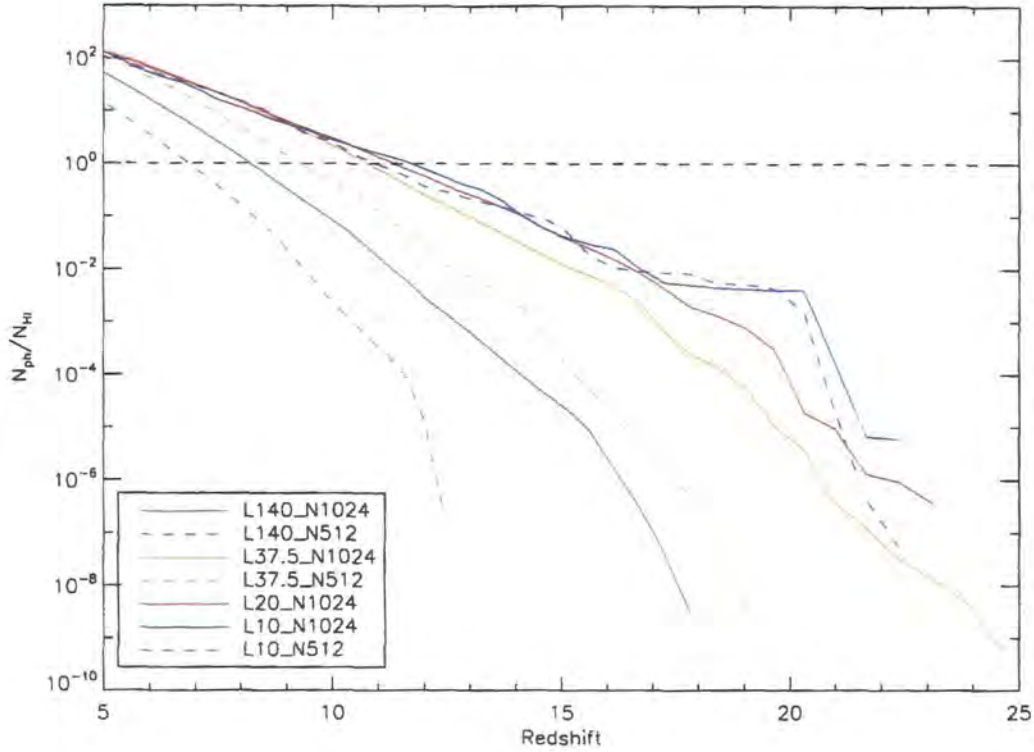


Figure 3.8: Number of ionizing photons per neutral hydrogen atom as a function of redshift for the different simulation boxes. Horizontal dashed line shows where  $\frac{N_{\text{ph}}}{N_{\text{HI}}} = 1$ .

is the simulation with the worst mass resolution. Assuming that each ionizing photon ionizes one neutral hydrogen atom, each simulation can be considered fully ionized at approximately the redshift where there is one ionizing photon per hydrogen atom if re-combinations are ignored. Fig. 3.9 again shows the number of ionizing photons per hydrogen atom, but now with  $z_{\text{cut}} = 15$ . As expected, the two figures are identical above  $z = 15$ . Below  $z = 15$ , the suppression affects mostly the smaller simulation volumes, where the contribution of ionizing photons from low mass halos are significant. Since the large simulation box (green line) does not resolve much of the smaller halos to begin with, suppression has minimal effect on it.

Table 3.1 lists the redshifts at which  $\frac{N_{\text{ph}}}{N_{\text{HI}}} = 1$ , extracted from Fig. 3.8 and Fig. 3.9 for the various simulations. This can be used as a reference for an approximation of the redshift of reionization. Values lie between 6.88 and 11.78, depending on the simulation used. This is done for both the  $z_{\text{cut}} = 6$  and  $z_{\text{cut}} = 15$  GALFORM models. As can be seen,

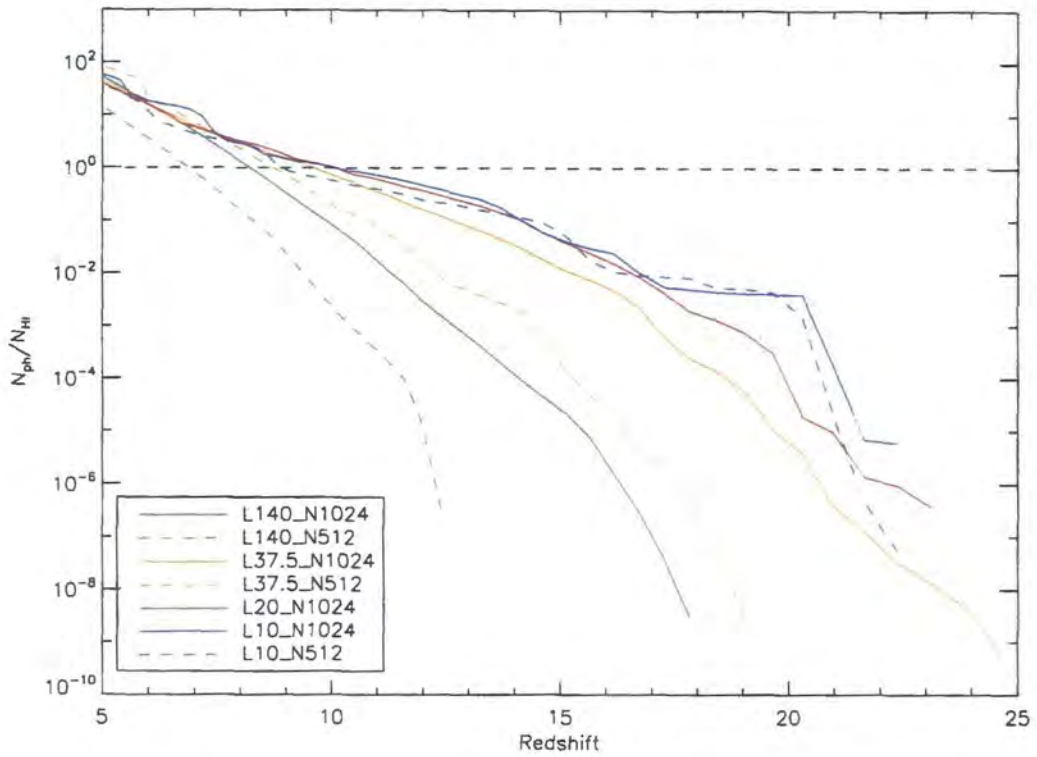


Figure 3.9: Number of ionizing photons per hydrogen atom as a function of redshift for the different simulation boxes, with  $z_{\text{cut}} = 15$ . Horizontal dashed line shows where  $\frac{N_{\text{ph}}}{N_{\text{HI}}} = 1$ .

Simulation	$z_{\text{cut}} = 6$	$z_{\text{cut}} = 15$
L140_N1024	8.24	8.24
L140_N512	6.88	6.88
L37.5_N1024	10.81	9.66
L37.5_N512	9.36	8.77
L20_N1024	11.41	10.13
L10_N1024	11.78	10.13
L10_N512	11.00	8.91

Table 3.1: Redshifts at which  $\frac{N_{\text{ph}}}{N_{\text{HI}}} = 1$  in N-Body simulations.

increasing  $z_{\text{cut}}$  to 15 has no effect on the largest simulation boxes, this is because these simulations do not resolve the smallest halos that are suppressed as discussed. For the other simulations, the suppression of gas cooling by photoionization in low mass halos does show an effect and the redshift of reionization happens at later times if suppression begins at an earlier redshift.

# Chapter 4

## *Simulating the 21-cm Signal*

### 4.1 Introduction

In chapter 2, I described the tools and techniques used to simulate the distribution of mass in the Universe and predict the properties of galaxies that would form. With all the information needed, one can proceed to simulate 21-cm signal expected from the neutral hydrogen. In this chapter, I will first review the current status of 21-cm signal simulations, then the methods I used will be described. Finally, the 21-cm maps and spectra created will be presented.

### 4.2 Current status of 21-cm Signal simulations

The number of attempts to simulate the 21-cm signal have increased since the various observatories described in section 1.4 were being planned and built.

There are a number of simulations investigating the epoch of reionization but to date, there have been only been a few cosmological simulations which study the 21-cm signal specifically. In section 2.4, the significance of the large range of halo masses required in 21-cm simulations was already stated. Most of the current simulations either use a small volume to achieve the resolution required to resolve dwarf galaxies, or choose a large simulation volume with a low resolution to capture the large ionized regions produced by more massive galaxies.

Ciardi and Madau (2003) investigated whether the 21-cm signal will be observable. The N-body code, GADGET (initial version of GADGET-2, described in 2.2.1) was used to obtain the distribution of dark matter in a  $20h^{-1}\text{Mpc}$  box. The galaxy population was then modelled using semi-analytical techniques and a Monte-Carlo radiative transfer

code, CRASH (Cosmological Radiative transfer scheme for Hydrodynamics, Ciardi et al. (2001)), was used to propagate ionizing photons into the intergalactic medium. These simulations were carried out and estimated that during the early stages of reionization, enough Ly $\alpha$  continuum photons are emitted to decouple the spin temperature of neutral hydrogen from the background CMB temperature, causing 21-cm to become visible in either emission or absorption.

Mellema et al. (2006) made predictions for a range of observational characteristics using N-Body and radiative transfer simulations from Iliev et al. (2006). The N-Body simulation was performed using the particle-mesh code PM-FAST. This simulation used  $1624^3$  particles on a  $3248^3$  mesh in a volume of  $(100h^{-1}\text{Mpc})^3$ . The radiative transfer was carried out using C<sup>2</sup>-Ray, with mesh resolutions of  $203^3$  and  $406^3$ . The 21-cm maps generated were smoothed by integrating over a bandwidth of 200kHz and convolved with a Gaussian beam of FWHM 3 arcmin. This is to mimic upcoming observations, such as those by LOFAR (see section 1.4), that will not have the spatial resolution that the simulations can achieve. They concluded that although small details are smoothed over, the main structures such as ionized bubbles are still visible and should be detectable. They also found that there was a gradual decrease in 21-cm signal rather than a sharp step function, suggesting an extended period during which neutral hydrogen was ionized. This was further investigated in Iliev et al. (2007) where the extended nature of reionization was attributed to low mass sources with a high efficiency of producing ionizing photons. The presence of these sources at early times causes reionization to begin earlier. However at late times, these sources become suppressed due to Jeans mass filtering and no longer contribute to reionization. The later stages are controlled by the higher mass halos.

In the Iliev et al. (2006) simulations described above, the resolution of the radiative transfer is much lower than the N-Body simulation. This is because full 3-D radiative transfer simulations are very computational intensive. To overcome this, Thomas et al. (2008) investigated using a 1-D radiative transfer code, BEARS (Bubble Expansion Around Radiative Sources), instead to propagate ionizing photons. They compare results with the full 3-D radiative code, CRASH. The nature of the BEARS approach creates perfectly spherical bubbles, but while this does not reproduce the complex details of the ionization fronts, they argue that after filtering images from both BEARS and

CRASH with the telescope's point spread function (such as LOFAR's), the images are indistinguishable. A comparison of statistical quantities such as the mean neutral fraction at different redshifts showed that the two methods are in excellent agreement at early redshifts ( $z > 8$ ) but do not agree well at low redshifts. They attribute this to two reasons. Firstly, the IGM in the BEARS simulation is assumed to be predominantly uniform while the Universe is much less homogeneous at low redshifts. Secondly, the spherical bubbles become much larger and overlap with multiple bubbles. The BEARS treatment of overlapping bubbles becomes less accurate with multiple overlaps.

A recent simulation from Santos et al. (2008) uses a large simulation volume of  $100h^{-1}\text{Mpc}$  with a high particle mass resolution of  $3.02 \times 10^6 h^{-1}M_{\odot}$ , with halos reliably resolved down to masses of  $\sim 10^8 h^{-1}M_{\odot}$ . Quantities such as the clustering of neutral gas fraction, ionization fraction and the 21-cm signal calculated from this simulation were compared with the analytical models. They found that analytical models gave a reasonably accurate description of the 21-cm power spectrum, making them useful for quickly exploring the parameters relevant to surveys without needing to run computationally intensive runs. Similar conclusions were reached by Zahn et al. (2007).

### 4.3 Generating 21-cm Maps and Power Spectra

To simulate the 21-cm signal, the distribution of neutral hydrogen has to be known. In the method described in this section, this is achieved in two main steps. Firstly, the distribution of hydrogen gas is inferred from the N-body simulations run using L-Gadget2. Secondly, ionized regions are "painted" around ionizing sources identified by GALFORM. The first step gives a picture of 21-cm signal in the universe without reionization, while the second step adds ionized regions, which removes 21-cm signal from those areas.

#### 4.3.1 Calculating the 21-cm Brightness Temperature

To calculate the 21-cm brightness temperature,  $\delta T_b$ , first consider the optical depth,  $\tau_{\nu}$  (Rybicki and Lightman, 1979),

$$\tau_{\nu}(s) = \int_{s_0}^s \alpha_{\nu}(s') ds'. \quad (4.1)$$

$\alpha_\nu$  is the absorption coefficient and under local thermodynamic equilibrium, is given by

$$\alpha_\nu = \frac{h_p \nu}{4\pi} n_1 B_{12} \left(1 - e^{-h_p \nu / k T_s}\right) \phi(\nu), \quad (4.2)$$

where  $h_p$  is Planck's constant,  $\nu$  is the frequency,  $n_1$  is the number density of the lower quantum states,  $B_{12}$  is the Einstein absorption coefficient,  $k$  is the Boltzmann constant and  $\phi(\nu)$  is the normalised line profile. Using the Einstein relations:

$$A_{21} = \frac{2h\nu^3 g_1}{c^2 g_2} B_{12}. \quad (4.3)$$

where  $g_1$  and  $g_2$  are the number of states in the upper and lower energy levels (see section 1.3.1), we obtain the following expression for the absorption coefficient:

$$\alpha_\nu = \frac{c^2}{8\pi\nu^2} \frac{g_2}{g_1} n_1 A_{21} \left(1 - e^{-h_p \nu / k T_s}\right) \phi(\nu). \quad (4.4)$$

For the 21-cm line,  $\frac{h_p \nu}{k} = 0.068\text{K}$ . This is much less than the CMB temperature, which is much less than the expected spin temperature (see section 1.3.2). The approximation  $\frac{h_p \nu}{k} \ll T_s$  can be made. Also, for the 21-cm transition,  $g_2 = 3$  and  $g_1 = 1$  (see section 1.3.1). This implies that a quarter of the atoms are in the lower quantum state. So we have  $n_1 = \frac{n_{\text{HI}}}{4}$ , where  $n_{\text{HI}}$  is the number density of neutral hydrogen at the given redshift. Inserting these values and making the approximation above we obtain

$$\alpha_\nu = \frac{3c^2}{32\pi\nu^2} n_{\text{HI}} A_{21} \frac{h_p \nu}{k T_s} \phi(\nu). \quad (4.5)$$

To calculate the optical depth, we need to consider the line profile and carry out the integration in eq. (4.1). Since the 21-cm line is extremely narrow, all of the optical depth is constrained to a specific redshift  $z$ .  $\phi(\nu)$  can be considered as a delta function over the line of sight variable  $s'$ .  $\phi(\nu)$  can be written as

$$\phi(\nu) = \delta[\nu_{21} - (1 + z')\nu] = \frac{(1 + z')}{\nu_{21}} \delta(z - z'), \quad (4.6)$$

where  $\nu$  is the observed frequency, and is related to the redshift,  $z$ , via

$$z = \frac{\nu_{21}}{\nu} - 1 \quad (4.7)$$

Combining equations (4.5) and (4.6) and performing the integration in eq. (4.1) over redshift to obtain

$$\tau_\nu = \int \frac{3c^2}{32\pi\nu_{21}^2} n_{\text{HI}} A_{21} \frac{h_p \nu_{21}}{k T_s} \frac{(1 + z')}{\nu_{21}} \delta(z - z') \frac{ds}{dz'} dz' \quad (4.8)$$

$$\tau_\nu = \frac{3c^2}{32\pi\nu_{21}^2} n_{\text{HI}} A_{21} \frac{h_p \nu_{21}}{k T_s} \frac{(1 + z)}{\nu_{21}} \frac{ds}{dz}. \quad (4.9)$$

The number density of neutral hydrogen is related to the mass density of neutral hydrogen simply by

$$n_{\text{HI}} = \langle n_{\text{H}} \rangle \frac{\rho_{\text{HI}}}{\langle \rho_{\text{H}} \rangle}. \quad (4.10)$$

Since the mean density is locked to the Hubble flow, it evolves as  $(1+z)^3$  and can be defined in terms of the present day value of the baryon density,  $\Omega_B$ , to obtain

$$\begin{aligned} \langle n_{\text{H}} \rangle &= \frac{\rho_B}{m_{\text{H}}} X (1+z)^3 \\ &= \frac{\Omega_B \rho_{\text{crit}}}{m_{\text{H}}} X (1+z)^3 \\ \langle n_{\text{H}} \rangle &= \frac{3H_0}{8\pi G} \frac{\Omega_B}{m_{\text{H}}} X (1+z)^3, \end{aligned} \quad (4.11)$$

where  $\rho_B$  is the physical baryon density,  $m_{\text{H}}$  is the mass of a hydrogen atom,  $X$  is the hydrogen abundance by mass.  $\rho_{\text{crit}}$  is the critical density and is given by  $\frac{3H_0^2}{8\pi G}$ , where  $H_0$  is the present day Hubble constant and  $G$  is the gravitational constant.

With the optical depth, we can now calculate the specific intensity at the source of the 21-cm emission. The specific intensity,  $I_\nu$ , is given in terms of the background CMB brightness,  $I_{\text{CMB}}$  and the emission brightness of the neutral hydrogen,  $I_{\text{HI}}$ :

$$I_\nu = I_{\text{CMB}} e^{-\tau_\nu} + I_{\text{HI}} (1 - e^{-\tau_\nu}) \quad (4.12)$$

The difference between the CMB background and neutral hydrogen intensity is then

$$\Delta I_\nu = I_\nu - I_{\text{CMB}} \quad (4.13)$$

$$\Delta I_\nu = (I_{\text{HI}} - I_{\text{CMB}}) (1 - e^{-\tau_\nu}) \approx (I_{\text{HI}} - I_{\text{CMB}}) \tau_\nu, \quad (4.14)$$

where the approximation can be made since the optical depths associated with the 21-cm emissions are small. The last step is to propagate the emission to a present day observer on Earth. The proper length per redshift interval,  $\frac{ds}{dz}$  is given by

$$\frac{ds}{dz} = \frac{c}{H_0(1+z)E(z)}, \quad (4.15)$$

where  $E(z) \equiv [\Omega_M(1+z)^3 + \Omega_k(1+z)^2 + \Omega_\Lambda]^{1/2}$  (Peebles, 1993, pp 310-321). Also, in proper coordinates, the brightness conservation law is given by (Peacock, 1999, eq. (3.88))

$$I_\nu(0) = \frac{I_\nu(z)}{(1+z)^3}. \quad (4.16)$$

Combining equations (4.9) through to (4.11) and (4.14) through to (4.16), then simplifying, we obtain

$$\Delta I_\nu = \frac{3c^3}{32\pi\nu_{21}^3} \left( \frac{3H_0^2 \Omega_B}{8\pi G m_H} X \right) \frac{A_{21}}{H_0 E(z)} \frac{h_p \nu_{21}}{k} \frac{(I_{\text{HI}} - I_{\text{CMB}})}{T_s} \frac{\rho_{\text{HI}}}{\langle \rho_{\text{H}} \rangle} \quad (4.17)$$

For radio wavelengths where the Rayleigh-Jeans law usually applies, the specific intensity is related to the brightness temperature,  $T_b$ , via (Rybicki and Lightman, 1979, eq. 1.60)

$$I_\nu = \frac{2\nu^2}{c^2} k T_b. \quad (4.18)$$

The specific intensities in eq. (4.17) can therefore be replaced by the brightness temperatures to obtain the differential brightness temperature,

$$\delta T_b = \frac{3c^3}{32\pi\nu_{21}^3} \left( \frac{3H_0^2 \Omega_B}{8\pi G m_H} X \right) \frac{A_{21}}{H_0 E(z)} \frac{h_p \nu_{21}}{k} \frac{(T_s - T_{\text{CMB}})}{T_s} (1+z)^2 \frac{\rho_{\text{HI}}}{\langle \rho_{\text{H}} \rangle}, \quad (4.19)$$

where the  $(1+z)^2$  factor relates the temperature on the left hand side, which is measured at the observer, and the temperature on the right hand side, which is in the frame of the neutral hydrogen. Substituting standard values for the constants ( $c$ ,  $\nu_{21}$ ,  $G$ ,  $m_H$ ,  $A_{21}$ ,  $h_p$ ,  $k$ ) and taking  $\Omega_B = 0.045$ ,  $X = 0.73$ , eq. (4.19) simplifies to

$$\delta T_b = (3.3\text{mK}) h^{-1} \frac{(1+z)^2}{E(z)} \frac{(T_s - T_{\text{CMB}})}{T_s} \frac{\rho_{\text{HI}}}{\langle \rho_{\text{H}} \rangle}. \quad (4.20)$$

Assuming that  $T_s \gg T_{\text{CMB}}$ , the 21-cm brightness temperature at a specific redshift can be computed using eq. (4.20) given a set cosmological density parameters ( $\Omega_M$ ,  $\Omega_k$ ,  $\Omega_\Lambda$ ) and the neutral hydrogen density inferred from the density field of the N-Body simulations. Eq. (4.20) uses the density of the hydrogen gas,  $\rho_{\text{HI}}$ , however, our N-Body simulations contain no gas particles. We assume that the gas distribution follows the dark matter from the simulations, so  $\delta_{\text{H}} = \delta_{\text{DM}}$ , where  $\delta = \frac{\rho}{\langle \rho \rangle} - 1$  is the over-density. Also, for a given ionized fraction,  $x_{\text{HII}}$ , the neutral hydrogen density is  $\rho_{\text{HI}} = (1 - x_{\text{HII}}) \times \rho_{\text{H}}$ , so the expression  $\frac{\rho_{\text{HI}}}{\langle \rho_{\text{H}} \rangle}$  in (4.20) is given by

$$\frac{\rho_{\text{HI}}}{\langle \rho_{\text{H}} \rangle} = (1 - x_{\text{HII}}) \times \frac{\rho_{\text{DM}}}{\langle \rho_{\text{DM}} \rangle}. \quad (4.21)$$

For simplicity, we take  $x_{\text{HII}} = 0$  in neutral regions and  $x_{\text{HII}} = 1$  in ionized regions.

### 4.3.2 Cosmological HII Regions

Using the method described in the previous section (4.3.1), a map of the 21-cm brightness temperature can be obtained. This map is calculated from a neutral hydrogen density

field and does not take into account reionization of hydrogen atoms. To obtain a more accurate picture of the sky, the next step is to determine the ionized regions where there should be no 21-cm emission. Given the distribution of matter (from GADGET2), and positions and luminosities of ionizing sources (from GALFORM), there are numerous ways of approaching the problem of determining the regions of ionized hydrogen. One of the methods would be to carry out radiative transfer calculations to simulate the propagation of ionizing photons, determining which hydrogen atoms have been successfully ionized. This technique is very computationally intensive but can give more realistic results such as in the ionization fronts. Indeed, as explored in section 4.2, this is a common technique.

The method presented in this thesis is relatively simple when compared with using a radiative transfer code, and a good first step in approaching the problem. In this approach, ionized regions are created using cosmological Strömngren spheres. Strömngren spheres are well known in the area of stellar astrophysics, and was first derived by Bengt Strömngren (Strömngren, 1939). The cosmological generalization is described in Shapiro and Giroux (1987), who write the co-moving Strömngren radius,  $r_s$  as

$$r_s(t) = \left[ \frac{3N_{\text{ph}}}{4\pi x_{\text{HII}}\alpha_2 c_l n_{H,i}^2} \right]^{1/3} a(t) = r_{s,i} a(t), \quad (4.22)$$

where  $N_{\text{ph}}$  is the ionizing luminosity,  $x_{\text{HII}}$  is the ionized fraction within the ionized region.  $\alpha_2$  is the recombination coefficient to levels  $n \geq 2$ ,  $c_l$  is the small scale gas clumping factor and  $n_{H,i}$  is the average intergalactic hydrogen atom number density when the source turns on. The scale factor  $a(t) = \frac{1+z_i}{1+z}$  where  $z_i$  is the redshift at which the source turns on. Eq. (4.22) is derived by balancing the ionization rates with the recombination rates, creating a sphere of ionized gas when the two are in equilibrium. For simplicity, we assume a smooth universe with  $c_l = 1$ , and that within the ionized regions, the gas is completely ionized ( $x_{\text{HII}} = 1$ ). Also, the average hydrogen atom number density of the whole simulation box was used for  $n_{H,i}$ . This does not take into account of local density variations around sources, since bright sources would be expected to form in over-dense regions, we would expect large spheres to be too large while small spheres in under-dense regions to be too small. This choice was made for ease of implementation. The ionizing luminosities given by GALFORM are at a given redshift, so the Strömngren radii are calculated directly at that redshift, i.e. the light travel time is not included in

our calculations. The co-moving Strömngren radius calculated for each snapshot is  $r_{s,i}$ , using the GALFORM ionizing luminosities for that snapshot. Using eq. (4.22) for each GALFORM ionizing source, the cells in the density grid that lie within a cosmological Strömngren sphere are simply labeled with an ionized fraction of 1, while regions outside the spheres are labeled with an ionized fraction of 0. A simple prescription was taken to correct for overlapping spheres,

1.  $r_{s,i}$  for all ionizing sources in the simulation is first calculated
2. Starting with the brightest source, any other sources lying within its ionized region would merge with it, and all these sources would then be considered as just one source at the position of the brightest source. The luminosity of this source is the sum of the luminosities of the individual sources before merging.
3. The same procedure is carried out for all the remaining sources in reverse order of brightness (Brightest first).
4. The final ionized regions are then determined by recalculating the Strömngren radii of the new, merged sources.

The above prescription is implemented using periodic boundary conditions. There will be significant errors if the volume of the overlapping region is large, or for example, if there are two or more bright sources lying close to one another, but lie just outside each others ionized region. In reality the ionized regions also would not grow radially in this case, but rather towards opposite edges of the bubbles. The photons from one source would stream through the sphere created by the other source, ionizing the neutral hydrogen at the edge of ionized region around the second source. For two sources, this would create an ionized region with a characteristic butterfly shape, instead of two spherical regions as is assumed here. The advantage of the method presented here is that it is easy to implement and can compensate partially for the lost ionizing photons in the overlapped regions.

Fig. 4.2 shows  $\delta T_b$  for a slice from the L20\_N1024 simulation at  $z = 14.64$ , when we assume the distribution of hydrogen gas follows the dark matter and that  $T_s$  is constant,  $\delta T_b$  also follows the matter distribution shown in Fig 4.1. After applying the prescription described in section 4.3.2 to obtain the ionized regions, the slice shown in Fig. 4.2 now

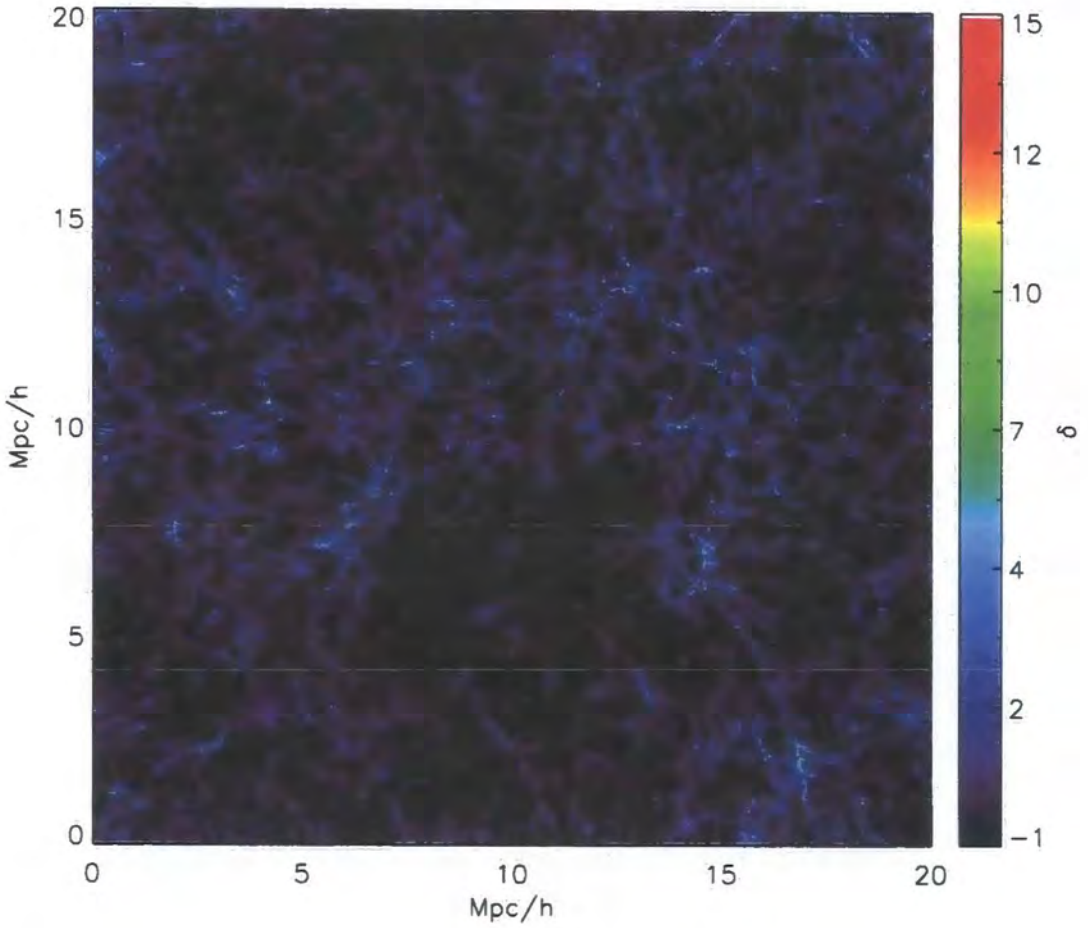


Figure 4.1: Over-density slice from the L20\_N1024 simulation at  $z = 14.64$ . The density field was computed using a cloud-in-cells assignment onto a  $512^3$  grid.

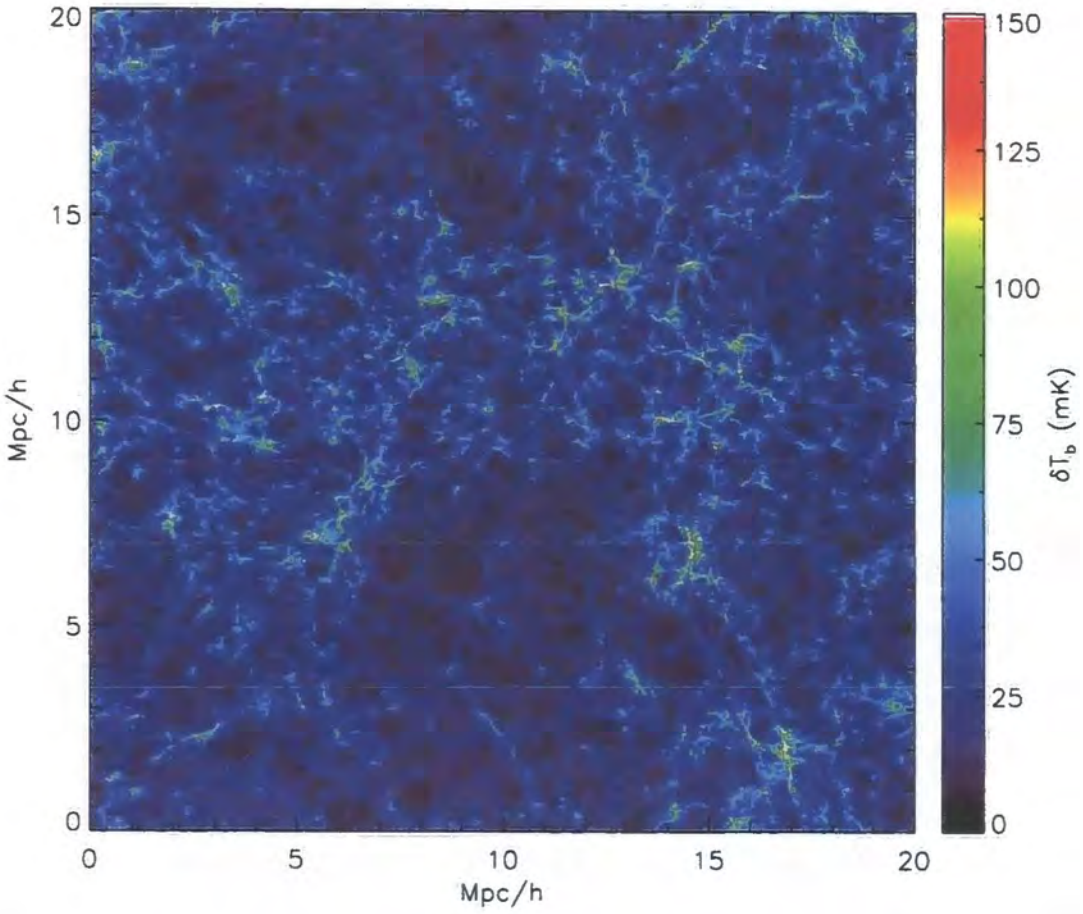


Figure 4.2:  $\delta T_b$  of a 2D slice from the L20\_N1024 simulation at  $z = 14.64$ . This is from the same slice as Fig. 4.1.  $\delta T_b$  follows the hydrogen distribution, which follows the density distribution shown in Fig. 4.1.

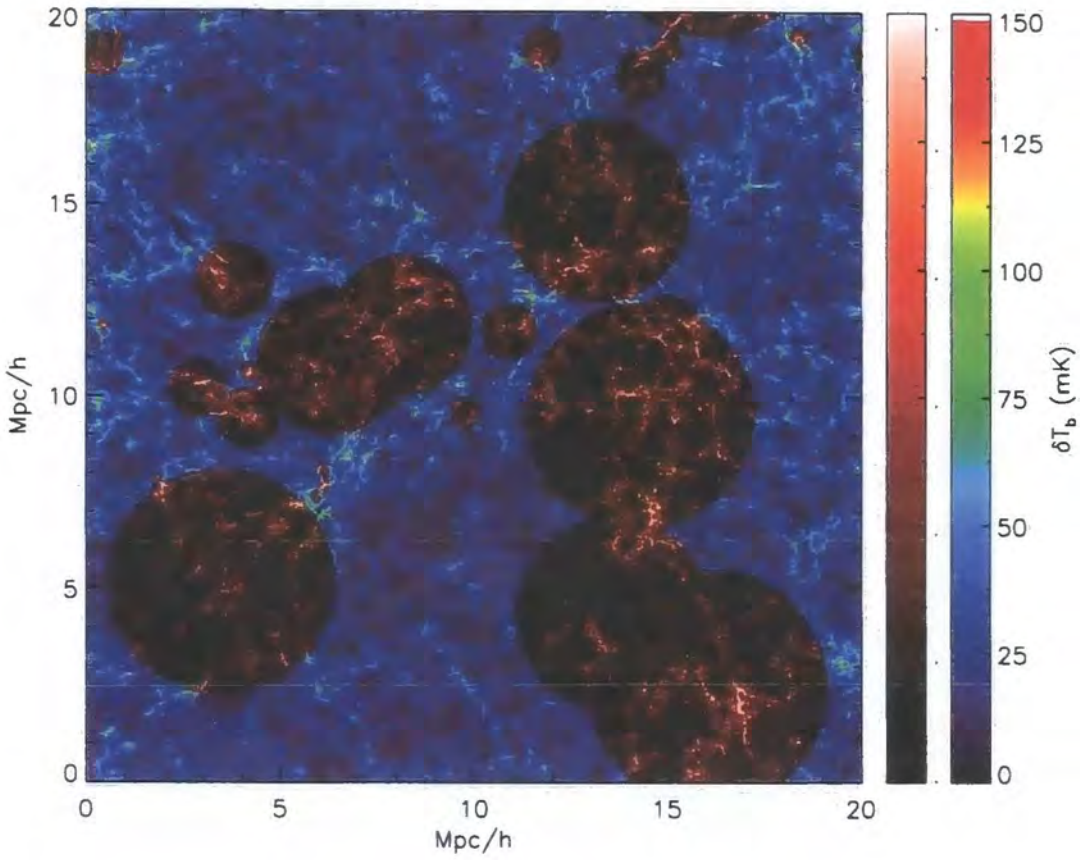


Figure 4.3:  $\delta T_b$  (rainbow) of a  $0.04h^{-1}\text{Mpc}$  thick slice from the L20\_N1024 simulation at  $z = 14.64$ , overlaid with the ionized regions (red). The red color scale represents  $\delta T_b$  if these ionized regions were neutral. This is the same slice as shown in Fig. 4.1 and Fig. 4.2.

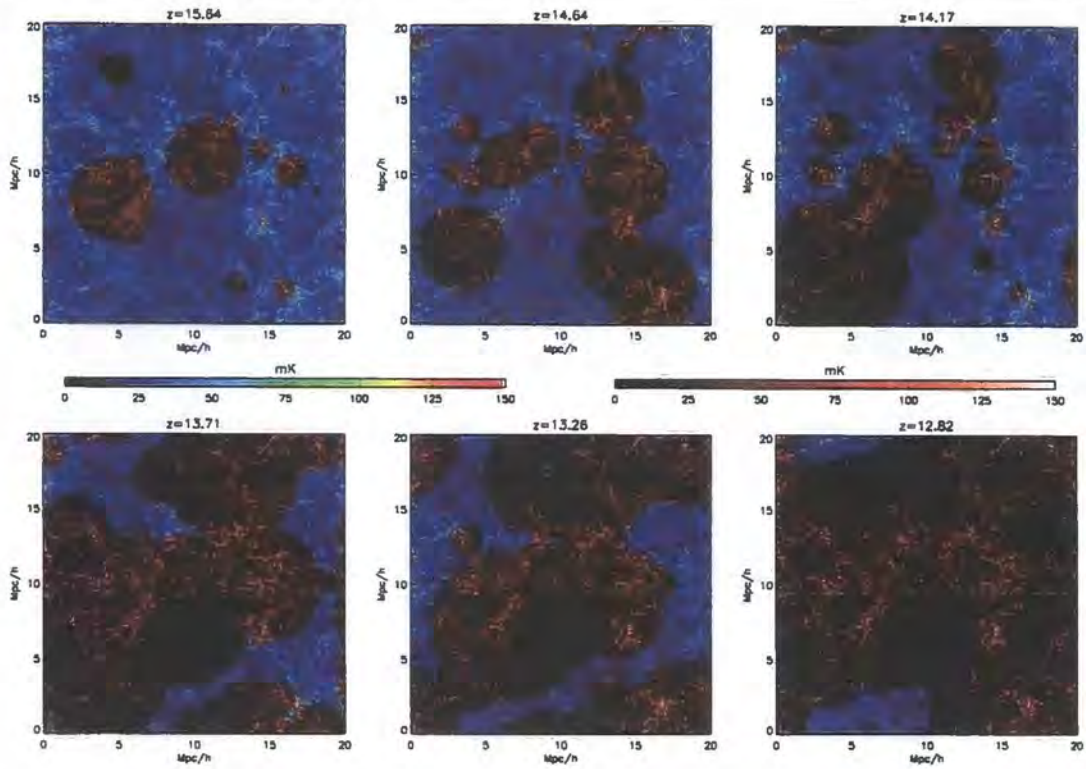


Figure 4.4: Same as Fig. 4.3 but at 6 different redshifts between  $z = 15.64$  and  $z = 12.82$ . Initially, there are only a few ionized bubbles. These bubbles grow as redshift decreases and at  $z = 12.82$ , nearly the whole box is ionized.

becomes Fig. 4.3. The ionized regions are represented by the red/white color scales, in these regions,  $\delta T_b = 0$  since there is no neutral hydrogen. Since high density regions are likely locations for halos to form, strong ionizing sources should also be expected in these regions, creating large ionized bubbles. When comparing Fig 4.2 with Fig 4.3, we can see that this effect erases much of the strongest 21-cm signal.

In Fig. 4.4, the same as Fig. 4.3 is shown but for a range of redshifts. As redshift decreases, the number of ionized bubbles as well as the size of these bubbles increases. The slice at  $z = 13.71$  show many large bubbles as well as significant overlap when compared with the slice at  $z = 14.17$ . Our prescription for correcting for overlapped regions would not be accurate for this case, but should work well during the early stages of reionization.

Table 4.1 presents the ionized fraction based on the total volume of Strömgren spheres,  $f_{\text{ion,ss}}$ , the ionized fraction based on the number of ionized cells in the cloud-in-cells grid,

Redshift	$f_{\text{ion,ss}}$	$f_{\text{ion,cells}}$	$f_{\text{overlap}}$
15.64	0.15	0.13	0.12
14.46	0.55	0.43	0.28
14.17	0.61	0.50	0.22
13.71	1.02	0.71	0.44
13.26	1.16	0.71	0.63
12.82	1.97	0.89	1.20

Table 4.1: The ionized fraction based on volume of Strömngren spheres, ionized fraction based on number of ionized cells in cloud-in-cells grid and the fraction of  $f_{\text{ion,cells}}$  that is overlapping at various redshifts for the L20\_N1024 simulation box. At  $z = 12.82$ , there is so much overlap that the total overlapped volume exceeds the total ionized volume based on the number of ionized cells.

$f_{\text{ion,cells}}$ , and the fraction of  $f_{\text{ion,cells}}$  that is overlapping,  $f_{\text{overlap}} = \frac{f_{\text{ion,ss}} - f_{\text{ion,cells}}}{f_{\text{ion,cells}}}$ .  $f_{\text{ion,ss}}$  can exceed unity since this is the total volume of Strömngren spheres without taking into account overlapping regions. These values are for the L20\_N1024 simulation. At higher redshifts, both the ionized fraction and  $f_{\text{overlap}}$  are low, this means the actual volume that is overlapped is only a small fraction of the volume of the box. As redshift decreases, both the ionized fraction and  $f_{\text{overlap}}$  are increasing in general. At  $z = 12.82$  there is so much overlap that the total overlapped volume exceeds the total ionized volume calculated from the number of ionized cells in the simulation box. However, it should be noted that the ionized fraction will never exceed 1 physically.  $f_{\text{ion,ss}}$  would be an overestimate at late stages of reionization, while  $f_{\text{ion,cells}}$  would be an underestimate. One can expect the true ionized fraction to lie somewhere between the two values. Physically, our prescription for correcting for overlapped regions may not be as bad as the large values of  $f_{\text{overlap}}$  suggests.

#### 4.4 21-cm Line of Sight Spectra

After post-processing of the density fields, we obtain  $\delta T_b$  as a function of 3-dimensional coordinates. To proceed to make 21-cm line-of-sight spectra and power spectra, we first convert one of the dimensions from distance into frequency. First, choose one axis of the

grid to be converted into frequency and consider a photon at one side of the simulation box at redshift  $z$ . The observed wavelength,  $\lambda$ , is given by

$$\lambda = \lambda_{21}(1+z) \left(1 + \frac{v}{c}\right), \quad (4.23)$$

where  $v$  is the Hubble velocity of a cell relative to the side of the box, given by eq. (1.1). The  $(1+z)$  term is to account for the cosmological redshift of the simulation output (see eq. 4.7), while the  $(1 + \frac{v}{c})$  term is due to the Hubble expansion. The Hubble velocity of a cell in terms of the comoving distance,  $x$ , from the side of the box is

$$v = H(z) \frac{x}{1+z}, \quad (4.24)$$

where  $H(z) = H_0 E(z)$ . Expressing eq. 4.23 in terms of the observed frequency,  $\nu$ , we obtain

$$\nu = \frac{\nu_{21}}{(1+z) \left(1 + \frac{v}{c}\right)}. \quad (4.25)$$

Calculating  $v$  for all cells using eq. (4.24) and using those values in eq. (4.25) gives the corresponding redshifted frequency of 21-cm photons in the cells. The peculiar velocity of each cell is neglected as it is insignificant when compared to the Hubble velocity.

The L20\_N1024 simulation is used to generate the spectra shown, as it was determined in chapter 3 that this was the simulation covering the most appropriate range in mass out of all the available simulations.

Fig. 4.5 shows an example of line-of-sight spectra at  $z = 14.64$  for the over-density,  $\delta$ , and  $\delta T_b$  with ionized regions in the simulation box. The  $\delta T_b$  spectrum has the same features as the overdensity spectrum. This is because the brightness temperature used is simply  $(1+\delta)$  multiplied by a constant factor, as shown in eq. (4.20). In the bottom spectra of Fig. 4.5, the frequencies at which there is no signal correspond to the ionized regions painted onto the temperature field. As can be seen, most of the signal is under 50mK, but there are some bright pixels in the simulations, such as the peak at approximately 89.95MHz, reaching over 250mK. All of the signal is in emission since the assumption that  $T_s \gg T_{\text{CMB}}$  is made. LOFAR is expected to achieve a sensitivity of  $\sim 35\text{mK}$  per resolution element after 100 nights of observation (Thomas et al., 2008). This means LOFAR will not be able to detect much of the signal, which is below  $\sim 35\text{mK}$ . However, most of the pronounced features in the LOS spectra lie above 35mK, and LOFAR will be able to detect these features.

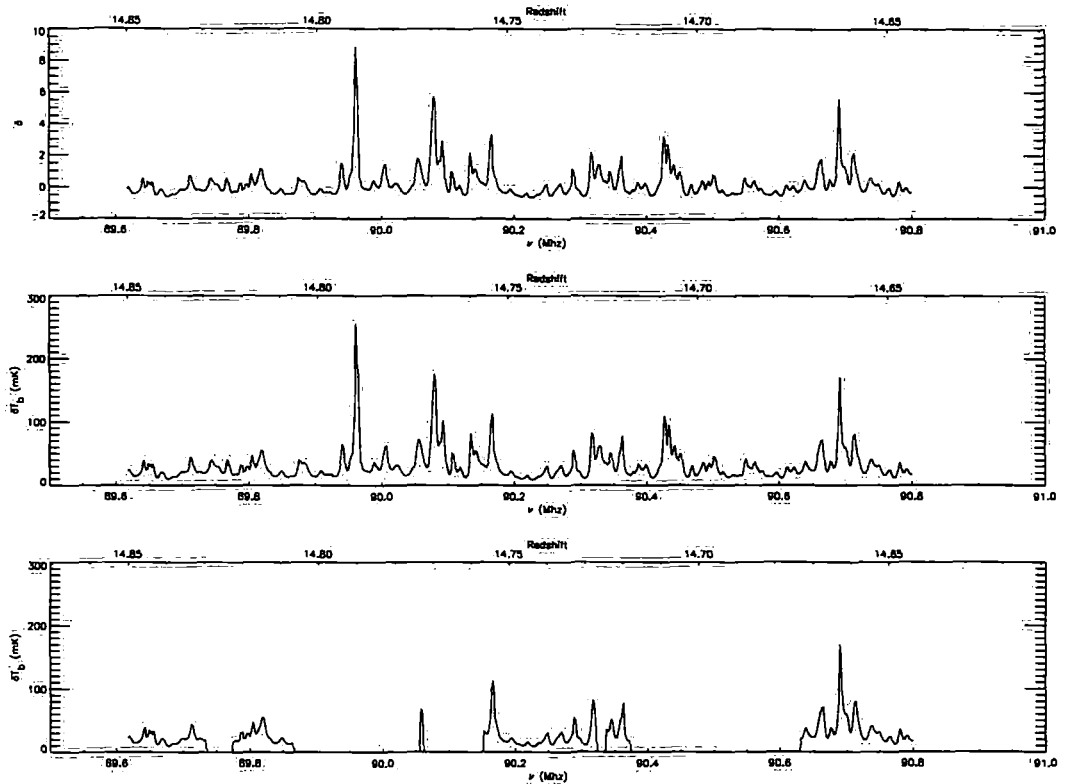


Figure 4.5: Example line-of-sight spectra from the L20\_N1024 simulation at  $z = 14.64$ , for the matter over-density (top), 21-cm differential brightness temperature (middle) and 21-cm differential brightness temperature with ionized regions in the simulation box (bottom). All three spectra are along same line-of-sight.

One thing to note in Fig. 4.5 is the frequency range. The L20\_N1024 simulation box covers approximately a range of 1.2MHz in frequency, and extends from  $z \approx 14.65$  to  $z \approx 14.85$ . Each individual cells covers a frequency range of  $\sim 2.34\text{kHz}$ . The frequency range covered by the box is small and does not reveal much about the evolution of neutral hydrogen. Although the following is not done in this thesis, a spectra with a larger frequency range could be created by using multiple snapshots to obtain a more complete picture of reionization. Gaps in the frequency between snapshots can be filled by tiling the periodic boxes, extending the frequency range of the LOS spectra obtained from a particular snapshot. It should also be noted that if reionization did occur at this redshift, LOFAR will not be able to detect it. The redshifted 21-cm signal would be at  $\sim 90\text{MHz}$  for a redshift of  $\sim 14$ , and this is below the frequency range of LOFAR.

## 4.5 21-cm Power Spectra

Upcoming experiments like LOFAR will have a low resolution that will not be able to resolve the smallest features in the 21-cm signal. They should however, be able to see larger structures in the structure such as ionized regions. One of the motivations for calculating the 21-cm power spectra is to determine what effect these ionized regions have on the 21-cm power at different scales. This would also be a quantity that can be measured from the observed, noisy low resolution data. Even though individual structures cannot be identified reliably due to noise, statistical quantities like power spectra can still be measured. The figures in this section aim to show how adding ionized regions alters the power spectra of the underlying  $\delta T_b$  field. The effects of smoothing are also investigated. As with the LOS spectra, these power spectra are generated from density and  $\delta T_b$  fields of the L20\_N1024 simulation box.

We define the dimensionless power spectrum,  $\Delta^2(k)$ , as the power per logarithmic interval in spatial frequency,  $k$ .

$$\Delta^2(k) = \frac{V}{(2\pi^2)} 4\pi k^3 \langle |\delta_k|^2 \rangle, \quad (4.26)$$

where  $V$  is the volume of the box and  $\langle |\delta_k|^2 \rangle$  is the mean power density for each  $k$ .  $\delta_k$  is obtained by performing a 3D Fourier transform on the  $\delta T_b$  field.

The power spectra of the hydrogen over-density field and  $\delta T_b$  field at  $z = 14.64$  are shown in Fig. 4.6. These are the power spectra of the simulation box if no reionization

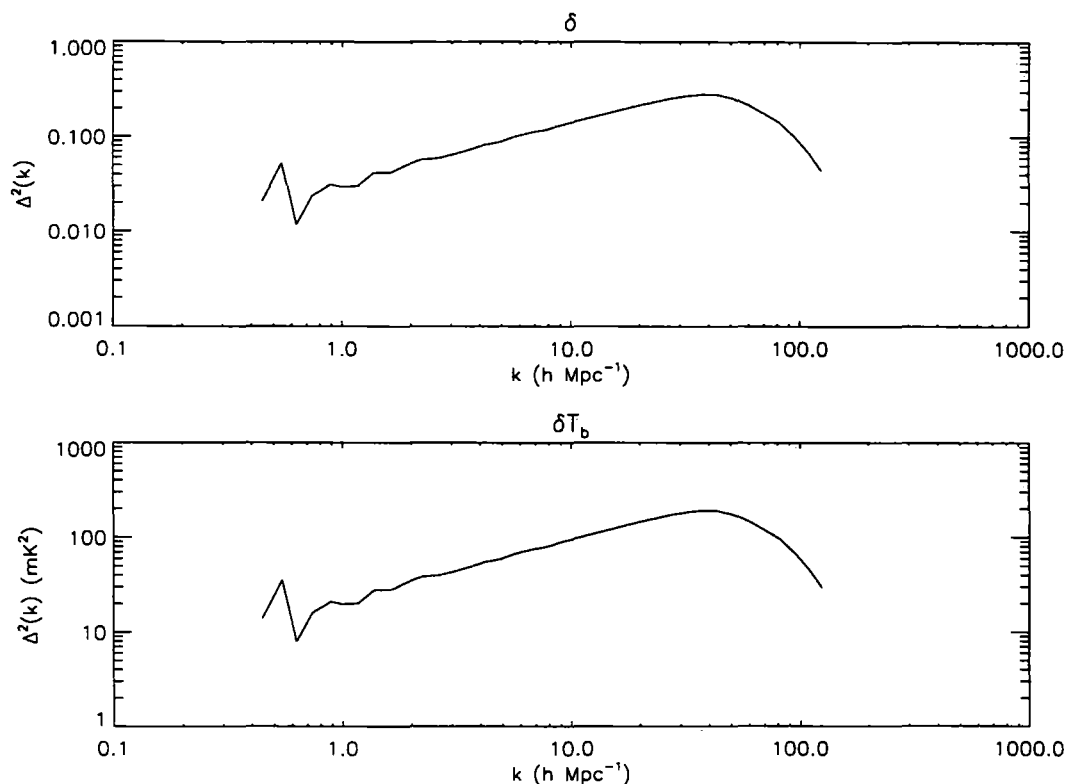
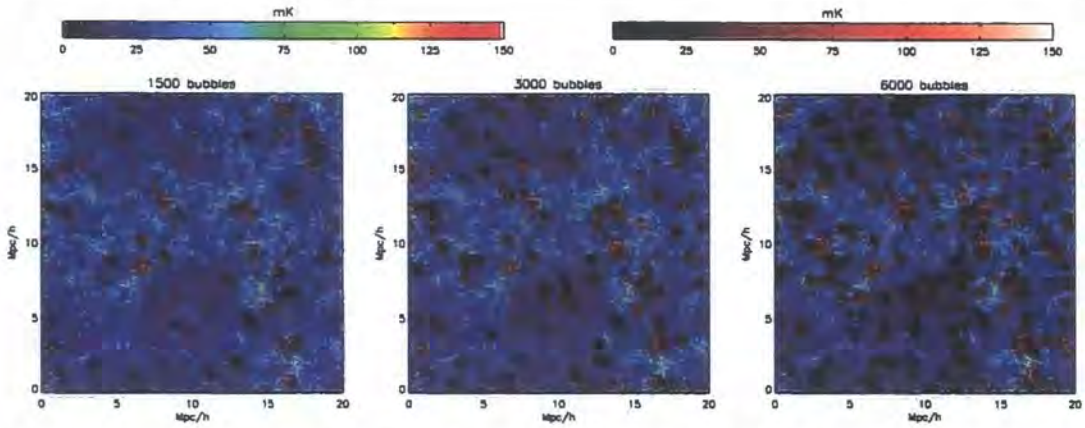


Figure 4.6: Power spectra of the hydrogen over-density field (top) and the differential brightness temperature field (bottom) of the L20\_N1024 simulation at  $z = 14.64$ . These are calculated on a  $512^3$  grid. Note the different scales used in the two figures.

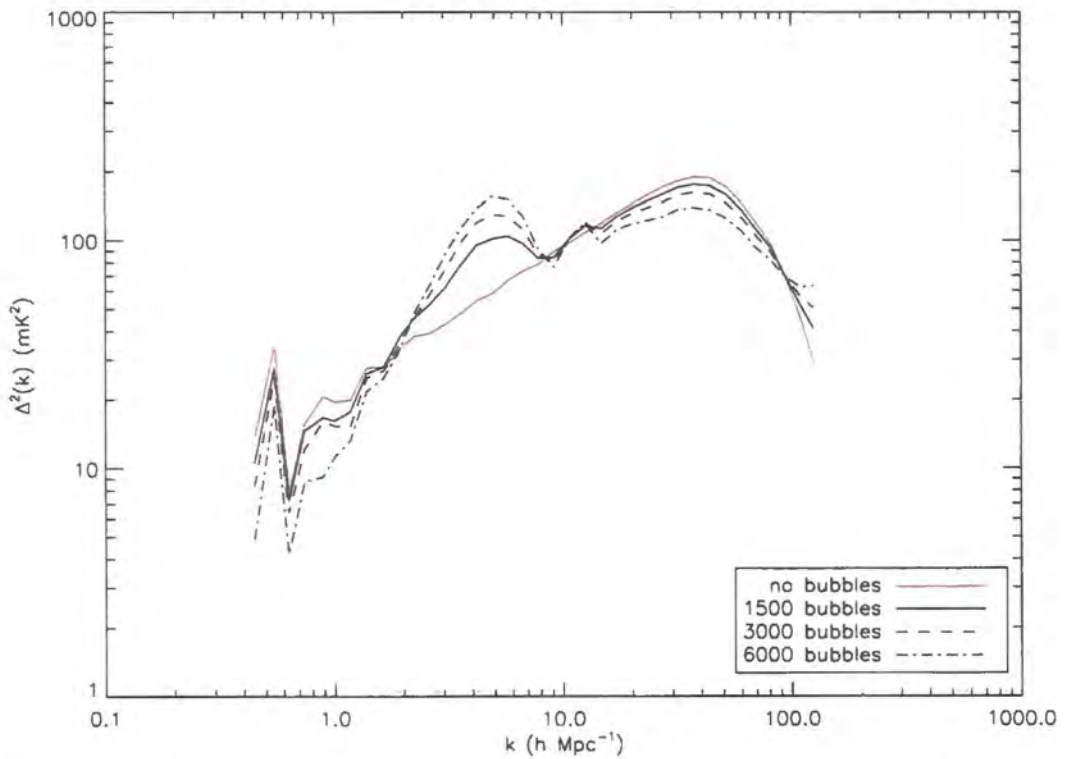
takes places and the whole box is completely neutral. Both spectra have the same shape since the brightness temperature calculated is the density multiplied by a constant factor (see eq. (4.20)). The turnover at  $k \sim 40 h \text{Mpc}^{-1}$  is due to the gridding of  $1024^3$  particles onto a  $512^3$  grid.

To help understand the effects of the ionized regions on the power spectra, we consider the following “toy model”. Some artificial ionized “bubbles” (spherical ionized regions) were first generated on top of the  $\delta T_b$  fields. The bubbles were distributed uniformly across the field, varying the number of bubbles and the size of bubbles.

In Fig. 4.7, spheres with a radius of  $0.5 h^{-1} \text{Mpc}$  were used. The black lines represent the different number of bubbles placed in the field. 1500, 3000 and 6000 bubbles correspond roughly to 10%, 20% and 40% of the total volume without taking into account any overlap. Fig. 4.7a shows example slices from the  $\delta T_b$  field to visualise the coverage of



(a) 2D slices illustrating the coverage of randomly distributed ionized regions in 4.7b (red scale), overlaid on top of the  $\delta T_b$  (rainbow scale) of the L20\_N1024 simulation at  $z = 14.64$ . The left, centre and right slices use 1500, 3000 and 6000 bubbles of radius  $0.5h^{-1}\text{Mpc}$  respectively. As before, the rainbow scale represents  $\delta T_b$  in neutral regions, while the red scale shows  $\delta T_b$  if the ionized regions were neutral.



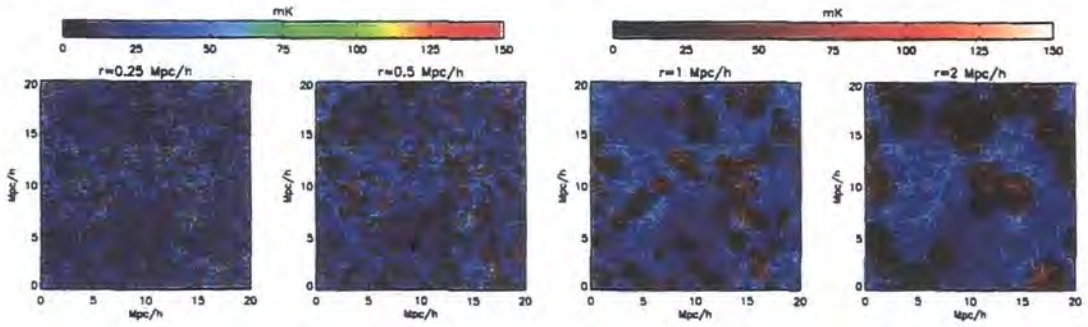
(b) 3D Power spectra of the  $\delta T_b$  field from the L20\_N1024 simulation at  $z = 14.64$ , with randomly distributed spherical ionized regions of radius  $0.5h^{-1}\text{Mpc}$ , varying the number of bubbles. The red line shows the power spectra of the  $\delta T_b$  field without any ionized regions while the black lines represent the different numbers of bubbles used. The position of the peaks corresponds to the size of the bubbles (see Fig. 4.8).

Figure 4.7: 2D slices and 3D Power spectra of the 21-cm brightness temperature field with randomly distributed ionized regions, varying the number of bubbles.

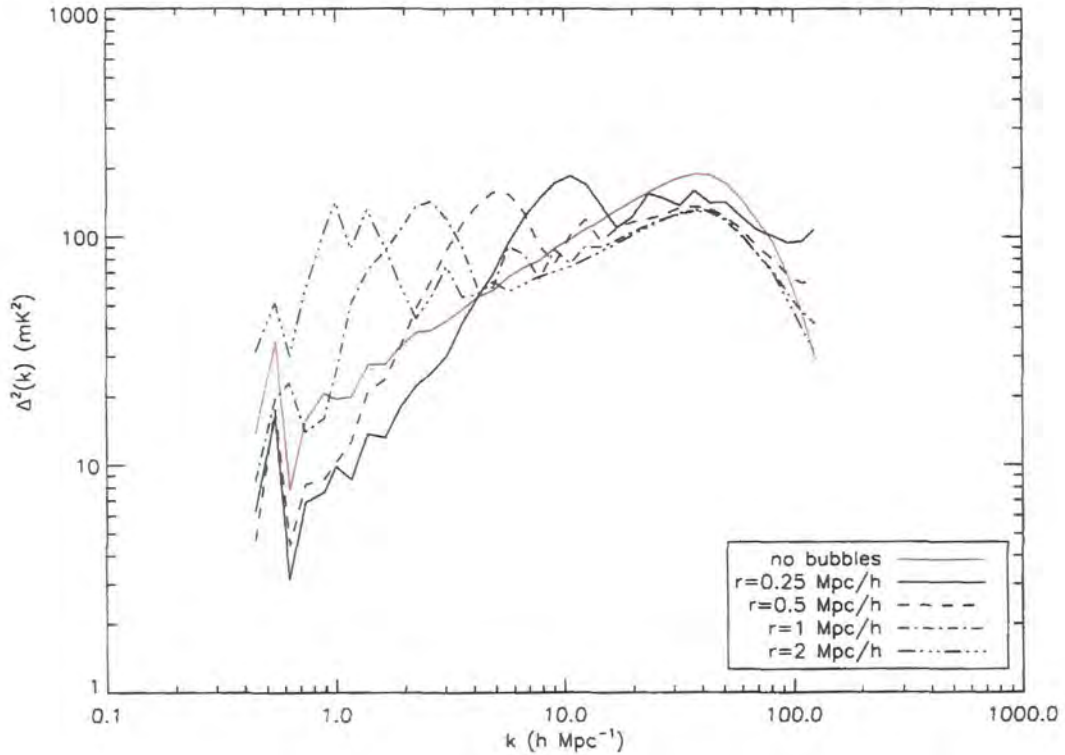
the ionized bubbles. There is a decrease in power at smaller scales when compared with the red line, the power spectra of the  $\delta T_b$  field without any ionized regions. The 21-cm signal is completely removed within the ionized bubbles, removing power from scales smaller than the bubble size. As more bubbles are added, the total volume covered by the bubbles and the ionized fraction of the box increases, removing an increasing amount of power. This is why for an increasing ionized fraction, there is decreasing power on small scales. There is also more power on  $k \sim 5h\text{Mpc}^{-1}$  scales, this corresponds to the physical size of the  $0.5h^{-1}\text{Mpc}$  spheres. The increase in number of bubbles, and hence the ionized fraction, results in more power on this scale. (see Fig. 4.8).

Fig. 4.8 again shows the power spectra of the  $\delta T_b$  field from the L20\_N1024 simulation at  $z = 14.64$  with artificial ionized bubbles, but with different sizes of bubbles. The ionized fraction of the box is kept approximately constant by choosing the number of spheres such that the total volume is the same with different sphere sizes. The exact ionized fraction will vary due to bubble overlap. For this figure, the ionized fraction of the box for all the bubble sizes is  $\sim 0.34$ . Fig. 4.8a shows example slices from the  $\delta T_b$  field to visualise the coverage of the ionized spheres of different sizes. The position of the different peaks correspond to the sizes of the bubbles. As previously discussed for Fig. 4.7, the power on small scales is likely affected by the ionized fraction of the box. In Fig. 4.8, the ionized fraction is kept approximately constant for all bubble sizes, the power on small scales is also approximately constant for the different bubble sizes. This suggests that the suppression on small scales is indeed due to an increasing ionized fraction. The amplitude of the peaks are also similar for the different sized bubbles because the ionized fraction is constant. The curve for the  $2h^{-1}\text{Mpc}$  bubble (dot dot dashed line) appears to have two peaks. However, there is considerable noise at large scales so it is likely this double peak is due to noise, rather than a real feature in the spectrum.

The evolution of the power spectra using ionized regions predicted by GALFORM from  $z = 15.64$  to  $z = 12.82$  is shown in Fig. 4.9. Comparing with the power spectra generated with the toy model, these spectra lack any obvious features. This is because the ionized regions predicted by GALFORM will have a range of different sizes. Despite the lack of features, it is clear that the slope of the power spectra decreases as redshift decreases.  $f_{\text{ion,cells}}$  at each redshift is indicated on the figures.  $f_{\text{ion,cells}}$  at  $z = 13.71$  and



(a) 2D slices illustrating the coverage of randomly distributed ionized regions in Fig. 4.8b (red scale), overlaid on top of  $\delta T_b$  (rainbow scale) of the L20\_N1024 simulation at  $z = 14.64$ . The slices from left to right use bubbles with radius of  $0.25h^{-1}\text{Mpc}$ ,  $0.5h^{-1}\text{Mpc}$ ,  $1h^{-1}\text{Mpc}$  and  $2h^{-1}\text{Mpc}$  in that order. The ionized fraction in each box is kept approximately constant at  $\sim 0.34$ . The color scales are the same as in Fig. 4.7a



(b) 3D Power spectra of the  $\delta T_b$  field from the L20\_N1024 simulation at  $z = 14.64$ , with randomly distributed ionized regions of various sizes. The ionized fraction is kept approximately constant at  $\sim 0.4$ . The red line shows the power spectra of the  $\delta T_b$  field without any ionized regions while the black lines represent different sizes of bubbles used.

Figure 4.8: 2D slices and 3D Power spectra of the 21-cm brightness temperature field with randomly distributed ionized regions, varying the size of the bubbles while keeping the ionized fraction approximately constant.

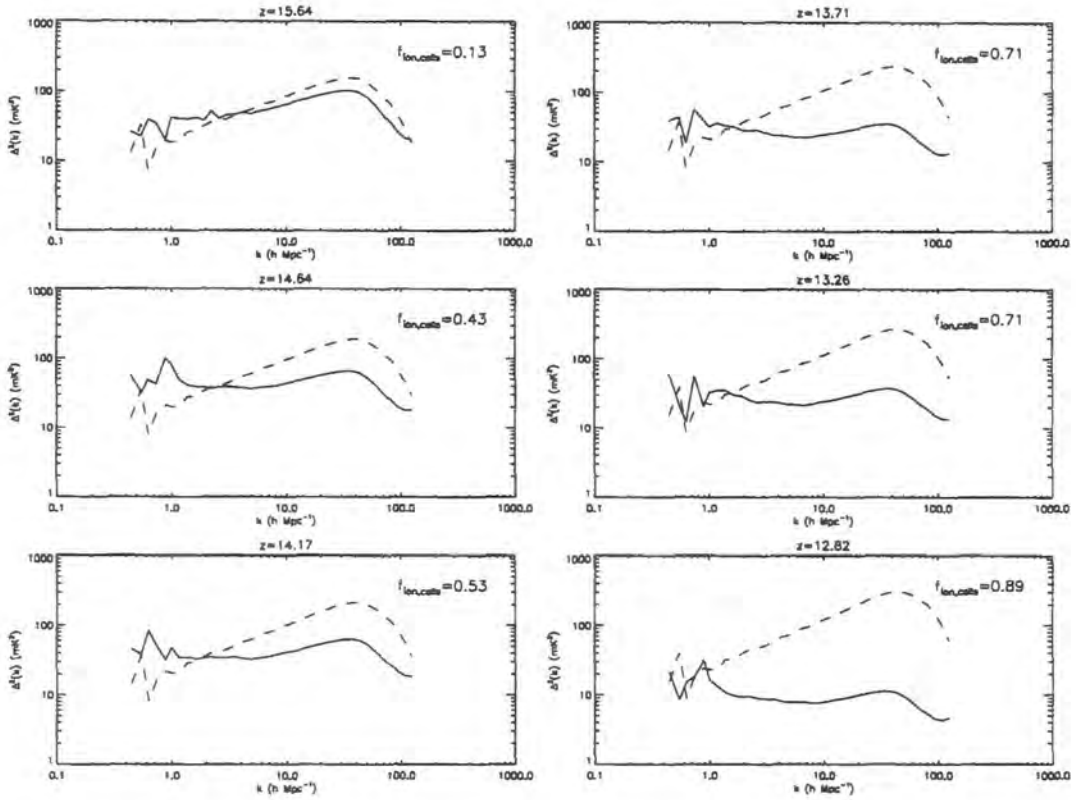


Figure 4.9: 3D power spectra of the  $\delta T_b$  field with ionized regions generated from GALFORM sources (solid lines), for the L20\_N1024 simulation at various redshifts. The power spectra for the field as if there was no reionization are also included for reference (dashed line). The slope of the spectra decreases as redshifts decreases.

$z = 13.26$  are nearly identical and it appears that the slope of these two power spectra are also very similar. The effect of ionized bubbles is that they remove the power on small scales, as the number and size of the bubbles increases, they wipe out power at increasingly larger scales. This has a big effect on small scales but only affects power on the large scales later in time. This suggests that the decrease in slope of the power spectra is likely to be due to the increasing ionized fraction. The power spectra presented here are similar to those in Santos et al. (2008). The power spectra in Santos et al. (2008) are at larger scales, ranging from  $k = 0.01h^{-1}\text{Mpc}$  to  $k = 10h^{-1}\text{Mpc}$ . There is considerable noise in our power spectra at these scales so it is difficult to compare in detail. However, at  $k = 10h^{-1}\text{Mpc}$ , the amplitude of the power spectra both presented here and in Santos et al. (2008) are similar.

## 4.6 Smoothing the Signal

The usefulness of theoretical predictions comes from comparison with observational data. This process allows astronomers to test our theoretical understanding of the problem. The 21-cm signal maps generated using the methods explained in this chapter are of considerably higher resolution than those one would expect from upcoming 21-cm observations using LOFAR. In this section, we will briefly look at the effects on the images, LOS spectra and power spectra generated in this chapter, of smoothing to the resolution of the observer.

To account for the lower resolution of the observations relative to the simulations, smoothing is carried out in two steps. Firstly, a tophat function with a width equivalent to 200kHz is convolved with the map in the frequency axis. This emulates the bandwidth of the LOFAR telescope. Next, each slice of the 21-cm grid is smoothed in the transverse direction using a 2-D Gaussian with a FWHM of 3 arcmin, again, emulating the LOFAR telescope beam response. After smoothing in bandwidth, the 2D slice of Fig. 4.3 is extracted from the data and shown in Fig. 4.10. Note the difference in the colour scale, this is because smoothing reduces rare, bright pixels from the grid. The smallest structures are smoothed over, but the ionized regions can still be seen clearly. The same slice is again shown in Fig. 4.11 after beam-smoothing. The range of temperatures observed has reduced further due to the smoothing. Now, only the largest structures are visible in this

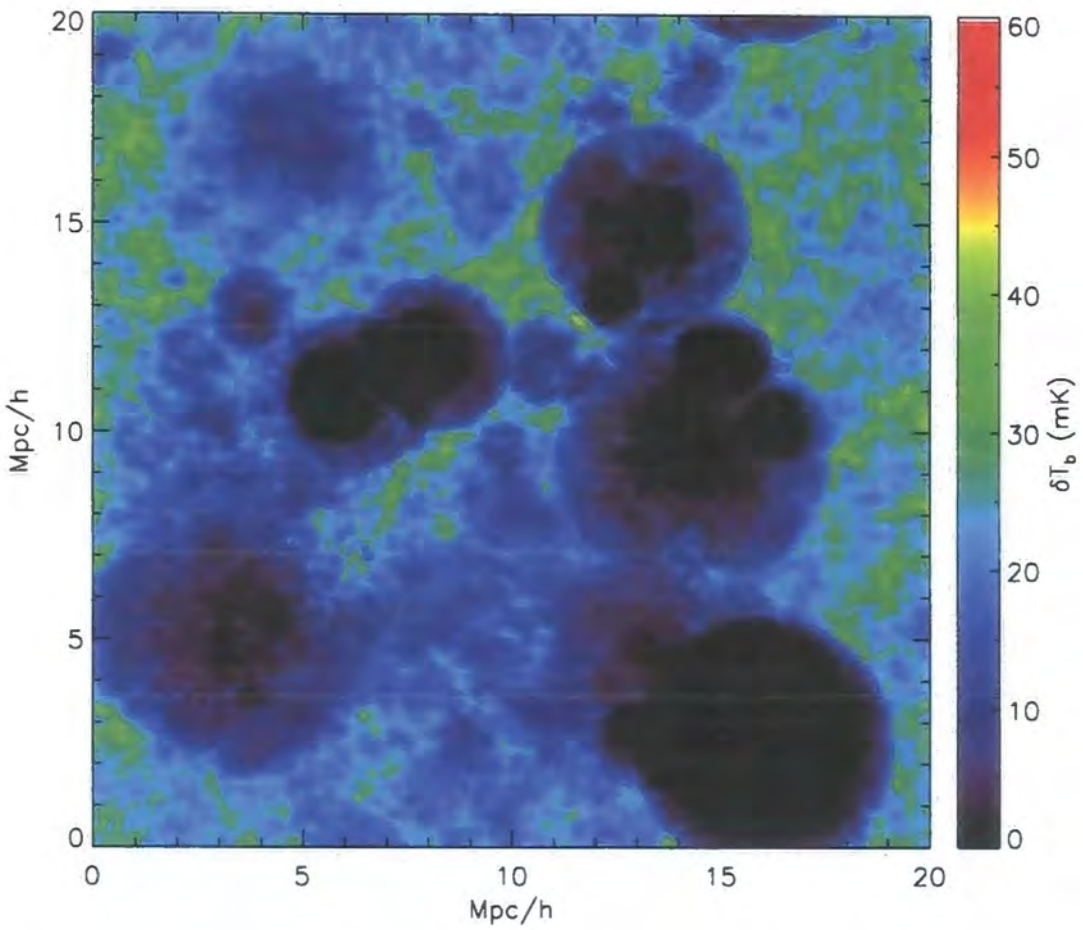


Figure 4.10: Bandwidth-smoothed  $\delta T_b$  of a 2D slice from the L20\_N1024 simulation at  $z = 14.64$ , smoothed over a bandwidth of 200kHz. This is the same slice as in Fig. 4.3. Comparing with Fig. 4.3, the rare bright peaks are no longer seen.

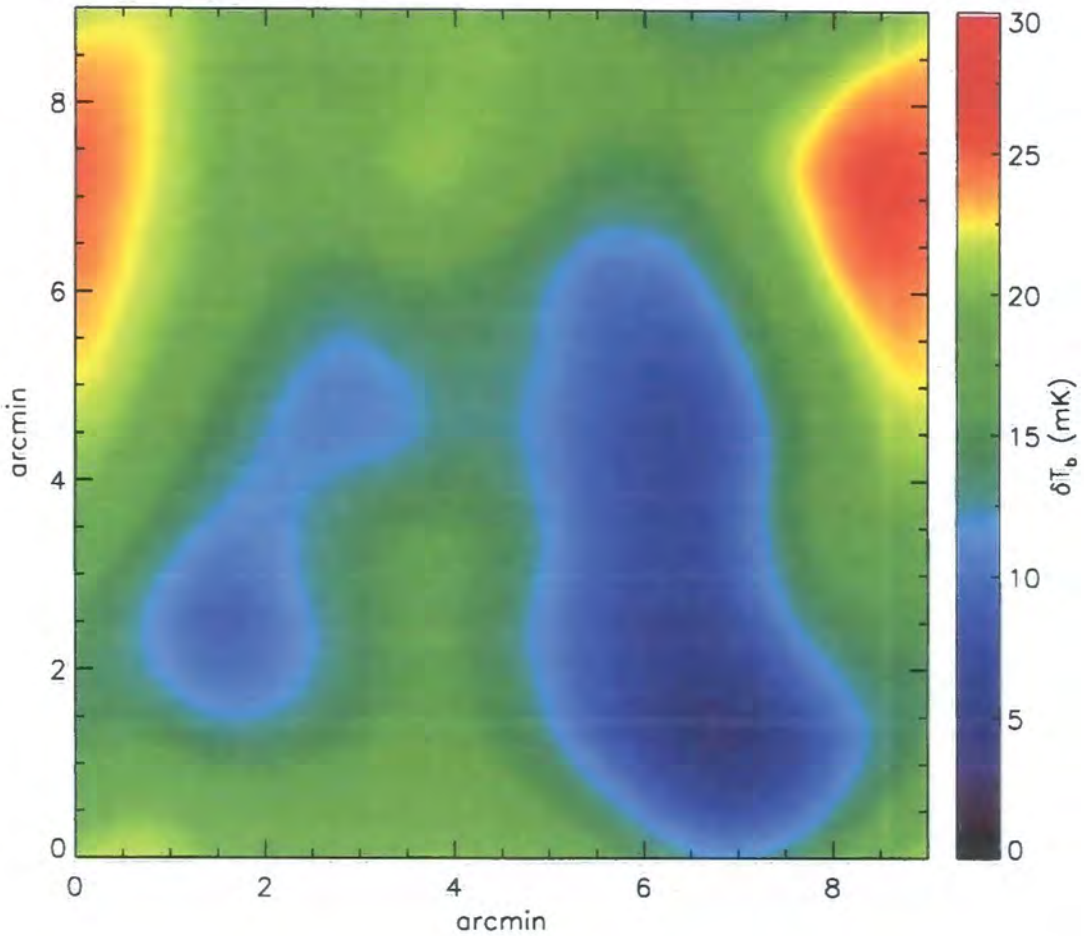


Figure 4.11: Bandwidth and beam-smoothed  $\delta T_b$  of a  $0.04h^{-1}\text{Mpc}$  thick slice from the L20\_N1024 simulation at  $z = 14.64$ , smoothed over a bandwidth of 200kHz and a Gaussian beam with FWHM of 3 arcmin. This is the same slice as in Fig. 4.3 and Fig. 4.10, only the largest structures are distinguishable.

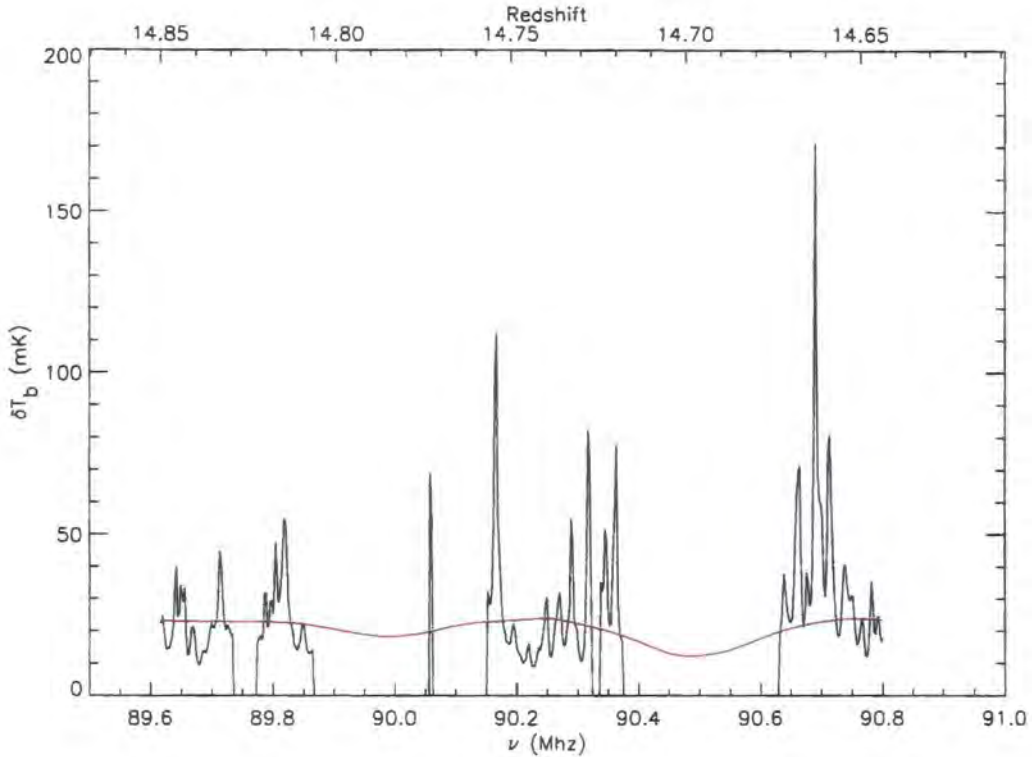


Figure 4.12: This figure shows the bottom LOS spectrum of Fig. 4.5 before (black) and after (red) smoothing the  $\delta T_b$  field with a Gaussian beam with FWHM of 3 arcmin and a bandwidth of 200kHz. The details have been wiped out, only the largest structures such as the trough at  $\sim 90.5$  can be distinguished.

image.

After smoothing the image over frequency and bandwidth, the spectrum from the same LOS of Fig. 4.5 is extracted again. This is shown in Fig. 4.12 and Fig. 4.13. In Fig. 4.12, the red, smoothed spectra looks almost completely flat compared to the original black spectrum. There is a small dip in the spectrum at  $\sim 90.5$  MHz due to a large ionized region. The remaining features of the spectrum can be seen more clearly in Fig. 4.13. The smoothing wipes out small features in the spectrum, but the main structures such as the troughs caused by large ionized regions at  $\sim 90$  MHz and  $\sim 90.5$  MHz can still be distinguished. The difference in the peak and trough of the signal is approximately 10 mK. As mentioned in section 4.4, LOFAR will have a sensitivity of approximately 35 MHz after 100 nights of observing. The smoothed LOS spectrum in Fig. 4.13 shows the signal to lie

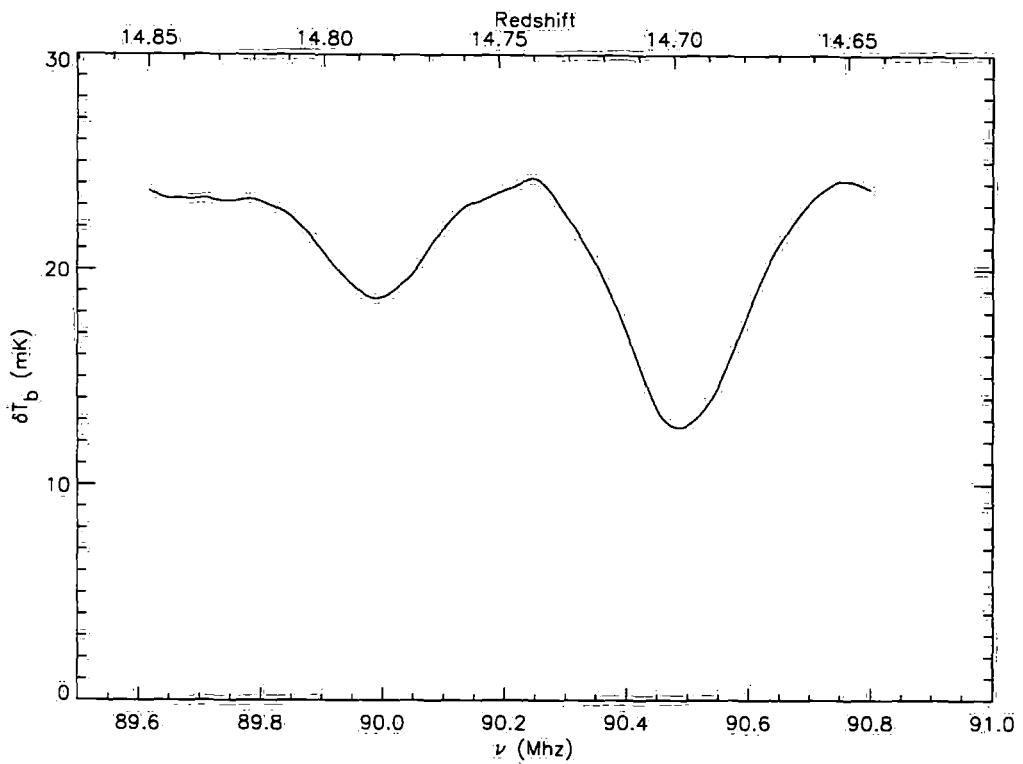


Figure 4.13: The smoothed spectrum of Fig. 4.12 shown on its own (the red line in Fig. 4.12). The troughs in the spectrum can be seen more clearly in this figure with a smaller range in the y-axis. There is a difference of approximately 10mK between the peak and trough of the spectrum.

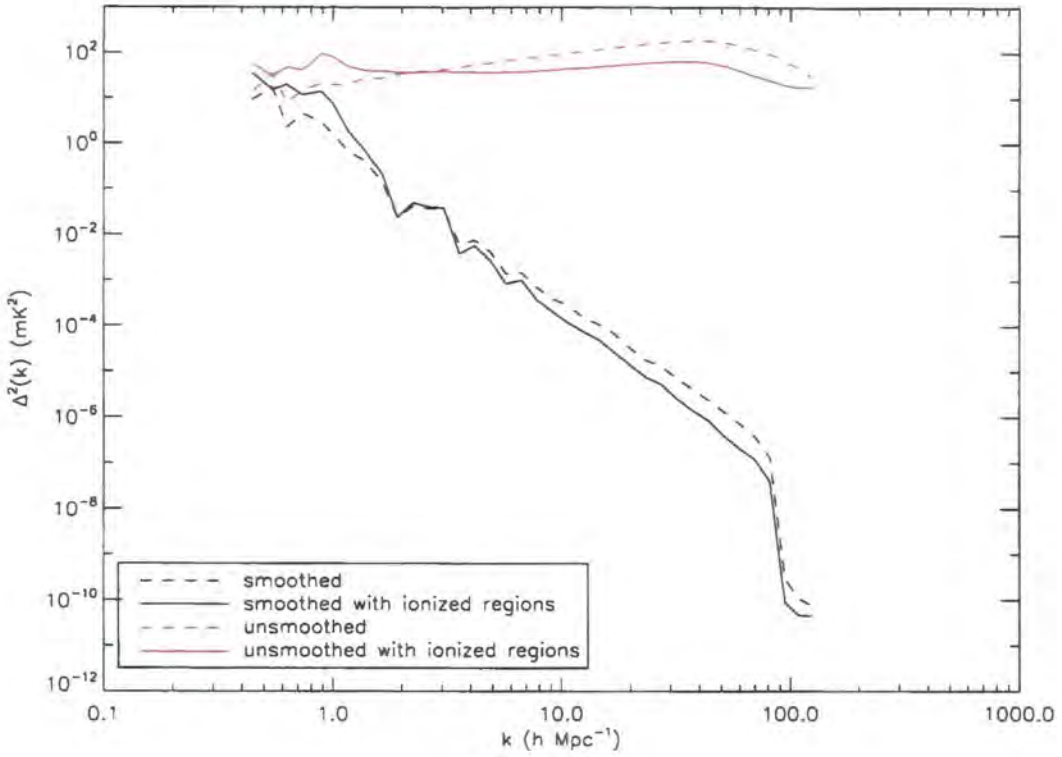


Figure 4.14: Power Spectra of the bandwidth and beam smoothed  $\delta T_b$  field at  $z = 14.64$ . The black lines are the smoothed power spectra while the red lines are the spectra before smoothing is applied, as shown in Fig. 4.9. As in Fig. 4.9, the dashed lines are the power spectra of the  $\delta T_b$  field without ionized regions, while the solid lines are the power spectra of the field with GALFORM ionized regions.

just below 35MHz. However, this is just one line of sight, there may be brighter regions where the signal may be detected. Nevertheless, this suggesting that LOFAR may have difficulties detecting the 21-cm signal with the planned observation time, and will not be able to detect the 10mK difference between the peak and trough of the signal. LOFAR will still be useful in observing the earlier stages of reionization, where the 21-cm signal should be brighter since the ionized fraction is lower in the Universe. Fig. 4.14 shows the power spectra of the smoothed  $\delta T_b$  field at  $z = 14.64$  in red, for both the  $\delta T_b$  field with and without GALFORM ionized regions. On the same plot in black are the power spectra of the field before smoothing is applied. The smoothed power spectra is nearly 10 orders of magnitude below the un-smoothed power spectra at the smallest

scales and the power is only comparable at the largest scales, where there is considerable noise. Note that our simulation is approximately 9 arcmin across while LOFAR will have a field of view of 5 degrees. Therefore we are missing much of the larger scale Fourier modes. LOFAR will not be able to detect the power on the smallest scales. A much larger simulation volume with a similar particle mass ( $\sim 5.17 \times 10^5 h^{-1} M_{\odot}$ ) is needed to determine the effect of smoothing has on the power spectra on larger scales.

# Chapter 5

## *Summary and Conclusions*

In this thesis, I simulated the 21-cm signal from the epoch of reionization. This was achieved using a combination of N-Body techniques and semi-analytical models. I ran seven N-Body simulations using L-GADGET2 for simulation volumes ranging from  $(10h^{-1}\text{Mpc})^3$  to  $(140h^{-1}\text{Mpc})^3$  and particle masses ranging from  $6.46 \times 10^4 h^{-1}M_{\odot}$  to  $1.42 \times 10^9 h^{-1}M_{\odot}$ . The GALFORM semi-analytical model was then used to predict properties of galaxies using the dark matter halo merger trees extracted from the N-Body simulations.

### 5.1 Ionizing luminosities from the GALFORM model

In chapter 3, I presented figures showing the distribution of ionizing luminosity as a function of halo mass for different simulation boxes. From these I have shown that:

- A large simulation volume with a low particle mass (high mass resolution) is required to cover the full dynamic range of halo masses that contribute significant ionizing photons. At  $z \sim 14.6$ , a particle mass of  $5 \times 10^5 h^{-1}M_{\odot}$  is needed to resolve the least massive halos contributing to the ionizing background. At the same redshift, a simulation volume of  $(140h^{-1}\text{Mpc})^3$  is large enough to see ionizing photons from halos with a mass of  $\sim 2 \times 10^{11} h^{-1}M_{\odot}$ . Using Monte-Carlo merger trees suggests that ionizing photons are produced from halos above this mass, but with emissivities more than two orders of magnitude less than the peak.
- A broad range of halo masses contribute significantly to the total ionizing luminosity, so it is important that simulations can cover the range of halo masses indicated in fig. 3.4.

Adjusting the  $z_{\text{cut}}$  parameter of the GALFORM model to model suppression of gas cooling in low mass halos showed that:

- changing the default value of  $z_{\text{cut}} = 6$  (this is effectively no suppression at the redshifts investigated) to  $z_{\text{cut}} = 15$  has significant effects on the ionizing luminosity generated by low mass halos at  $z < z_{\text{cut}}$ .
- The reduction in total ionizing photons generated after  $z_{\text{cut}}$  causes reionization to take place at a slower rate. This should result in a prolonged epoch of reionization.

## 5.2 The 21-cm Signal

In chapter 4, a simple method of calculating the spatial distribution of ionized regions was presented. This method uses the ionizing luminosity and positions of galaxies predicted by GALFORM to paint ionized regions around these galaxies. The size of the ionized region is calculated using cosmological Strömngren spheres. A method to compensate for lost photons in overlapping regions was also presented. For the L20\_N1024 simulation box, this was shown to be a good approximation at high redshifts ( $z > 14$ ) but became inaccurate at lower redshifts.

Next, images and spectra of the predicted 21-cm signal were presented. From the LOS spectra, it was shown that:

- The frequency range of one snapshot from a  $20h^{-1}\text{Mpc}$  simulation box is too small to extract much information about the evolution of neutral hydrogen during the epoch of reionization. It was suggested that this could be overcome by combining spectra from different redshifts of the same box and tiling the periodic simulation boxes to create a continuous spectrum between these snapshots of different redshifts.
- In the example LOS spectra presented, most of the signal lies below 50mK although there are occasional bright peaks, with some exceeding 250mK

Power spectra of the predicted differential brightness temperature ( $\delta T_b$ ) field, were also presented in this chapter. These were generated to investigate the effect ionized regions had on the power on different scales. As a simple test case, a toy model of

randomly distributed spheres of constant size representing the ionized regions were first painted onto the temperature field. For the toy model, it was shown that:

- A higher ionized fraction removes more power on small scales ( $k \sim 40h\text{Mpc}^{-1}$ ).
- Power is generated on the scales of the sphere sizes used, the amount of this power is affected by the ionized fraction. A higher ionized fraction caused by an increasing number of spheres of a constant size increases the power generated on the scales corresponding to the size of the spheres.

Following this, the power spectra of the  $\delta T_b$  field using GALFORM sources was presented after understanding of the basic effects ionized regions have on the power spectra. From these power spectra I concluded that:

- Compared with the randomly distributed bubbles of constant size, the power spectra using GALFORM sources lack any obvious features.
- An increased ionized fraction at lower redshifts reduces the slope of the power spectra. This presumably happens because as the ionized bubbles grow, the 21-cm signal is removed at increasingly larger scales.

Finally, images, LOS spectra and power spectra of the  $\delta T_b$  field smoothed using the LOFAR frequency and beam response were presented, from these it was shown that:

- Features on small scales are wiped out, the filamentary structures of the 21-cm signal inherited from the density field are no longer distinguishable.
- The occasional bright pixels previously seen in the un-smoothed LOS spectra are removed.
- Structures on large scales such as large ionized regions can still be seen in both the 2D slices and the LOS spectrum.
- Power on the smallest scales is not likely to be detected by LOFAR, while on large scales, a larger simulation is needed to see the largest scales in the power spectra that LOFAR will be able to detect.

Using GALFORM, the epoch of reionization was previously investigated in Benson et al. (2006). The Baugh et al. (2005) model used in this thesis was also one of the GALFORM models investigated in Benson et al. (2006). The difference in the work of this

thesis is the use of N-body simulations to generate dark matter halo merger trees. In the previous work, only Monte-Carlo merger trees were used. Although N-body merger trees have a lower mass resolution than Monte-Carlo merger trees, they provide valuable spatial information about the sources of reionization. This allows us to calculate ionization fronts, which was not possible in Benson et al. (2006).

The main motivation for simulating the 21-cm signal from the epoch of reionization is to help us understand the observations that will be made by 21-cm experiments such as LOFAR. The conclusion of this thesis suggest that although LOFAR is unlikely to observe the small scale features of the 21-cm signal, large scales structures such large ionized regions should be detected from the epoch of reionization. LOFAR should be able to detect the early stages of reionization, but may have difficulties during later stages when much of the brightest 21-cm signal is removed by reionization.

A large number of efforts on simulating the 21-cm signal are based on combining N-Body and radiative transfer techniques. To achieve the resolutions required, these are very computationally intensive. This thesis presented a method combining N-Body simulations, semi-analytical models and analytical calculations to simulate the 21-cm signal. Although likely to produce a less accurate picture of the epoch of reionization than using radiative transfer, this method can be implemented much more quickly. The success of semi-analytical models in galaxy formation in recent years also makes this method interesting. The effect of different parameters in the models on reionization can be experimented with very quickly without the need to do a radiative transfer run every time a parameter is changed. This means the parameter space of the model can first be explored cheaply before doing radiative transfer on the models that we find most interesting. The 21-cm signal will tell us a lot about the epoch of reionization, a period that we do not know much about. It will be interesting and exciting to see what these observations will tell us about the evolution of the Universe.

### 5.3 Directions for Future Work

There have been various simplifications made in this thesis to allow for ease of implementation. Here, I list some of the improvements that could be made by using more complex methods:

- Instead of assuming all the hydrogen is neutral, assign a neutral fraction to each cell in the density grid. The same can be done for within ionized regions.
- The Strömgren sphere calculation uses the average hydrogen number density of the simulation box. This does not take into account of local variations in the density, the local density around the sources should be used instead.
- A better implementation is required to allow for overlapping ionized regions at low redshifts.

The following improvements would increase computing time significantly, but should provide more accurate results:

- A larger simulation volume with similar mass resolution as the L20\_N1024 can be run to cover the full dynamic range in halo masses required. A larger simulation will also be able to see the largest scales in the power spectra that LOFAR will be able to detect.
- Instead of assuming that the hydrogen gas follows the dark matter, a SPH simulation can be carried out to determine the distribution of hydrogen.
- Radiative transfer techniques can be used to calculate the ionized regions instead of using Strömgren spheres.

Finally, the semi-analytical models of galaxy formation are constantly being improved, the same procedure carried out in this thesis can be repeated for different models.



# Bibliography

Barkana, R. and Loeb, A.: 2001, *Phys. Rep.* **349**, 125

Barnes, J. and Hut, P.: 1986, *Nature* **324**, 446

Baugh, C. M.: 2006, *Reports on Progress in Physics* **69**, 3101

Baugh, C. M., Lacey, C. G., Frenk, C. S., Granato, G. L., Silva, L., Bressan, A., Benson, A. J., and Cole, S.: 2005, *MNRAS* **356**, 1191

Becker, R. H., Fan, X., White, R. L., Strauss, M. A., Narayanan, V. K., Lupton, R. H., Gunn, J. E., Annis, J., Bahcall, N. A., Brinkmann, J., Connolly, A. J., Csabai, I., Czarapata, P. C., Doi, M., Heckman, T. M., Hennessy, G. S., Ivezić, Ž., Knapp, G. R., Lamb, D. Q., McKay, T. A., Munn, J. A., Nash, T., Nichol, R., Pier, J. R., Richards, G. T., Schneider, D. P., Stoughton, C., Szalay, A. S., Thakar, A. R., and York, D. G.: 2001, *AJ* **122**, 2850

Benson, A. J., Bower, R. G., Frenk, C. S., Lacey, C. G., Baugh, C. M., and Cole, S.: 2003, *ApJ* **599**, 38

Benson, A. J., Sugiyama, N., Nusser, A., and Lacey, C. G.: 2006, *MNRAS* **369**, 1055

Bond, J. R., Cole, S., Efstathiou, G., and Kaiser, N.: 1991, *ApJ* **379**, 440

Bower, R. G., Benson, A. J., Malbon, R., Helly, J. C., Frenk, C. S., Baugh, C. M., Cole, S., and Lacey, C. G.: 2006, *MNRAS* **370**, 645

Bruzual A., G. and Charlot, S.: 1993, *ApJ* **405**, 538

Ciardi, B., Ferrara, A., Marri, S., and Raimondo, G.: 2001, *MNRAS* **324**, 381

Ciardi, B. and Madau, P.: 2003, *ApJ* **596**, 1

Cole, S., Lacey, C. G., Baugh, C. M., and Frenk, C. S.: 2000, *MNRAS* **319**, 168

- Croton, D. J., Springel, V., White, S. D. M., De Lucia, G., Frenk, C. S., Gao, L., Jenkins, A., Kauffmann, G., Navarro, J. F., and Yoshida, N.: 2006, *MNRAS* **365**, 11
- Fan, X., White, R. L., Davis, M., Becker, R. H., Strauss, M. A., Haiman, Z., Schneider, D. P., Gregg, M. D., Gunn, J. E., Knapp, G. R., Lupton, R. H., Anderson, Jr., J. E., Anderson, S. F., Annis, J., Bahcall, N. A., Boroski, W. N., Brunner, R. J., Chen, B., Connolly, A. J., Csabai, I., Doi, M., Fukugita, M., Hennessy, G. S., Hindsley, R. B., Ichikawa, T., Ivezić, Ž., Loveday, J., Meiksin, A., McKay, T. A., Munn, J. A., Newberg, H. J., Nichol, R., Okamura, S., Pier, J. R., Sekiguchi, M., Shimasaku, K., Stoughton, C., Szalay, A. S., Szokoly, G. P., Thakar, A. R., Vogeley, M. S., and York, D. G.: 2000, *AJ* **120**, 1167
- Field, G. B.: 1959, *ApJ* **129**, 536
- Freedman, W. L., Madore, B. F., Gibson, B. K., Ferrarese, L., Kelson, D. D., Sakai, S., Mould, J. R., Kennicutt, Jr., R. C., Ford, H. C., Graham, J. A., Huchra, J. P., Hughes, S. M. G., Illingworth, G. D., Macri, L. M., and Stetson, P. B.: 2001, *ApJ* **553**, 47
- Furlanetto, S. R. and Furlanetto, M. R.: 2007, *MNRAS* **374**, 547
- Furlanetto, S. R., Oh, S. P., and Briggs, F. H.: 2006, *Phys. Rep.* **433**, 181
- Haiman, Z. and Loeb, A.: 1999, *ApJ* **519**, 479
- Hubble, E.: 1929, *Proceedings of the National Academy of Science* **15**, 168
- Iliev, I. T., Mellema, G., Pen, U.-L., Merz, H., Shapiro, P. R., and Alvarez, M. A.: 2006, *MNRAS* **369**, 1625
- Iliev, I. T., Mellema, G., Shapiro, P. R., and Pen, U.-L.: 2007, *MNRAS* **376**, 534
- Jenkins, A., Frenk, C. S., White, S. D. M., Colberg, J. M., Cole, S., Evrard, A. E., Couchman, H. M. P., and Yoshida, N.: 2001, *MNRAS* **321**, 372
- Lacey, C. and Cole, S.: 1993, *MNRAS* **262**, 627
- Mather, J. C., Cheng, E. S., Cottingham, D. A., Eplee, Jr., R. E., Fixsen, D. J., Hewagama, T., Isaacman, R. B., Jensen, K. A., Meyer, S. S., Noerdlinger, P. D., Read, S. M., Rosen, L. P., Shafer, R. A., Wright, E. L., Bennett, C. L., Boggess, N. W., Hauser, M. G., Kelsall, T., Moseley, Jr., S. H., Silverberg, R. F., Smoot, G. F., Weiss, R., and Wilkinson, D. T.: 1994, *ApJ* **420**, 439

- Mellema, G., Iliev, I. T., Pen, U.-L., and Shapiro, P. R.: 2006, *MNRAS* **372**, 679
- Nolta, M. R., Dunkley, J., Hill, R. S., Hinshaw, G., Komatsu, E., Larson, D., Page, L., Spergel, D. N., Bennett, C. L., Gold, B., Jarosik, N., Odegard, N., Weiland, J. L., Wollack, E., Halpern, M., Kogut, A., Limon, M., Meyer, S. S., Tucker, G. S., and Wright, E. L.: 2008, *ArXiv e-prints*
- Nusser, A.: 2005, *MNRAS* **359**, 183
- Ott, J., Walter, F., and Brinks, E.: 2005, *MNRAS* **358**, 1453
- Peacock, J. A.: 1999, *Cosmological Physics*, Cambridge University Press
- Peebles, P. J. E.: 1993, *Principles of Physical Cosmology*, Princeton University Press
- Press, W. H. and Schechter, P.: 1974, *ApJ* **187**, 425
- Pritchard, J. R. and Furlanetto, S. R.: 2006, *MNRAS* **367**, 1057
- Rybicki, G. B. and Lightman, A. P.: 1979, *Radiative Processes in Astrophysics*, Wiley
- Salmon, J. K. and Warren, M. S.: 1994, *Journal of Computational Physics* **111**, 136
- Santos, M. G., Amblard, A., Pritchard, J., Trac, H., Cen, R., and Cooray, A.: 2008, *ApJ* **689**, 1
- Schechter, P.: 1976, *ApJ* **203**, 297
- Seljak, U. and Zaldarriaga, M.: 1996, *ApJ* **469**, 437
- Shapiro, P. R. and Giroux, M. L.: 1987, *ApJ* **321**, L107
- Sheth, R. K., Mo, H. J., and Tormen, G.: 2001, *MNRAS* **323**, 1
- Springel, V.: 2005, *MNRAS* **364**, 1105
- Springel, V., White, S. D. M., Jenkins, A., Frenk, C. S., Yoshida, N., Gao, L., Navarro, J., Thacker, R., Croton, D., Helly, J., Peacock, J. A., Cole, S., Thomas, P., Couchman, H., Evrard, A., Colberg, J., and Pearce, F.: 2005, *Nature* **435**, 629
- Springel, V., Yoshida, N., and White, S. D. M.: 2001, *New Astronomy* **6**, 79
- Strömberg, B.: 1939, *ApJ* **89**, 526

- Sutherland, R. S. and Dopita, M. A.: 1993, *ApJS* **88**, 253
- Thomas, R. M., Zaroubi, S., Ciardi, B., Pawlik, A. H., Labropoulos, P., Jelic, V., Bernardi, G., Brentjens, M. A., de Bruyn, A. G., Harker, G. J. A., Koopmans, L. V. E., Mellema, G., Pandey, V. N., Schaye, J., and Yatawatta, S.: 2008, *ArXiv e-prints*
- Thoul, A. A. and Weinberg, D. H.: 1996, *ApJ* **465**, 608
- Tumlinson, J. and Shull, J. M.: 2000, *ApJ* **528**, L65
- van Albada, T. S., Bahcall, J. N., Begeman, K., and Sancisi, R.: 1985, *ApJ* **295**, 305
- White, S. D. M. and Rees, M. J.: 1978, *MNRAS* **183**, 341
- Wouthuysen, S. A.: 1952, *AJ* **57**, 31
- Zahn, O., Lidz, A., McQuinn, M., Dutta, S., Hernquist, L., Zaldarriaga, M., and Furlanetto, S. R.: 2007, *ApJ* **654**, 12
- Zel'Dovich, Y. B.: 1970, *A&A* **5**, 84
- Zygelman, B.: 2005, *ApJ* **622**, 1356

